STUDY ON EFFECT OF WATER CONTENTS ON MUDFLOW ZONE OF SIDEWALL AT PHU KHAM MINING

SURIYA WONGKAEW

มหาวิทยาลัยเทคโนโลยีสุรนารี

A Thesis Submitted in Partial Fulfillment of the Requirements for the
Degree of Master of Engineering in Civil, Transportation
and Geo-resources Engineering
Suranaree University of Technology
Academic Year 2023

การศึกษาผลกระทบของปริมาณน้ำต่อพื้นที่โคลนไหล ของผนังบ่อเหมืองภูคำ

นายสุริยา วงค์แก้ว

มหาวิทยาลัยเทคโนโลยีสุรนารี

วิทยานิพนธ์นี้เป็นส่วนหนึ่งของการศึกษาตามหลักสูตรปริญญาวิศวกรรมศาสตรมหาบัณฑิต
สาขาวิชาวิศวกรรมโยธา ขนส่ง และทรัพยากรธรณี
มหาวิทยาลัยเทคโนโลยีสุรนารี
ปีการศึกษา 2566

STUDY ON EFFECT OF WATER CONTENTS ON
MUDFLOW ZONE OF SIDEWALL AT PHU KHAM MINING

Suranaree University of Technology has approved this thesis submitted in partial fulfillment of the requirements for a Master's Degree.

Thesis Examining Committee

.....

(Assoc. Prof. Dr. Pornkasem Jongpradist)
Chairperson

.....

(Dr. Thanittha Thongprapha)
Member (Thesis Advisor)

.....

(Asst. Prof. Dr. Prachya Tepnarong)
Member

.....

(Assoc. Prof. Dr. Yupaporn Ruksakulpiwat)
Vice Rector for Academic Affairs and
Quality Assurance

.....

(Assoc. Prof. Dr. Pornsiri Jongkol)
Dean of Institute of Engineering

มหาวิทยาลัยเทคโนโลยีสุรนารี

สุริยา วงค์แก้ว: การศึกษาผลกระทบของปริมาณน้ำต่อพื้นที่โคลนไหลของผนังบ่อเหมืองภูคำ (STUDY ON EFFECT OF WATER CONTENTS ON MUDFLOW ZONE OF SIDEWALL AT PHU KHAM MINING) อาจารย์ที่ปรึกษา : ดร.ธนิษฐา ทองประภา, 108 หน้า

คำสำคัญ: ความมั่นคงของความลาดเอียง/กำลังรับแรงเฉือน /รอยเลื่อน /ปริมาณความชื้น

โคลนไหลได้รับการศึกษาโดยการทดสอบแรงเฉือนโดยตรงและการจำลองเชิงตัวเลข เพื่อหาผลกระทบของปริมาณน้ำต่อความมั่นคงของความลาดเอียงบริเวณผนังด้านทิศใต้ของบ่อเหมืองภูคำ ประเทศลาว วัสดุโคลนไหลบนผนังเพดานประกอบด้วยรอยเลื่อนสีดำ (BSH) และหินเถ้าภูเขาไฟ (VTF) ถูกเตรียมไว้สำหรับการทดสอบแรงเฉือนโดยตรงภายใต้การผันแปรปริมาณน้ำตั้งแต่ร้อยละ 0 5 10 15 20 25 30 และ 35 โดยน้ำหนัก ผลการทดสอบแสดงให้เห็นว่ากำลังรับแรงเฉือนมีค่าลดลงเมื่อมีปริมาณน้ำเพิ่มขึ้น โดยเฉพาะตัวอย่างรอยเลื่อนสีดำภายใต้แรงดันตั้งฉากต่ำ สมบัติทางกลและทางเคมีบ่งชี้ว่าปริมาณแร่ดินเหนียวของรอยเลื่อนสีดำมีสัดส่วนมากกว่าหินเถ้าภูเขาไฟ แบบจำลองความลาดชันได้บรรจุชั้นดินอ่อนที่มีความลาดเอียงเป็นมุม 63 องศา ผลการจำลองเชิงตัวเลขระบุว่าค่าปัจจัยความปลอดภัยมีค่าลดลงด้วยการเพิ่มขึ้นของมุมความลาดเอียง ความสูงของความลาดเอียงและปริมาณน้ำ ตำแหน่งของระนาบรอยเลื่อนสีดำที่ไม่แข็งแรงบนหน้าลาดเอียงมีผลกระทบอย่างมีนัยสำคัญต่อความมั่นคงของความลาดเอียง ปริมาณน้ำส่งผลต่อปัจจัยความปลอดภัยเล็กน้อยหากระนาบดินอ่อนไม่ได้พาดตัดหน้าลาดเอียง ปริมาณน้ำของรอยเลื่อนสีดำมีผลกระทบน้อยต่อความลาดเอียงโดยรวม แม้ว่าวัสดุนั้นจะเป็นดินเหนียวก็ตาม ผลการจำลองเชิงตัวเลขถูกนำมาใช้เพื่อพัฒนาสมการเชิงประจักษ์ สมการนี้สามารถคาดคะเนปัจจัยความปลอดภัยภายใต้มุมของความลาดชัน ความสูงของความลาดชัน และปริมาณน้ำที่แตกต่างกัน โดยสภาวะของน้ำบาดาลไม่ได้ถูกศึกษาในกรณีนี้

สาขาวิชา เทคโนโลยีธรณี ลายมือชื่อนักศึกษา .....

ปีการศึกษา 2566 ลายมือชื่ออาจารย์ที่ปรึกษา .....

SURIYA WONGKAEW: STUDY ON EFFECT OF WATER CONTENTS ON MUDFLOW ZONE OF SIDEWALL AT PHU KHAM MINING. THESIS ADVISOR: THANITTHA THONGPRAPHA, PH.D., 108 PP.

Keyword: Slope stability/Shear strength/Fault /Moisture content

Mudflow has been investigated by direct shear testing and numerical simulation to determine the effect of water contents on slope stability at the south wall of Phu Kham open pit mine, Laos. The mudflow materials on the hanging wall including black fault (BSH) and volcanic tuff (VTF) are prepared for direct shear tests with different water contents varying from 0%, 5%, 10%, 15%, 20%, 25%, 30% to 35% by weights. Test results show that shear strengths reduce with increasing water content, specifically BSH under low normal load pressure. The mechanical and chemical properties of BSH indicate more clay mineral proportion than VTF material. The modelled slopes contain an inclined weak layer with 63° slope face. Numerical results indicate that the factors of safety decrease with increasing slope face angles, slope heights, and water contents. The position of the weak BSH plane on the slope face has a significant impact on the stability slope. The water content slightly affects the factor of safety if the plane of weakness is not across the slope face. The water content of BSH slightly influences the overall slope even though the material has clay material. Numerical simulation results are used to develop empirical equations. The equations can predict the safety factor under different slopes face angles, slope height, and water contents. Ground water condition is not studied in this case.

School of Geotechnology

Academic Year 2023

Student's Signature .....

Advisor's Signature .....

ACKNOWLEDGEMENTS

I would like to express the Institute of Research and Development, Suranaree University of Technology funding for this research. I would like to express my honest appreciation to Dr. Thanittha Thongprapha for her valuable guidance. I appreciate her powerful support, suggestions, and encouragement during the research period. I also would like to thank Professor Dr. Kittitep Fuenkajorn for valuable suggestions, support and comments on my research works. Grateful thanks to all the staff of the Geomechanics Research Unit who helped and supported my work.

Suriya Wongkaew

มหาวิทยาลัยเทคโนโลยีสุรนารี

TABLE OF CONTENTS

Page

ABSTRACT (THAI) ..... **I**

ABSTRACT (ENGLIST) ..... **II**

ACKNOWLEDGEMENT ..... **III**

TABLE OF CONTENTS ..... **IV**

LIST OF TABLES ..... **VIII**

LIST OF FIGURES ..... **IX**

LIST OF ABBREVIATIONS ..... **XVI**

CHAPTER

I INTRODUCTION **1**

1.1 Background and Rationale 1

1.2 Research Objective 1

1.3 Scope and Limitations 2

1.4 Research Methodology 3

1.4.1 Literature Review 4

1.4.2 Study area 4

1.4.3 Samples collection and preparation 4

1.4.4 Chemical properties 4

1.4.5 Physical properties test 4

1.4.6 Direct shear test 5

1.4.7 Numerical model simulation 5

1.4.8 Analysis of test result 5

TABLE OF CONTENTS (Continued)

Page

1.4.9 Discussions, and conclusions 5
1.5 Thesis Contents 6
II LITERATURE REVIEW 7
2.1 Introduction 7
2.2 Effect of mudflow material at Phu Kham mine 7
2.3 Effect of water content on weak material 9
2.4 Effect of slope characters on stability of slope 14
2.5 Effect of mineral compositions on slope stability 21
2.6 Computer simulations of slope stability 22
III STUDY AREA 36
3.1 Introduction 36
3.2 Location of Phu Kham mine 36
3.3 Failure of south wall 37
3.4 Lithology and structure control at south wall 36
3.4.1 Lithologies and weathering boundaries at south wall 38
3.4.2 Structure control at south wall 40
3.5 Stability analysis at south wall 44
IV SAMPLE COLLECTION AND PREPARATION 50
4.1 Introduction 50
4.2 Sample collection 50
4.3 Physical property test 51
4.3.1 Natural water content 51
4.3.2 Specific gravity 52

TABLE OF CONTENTS (Continued)

Page

4.3.3 Sand cone test 52
4.3.4 Grain size analysis 53
4.3.5 Atterberge's limit test 54
4.4 Chemical Property Test 55

V DIRECT SHEAR TESTING 61

5.1 Introduction 61
5.2 Sample preparation 61
5.3 Test method 62
5.4 Test results 64

VI NUMERICAL SIMULATIONS 84

6.1 Introduction 84
6.2 Slope geometry 84
6.3 Simulation model 86
6.4 Simulation results 86
6.4.1 Effect of slope face angle 86
6.4.2 Effect of position of exposed BSH plane on slope face 86
6.4.3 Effect of water content of VTF and slope height 87
6.5 Empirical equation 96

VII DISCUSSIONS, CONCLUSIONS AND RECOMMENDATIONS FOR FUTURE STUDIES 98

7.1 Discussions 98
7.2 Conclusions 99

TABLE OF CONTENTS (Continued)

Page

7.3 Recommendations for future studies..... 101

REFERENCES.....102

BIOGRAPHY 108

มหาวิทยาลัยเทคโนโลยีสุรนารี

LIST OF TABLES

Table **Page**

2.1 Slope angle and factor of safety (Shiferaw, 2021)..... 16
2.2 The mechanical and physical properties of rockmass (Zhao et al., 2023). 18
2.3 Mass mechnical parametoers (Su et al., 2022) 25
2.4 Designed safety of factor results (Su et al., 2022)..... 27
2.5 Properties of rock and weak layer (Beyabanaki, 2020)..... 29
2.6 Summary of minimum of safety factor results by FDM and LEM analysis (Beyabanaki, 2020) 35
3.1 Summary of laboratory test results per lithology (Ramli and Lucas, 2021) 39
3.2 Rock mass shear strength parameters used for analysis (Ramli and Lucas, 2021). 47
4.1 Summary of physical properties test results of BSH and VTF 54
4.2 Sieve number and sieve opening following the ASTM D422 standard..... 56
4.3 Mineral compositions of BSH and VTF by XRD. 59
4.4 Mineral compositions of BSH and VTF by X-ray fluorescence 60
5.1 Post-test BSH and VTF of direct shear test with various water contents..... 65
5.2 Peak shear stress and shear parameters of BSH for 390-570 mRL. 82
5.3 Peak shear stress and shear parameters of VTF 82
6.1 Summary of mechanical properties using in the simulation 84
6.2 Summary of cohesion and friction angle used in simulations for BSH and VT 85
6.3 Peak shear stress and shear parameters of BSH..... 93

LIST OF FIGURES

Figure **Page**

1.1 Research methodology. 3

2.1 Location of Phu Kham mine, Laos 8

2.2 Regional setting of the Phu Kham deposit, Laos (Fan, 2000) 9

2.3 Shear strength of sandy loam soil on Mohr-Coulomb diagrams with different water content (EI hariri et al., 2023). 12

2.4 Shear cohesion of sandy loam soil with varying water content (EI hariri et al., 2023) 13

2.5 Internal friction angle of sandy loam soil with varying water content (EI hariri et al., 2023) 13

2.6 Slope height decrease versus FoS (Shiferaw, 2021) 15

2.7 Types of slope failure a) base slide, b) toe slide, and c) slope slide (Shiferaw, 2021) 15

2.8 Variation of the crack initiation angle with the slope angle A) effect of side-pressure coefficient (K0) and B) effect of the side-friction coefficient (f) (Wang et al., 2023) 17

2.9 Variation of the slope safety height with crack length A) effect of side pressure coefficient (K0) and B) effect of the side-friction coefficient (f) Wang et al., (2023) 17

2.10 The lithology profile on schematic diagram (Zhao et al., 2023) 19

2.11 Calculation process of factor of safety slope by I) Bishop and II) Janbu method (Zhao et al, 2023)) 19

2.12 The changing of safety factor and failure location (Zhao et al., 2023) 20

LIST OF FIGURES (Continued)

Figure **Page**

2.13 Variation of the FOS with different locations and conditions (Zhao et al., 2023) 20
2.14 Comparison of shear strength parameters between the compacted and subjected to wetting-drying of kaolinite-quartz proportion: a) cohesion and b) friction angle (Charkley et al., 2019) 24
2.15 Examples of stability analysis of simplified Bishop and M-P method of each section and zone (Su et al., 2022) 26
2.16 Location of A and B model sections (Su et al., 2022).. 28
2.17 Cloud chart of safety factor and shear strain increment of model A (Su et al., 2022). 28
2.18 Cloud chart of safety factor and shear strain increment of model B (Su et al., 2022) 29
2.19 Dimension of the analyzed slope (Beyabanaki, 2020) 30
2.20 Case considered for weak layer: a) horizontal weak layer 5 m above toe, b) horizontal weak layer 1 m above toe, c) inclined weak layer with an angle of 29° with respect to horizontal, d) weak layer with an inclination of 57° (Beyabanaki, 2020) 30
2.21 FLAC modelling for case 1: a) model configuration and b) modeling results (Beyabanaki, 2020) 31
2.22 LEM analysis result for case 1 (Beyabanaki, 2020).. 31
2.23 FLAC modelling for case 2: a) model configuration and b) modeling results (Beyabanaki, 2020) 32
2.24 LEM analysis result for case 2 (Beyabanaki, 2020) 32

LIST OF FIGURES (Continued)

Figure **Page**

2.25 FLAC modelling for case 3: a) model configuration and b) modeling results (Beyabanaki, 2020) 33

2.26 LEM analysis result for case 3 (Beyabanaki, 2020) 33

2.27 FLAC modelling for case 4: a) model configuration and b) modeling results (Beyabanaki, 2020).. 34

2.28 LEM analysis result for case 4 (Beyabanaki, 2020). 34

3.1 Location of Phu Kham mine, Laos (Ramli and Lucas, 2021)..... 36

3.2 Location of failure on south wall at Phu Kham mine (Ramli and Lucas, 2021)..... 37

3.3 Upper part of south wall at Phu Kham mine (Ramli and Lucas, 2021)..... 37

3.4 Lower part of south wall at Phu Kham mine (Ramli and Lucas, 2021). 38

3.5 Lithologies and weathering boundary of the south wall at Phu Kham mine .. 39

3.6 Lithologies of the south wall at Phu Kham mine (Ramli and Lucas, 2021)..... 40

3.7 Geological faults and lithologies for south wall at Phu Kham mine (Ramli and Lucas, 2021)..... 41

3.8 Geological faults at south wall at Phu Kham mine (Ramli and Lucas, 2021)... 41

3.9 Plan of south wall fault network, ±100m slice at 450mRL level plan at Phu Kham mine (Ramli and Lucas, 2021)..... 42

3.10 South wall cross section, looking north at Phu Kham mine (Ramli and Lucas, 2021)..... 42

3.11 Black fault 16, faulted contact between VTF and IGN with clay alteration at the south wall, Phu Kham mine (Ramli and Lucas, 2021)..... 43

3.12 Key potential failure mechanism at the south wall, Phu Kham mine (Ramli and Lucas, 2021)... 43

LIST OF FIGURES (Continued)

Figure **Page**

3.13 Slide3 model at south wall, looking south (Ramli and Lucas, 2021) 46
3.14 FoS for south wall, base case fault strength (Ramli and Lucas, 2021) 48
3.15 FoS for south wall, fault strength sensitivity case (Ramli and Lucas, 2021) 48
3.16 FoS for south wall, groundwater sensitivity case (Ramli and Lucas, 2021)..... 49
4.1 Collection of drilling samples at PKGT0093... 51
4.2 Location of collected samples at side wall, Phu Kham mine, Laos 55
4.3 Sand cone test of the BSH sample at Phu Kham mine... 56
4.4 Sand cone test of the VTF sample at Phu Kham mine.... 57
4.5 Grain size distribution of BSH..... 57
4.6 Grain size distribution of VTF..... 58
4.7 X-ray diffraction apparatus at Suranaree University of Technology 58
4.8 X-ray fluorescence apparatus at Suranaree University of Technology 59
5.1 BSH sample under dry condition for direct shear test..... 62
5.2 VTF sample under dry condition for direct shear test 63
5.3 Direct shear test apparatus at Suranaree University of Technology laborator 63
5.4 Relationships of shear stress with displacement (a) and shear stress with normal stress of BSH at 0% water content condition 66
5.5 Relationships of shear stress with displacement (a) and shear stress with normal stress of BSH at 5% water content condition 67
5.6 Relationships of shear stress with displacement (a) and shear stress with normal stress of BSH at 10% water content condition..... 68
5.7 Relationships of shear stress with displacement (a) and shear stress with normal stress of BSH at 15% water content condition..... 69

LIST OF FIGURES (Continued)

Figure **Page**

5.8 Relationships of shear stress with displacement (a) and shear stress with normal stress of BSH at 20% water content condition 70
5.9 Relationships of shear stress with displacement (a) and shear stress with normal stress of BSH at 25% water content condition 71
5.10 Relationships of shear stress with displacement (a) and shear stress with normal stress of BSH at 30% water content condition 72
5.11 Relationships of shear stress with displacement (a) and shear stress with normal stress of BSH at 35% water content condition 73
5.12 Relationships of shear stress with displacement (a) and shear stress with normal stress of VTF at 0% water content condition 74
5.13 Relationships of shear stress with displacement (a) and shear stress with normal stress of VTF at 5% water content condition 75
5.14 Relationships of shear stress with displacement (a) and shear stress with normal stress of VTF at 10% water content condition 76
5.15 Relationships of shear stress with displacement (a) and shear stress with normal stress of VTF at 15% water content condition 77
5.16 Relationships of shear stress with displacement (a) and shear stress with normal stress of VTF at 20% water content condition 78
5.17 Relationships of shear stress with displacement (a) and shear stress with normal stress of VTF at 25% water content condition 79
5.18 Relationships of shear stress with displacement (a) and shear stress with normal stress of VTF at 30% water content condition 80
5.19 Relationships of shear stress with displacement (a) and shear stress with normal stress of VTF at 35% water content condition 81

LIST OF FIGURES (Continued)

Figure **Page**

5.20 Shear strength as a function of water content of BSH (a) and VTF (b) at different normal stress 83
6.1 Boundary conditions of exposed BSH on slope (a) and unexposed BSH on slope (b). 85
6.2 Factor of safety as a function of slope face angles under various water contents of BSH and VTF, and slope heights at 50m (a) and 100m (b) 88
6.3 Factor of safety as a function of slope face angles under various water contents of BSH and VTF, and slope heights at 150m (a) and 200m (b) 89
6.4 BSH plane do not appear as low slope height condition at (a) slope height 50m, slope face 20° and (b) slope heights 100m, slope face 30° 90
6.5 BSH plane do not appear as steep slope face condition at (a) slope face 40° slope height 150m and (b) slope face 50°slope heights 200m 91
6.6 BSH plane appears at (a) slope face 20°, slope height 100m and (b) slope face 30°, slope height 150m. 92
6.7 Factor of safety as a function of water contents of VTF under various slope heights with slope face angles at 20° (a) and 30° (b) 94
6.8 Factor of safety as a function of water contents of VTF under various slope heights with slope face angles at 40° (a) and 50° (b) 95
6.9 Factor of safety as a function of water contents of VTF under various slope heights with slope face angles at 60° 96
6.10 Predicted factor of safety as a function of water contents, slope face angles, and slope heights. 97

LIST OF FIGURES (Continued)

Figure **Page**

7.1 Comparison of empirical equation with different numerical simulation models at cohesion 23.54 kPa and friction angle 37 degrees of VTF material. 100

7.2 Comparison of empirical equation with different numerical simulation models at cohesion 33.47 kPa and friction angle 32 degrees of VTF material 100

มหาวิทยาลัยเทคโนโลยีสุรนารี

LIST OF ABBREVIATIONS

τ	=	Shear strength
c'	=	Effective cohesion
σ	=	Total stress
u_w	=	Pore water pressure
ϕ'	=	Effective fiction angle
σ-u_a	=	Net normal stress
ϕ^b	=	Friction angle with respect to matric suction
u_a	=	Pore air
FOS	=	Factor of safety
K	=	Factor of safety of circular sliding surface
c_i	=	Cohesion force of block No
φ_i	=	internal friction angle of block No i
W_i	=	Weight of block No i and overlying tailings
L_i	=	Bottom edge length of block No i
Q_i	=	Horizontal force acting on block No i
α_i	=	Angle between the bottom edge of block No i
U_i	=	Horizontal plane of coordinate axis on block No i
X	=	Tangential force between soil strips

มหาวิทยาลัยเทคโนโลยีสุรนารี

LIST OF ABBREVIATIONS (Continued)

E	=	Normal force between soil strips
λ	=	Constant
μ	=	Poisson Ratio
c	=	Cohesion
φ	=	Friction angle
UCS	=	Unconfined compressive strength
TXL	=	Triaxial compressive strength
DS	=	Direct shear
w	=	Percentage of water content
W_s	=	Mass of soil at the field
W_d	=	Mass of dry soil
G_s	=	Specific gravity
γ_s	=	Density of soil
γ_w	=	Density of water
γ_c	=	Density of sand
γ_d	=	Dry density
LL	=	Liquid limit
PL	=	Plastic limit
PI	=	Plastic index
σ_n	=	Normal stress
ψ	=	Slope face angle
H	=	Slope height

มหาวิทยาลัยเทคโนโลยีสุรนารี

LIST OF ABBREVIATIONS (Continued)

FS = Factor of safe

มหาวิทยาลัยเทคโนโลยีสุรนารี

CHAPTER I
INTRODUCTION

1.1 Background and Rationale

Phu Kham Mining is a copper and gold open pit excavation, which is operated by PanAust's Phu Bia Mining Contract at Xaisombon, Vientiane, Laos. An unstable slope is found at the south wall of the pit. The weak zone on the sidewall is mudflow type including black fault (BSH) and volcanic tuff (VTF). The general factors controlling soil slope stability are groundwater, slope geometries, soil mechanical properties, structural geology, and excavation activity. The slope stability of the sidewall is mainly controlled by the water contents of mudflow and slope characteristics. Several researchers have studied the effects of water contents on weak material. Gusman et al. (2018) and Pei et al. (2020) find that the amount of rainwater could affect slope stability. Liu et al. (2020) indicate that collapsing erosion occurred faster with higher water contents and steeper slope angles. The 3D limit equilibrium model is investigated during rainfall conditions and shows significant impacts of wetting depth followed by the permeability coefficient, moisture content, suction head, rainfall intensity, and slope angle (Liu et al., 2021). Even though the effects of water content on slope stability have been studied by many researchers, the effort of safety factor prediction for specific pit slope design of Phu Kham open pit under various water contents and slope geometries has never been attempted.

1.2 Research Objective

The objective of this study is to determine the shear strength parameters of mudflow material at the sidewall of Phu Kham mine under various water contents (0, 5, 10, 15, 20, 25, 30, and 35% by weight) by performing a direct shear test. The test

results are simulated in a numerical model with a limit equilibrium method using SLIDE 2D software under different slope heights and slope face angles. Empirical solutions obtained from simulation results are developed for use to predict the long-term slope behavior in the dry and rainy seasons.

1.3 Scope and Limitations

The scope and limitations of this study include as following:

1) Weak material (mudflow) samples including BSH and VTF are collected from the field at Phu Kham mine, Laos.
2) A water content test is conducted following ASTM D2216 standard practice.
3) Atterberg's limit test is conducted following ASTM D4318 standard practice.
4) Grain size analysis is conducted following ASTM D422 standard practice.
5) Sand cone test is conducted following ASTM D1556 standard practice.
6) Specific gravity is conducted following ASTM D854 standard practice.
7) Mineral compositions are analyzed by using the X-ray Diffraction method (XRD).
8) Element compositions are analyzed by using the X-ray Fluorescence method (XRF).
9) Direct shear test is performed under ASTM D3080 standard practice with various water contents of 0, 5, 10, 15, 20, 25, 30 to 35% by weight.
10) Numerical analyses using Slide2D software are performed to assess the stability of the designed slopes. The results are used to develop empirical equations for a guide announcement of stability conditions.

1.4 Research Methodology

The research methodology (Figure 1.1) is divided into 8 steps, including literature review, sample collection, and preparation, chemical properties analyses (XRF and XRD analyses), physical properties test (grain size analysis, water content test, specific gravity, sand cone test, and Atterburge's limit test), direct shear test, numerical model simulation, analysis of test results, discussions, conclusions, and thesis writing.

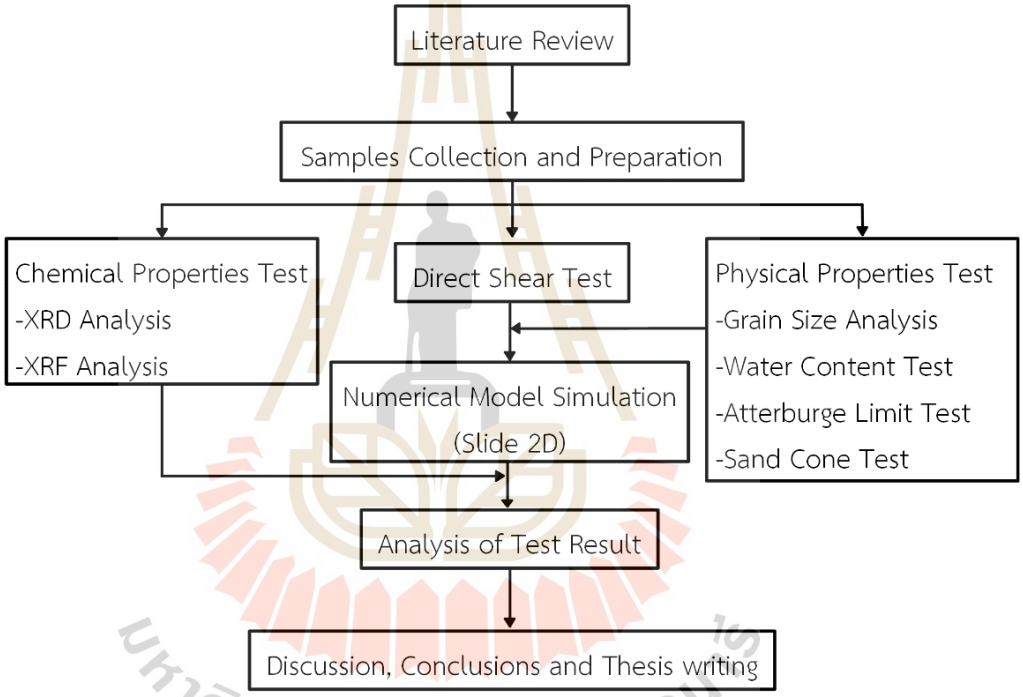


Figure 1.1 Research methodology.

1.4.1 Literature Reviews

The literature review is carried out to improve an understanding of water content on the direct shear test of mudflow. The topics reviewed here include the effect of mudflow material at Phu Kham mine, the effect of water content on weak material, the effect of slope characters on slope stability, the effect of mineral composition on slope stability, and computer simulations of slope stability that affect water content with mudflow movement. The sources of information are from journals, technical reports, and conference papers.

1.4.2 Study area

The south wall was studied by a consultancy company. This topic reviewed study results including the location of the mine, failure of the south wall, lithology and structure control at the south wall, and stability analysis at the south wall. This report provides the information to design the pit shell of the Phu Kham mine.

1.4.3 Samples collection and preparation

The samples at Phu Kham mine are used in this study. Sample preparation is carried out at the Suranaree University of Technology and Phu Khum Mine laboratory.

1.4.4 Chemical properties

The chemical properties are determined by XRF and XRD analyses, which are performed on finely soil powder pressed into coherent pellets. The analysis is performed under initial conditions. The results identify the quantity of elements and mineral compositions which leads to revealing the effect of water content on the material.

1.4.5 Physical properties test

The physical properties are determined by water content tests (ASTM D2216), Atterberge's limit test (ASTM D4318) grain size analysis (ASTM D422), specific

gravity (D854), and sand cone test (ASTM D1556), following ASTM standards practice of the mudflow samples test. The samples are determined for the properties at the initial stage. The results are presented under different physical properties of each sample.

1.4.6 Direct shear test

The direct shear test determines the shear strength parameters of soil. The test procedure follows the relevant ASTM D3080 standard practice with various water content of 0, 5, 10, 15, 20, 25, 30 to 35% by weight. The results identify strength properties by using a numerical simulation process.

1.4.7 Numerical model simulation

The limit equilibrium software, Slide2D uses the slope mine characteristics for investigation of the effects of high wall mine and water content on mudflow properties. The test results obtained from physical and mechanical tests are used as parameters in the simulation.

1.4.8 Analysis of test result

The results of numerical simulation models in terms of the water content and shear strength are compared against the results of chemical tests (XRD and XRF tests), and mudflow properties. The possibility for effect on mudflow behavior conditions in different parameters models with varying water content results is analyzed and related by simulation results. The results are used to develop an equation for predicting weak zone behavior as affected by water content and relevant conditions.

1.4.9 Discussions and conclusions

Discussions are made on the reliability and adequacies of the approaches used here. Future research needs to be identified. All research activities, methods, and results are documented and complied with in the thesis. The research or findings are published in the conference proceedings.

1.5 Thesis Contents

The first Chapter introduces the background of problems and significance of the study, identifying the research objectives, scope and limitations, and research methodology. The second Chapter summarizes the results of the literature review. Chapter three describes the details of the study area. Chapter four describes the rock sample collection and results of chemical property and physical properties tests. Direct shear testing and test results are presented in Chapter Five. Chapter six shows the simulation results of the numerical model and analysis of test results. Chapter seven provides discussion, conclusions, and recommendations for future studies.

มหาวิทยาลัยเทคโนโลยีสุรนารี

CHAPTER II

LITERATURE REVIEW

2.1 Introduction

This chapter summarizes the results of the literature review carried out to improve an understanding of the effect of the water content of mudflow on direct shear tests. The topics are reviewed here, including the effect of mudflow material at Phu Kham mine, the effect of water content on weak material, the effect of slope geometry on its stability, the effect of mineral compositions on slope stability, and computer simulations on slope stability.

2.2 Effect of mudflow material at Phu Kham mine

Phu Kham mining is copper and gold open pit excavation, which is operated by PanAust's Phu Bia Mining Contract at Xaisombon, Vientiane, Laos (Figure 2.1). The deposit of Phu Kham occurs near the intersection of the Truongson fold belts and Loei-Phetchabun/ Louangphabang which formed the west and northeast margins, respectively of the Khorat-Kontum terrane in Figure 2.2 (Fan, 2000). The mineralization deposit includes sulfide and silicate-oxide skarn and stockwork mineralization styles in a layer of intermediate volcaniclastics with Permo-Carboniferous interbedded limestone. The host sequence is classified from a basement redbed siltstone on footwall and granite material by a low angle thrust fault (Mao et al., 2005). Mineralization mainly occupies and hosts within thrust fault hanging walls associated with schist (skarn bordering limestone), diorite bodies, breccia, and intermediate porphyry dykes (Soysouvanh et al., 2016). The unstable slope is found at the south wall of Phu Kham mine. The weak zone on the sidewall is mudflow which includes black fault or thrust fault material (BSH) and volcanic tuff or schist (VTF).

The slope stability at the south wall depends on the mudflow characteristics. They have high porosity and low permeability which are different general soil characteristics. The mudflow is classified as medium to high plasticity clay which has an average clay content of about 59%. The weak material with high clay content is sensitive to water. The mine had been depressurized by groundwater removal in the wall however could not be used by the sub-horizontal drain method.

The hydrologic investigation was made by permeability test by Guelph permeameter instrument. The results show permeability values at the south wall that BSH is 5.79x10-3 m/day and VTF is 4.75x10-2 m/day which are classified as very low permeability (Pramuji, 2015). The mudflow is sensitive water leading to instability of the slope on the south wall, of the Phu Kham mine. Many times, the mine was redesigned and supported slope stability methods on the south wall, but they could not solve this problem.



Figure 2.1 Location of Phu Kham mine, Laos.

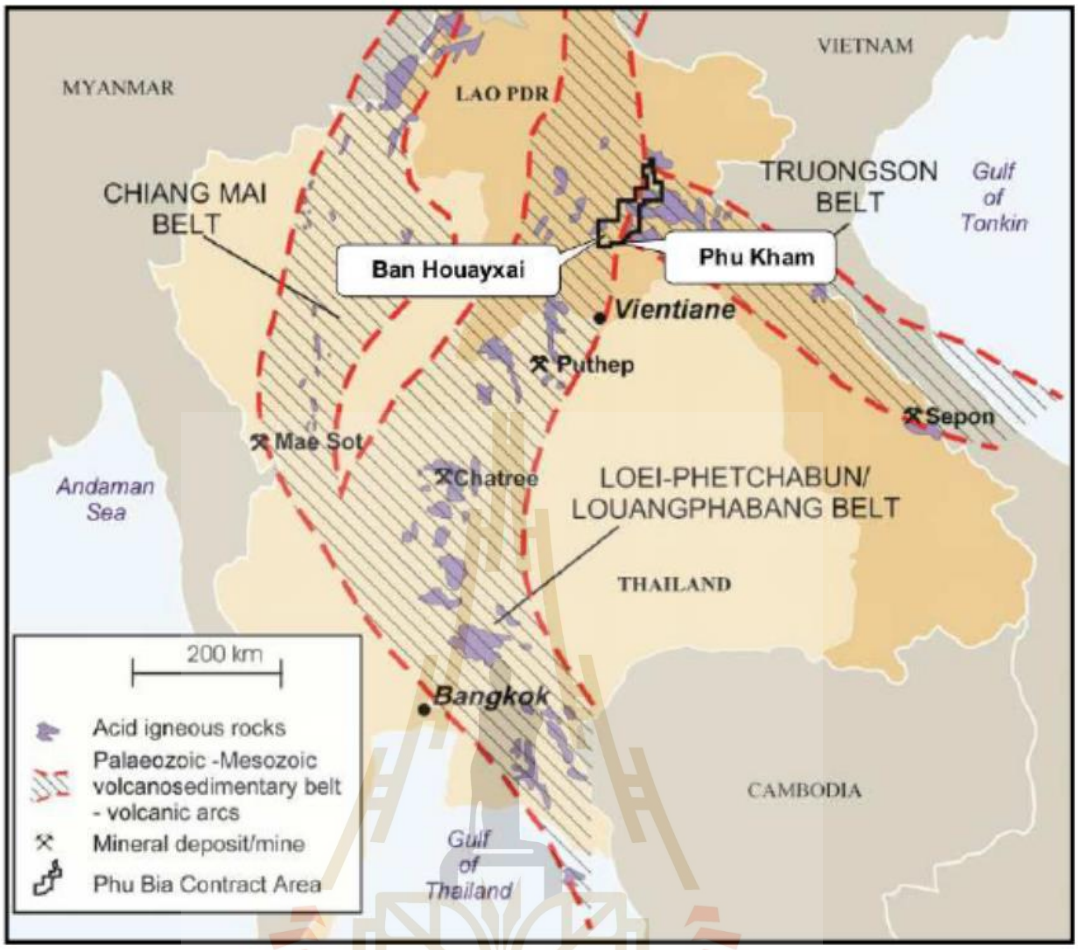


Figure 2.2 Regional setting of the Phu Kham deposit, Laos (Fan, 2000).

2.3 Effect of water content on weak material

The open pit mines have many troubles in the rainy season which cannot be protected against the natural condition. The influence of changing of water content of soil directly affects physical and mechanical properties. In the rainy season, increasing the water content of ground mass to the saturated condition can reduce soil shear strength due to increasing pore-water pressure and the appearance of some failure of mine wall if the material is not suffered by increasing water content. The water content has significantly affected slope characters but the material slope of the Phu Kham mine has rarely been studied.

Many researchers investigate the pattern of change in the shear strength with varying water content for soil material (Yong et al., 2023; Wang et al., 1990; Li et al., 2021). The result indicates that water content is increasing with decreased cohesion and internal friction of soil on the direct shear test. The case of study impacts of rainfall has confirmed slope instability due to high water content in soil material (Hao et al., 2023).

Liu et al. (2021) study a new Green-Ampt model of the infiltration process based on fractional derivative and application in 3D analysis of slope stability. They found six parameters that affected fractional derivatives. The parameters are wetting front depth, water content, permeability coefficient, rainfall intensity, suction head, and slope angle. Liu et al. (2020) studied pore water pressure, water content, and wetting front in residual soil of granite during collapsing erosion with different slope angles. The results indicate that collapsing erosion of granite residual soil occurs faster with steeper slope angles by artificial rainfall in subtropical regions. The water content between 30-40% of weight occurs toward the upslope direction of collapse due to increasing pore-water pressure and then soil mass is collapsed. The slope angle affects the infiltration process during collapsing erosion during the rainy season.

Gusman et al. (2018) indicate that increasing water content significantly affects slope stability causing decreasing cohesion and friction angle based on soil test results. The relationship of water content with cohesion and fiction angle is a simple linear equation. The slope stability at Sitinjau Lauik Kota Padang is a safe condition between water content from 0 to 50% but if at 50 reaching the maximum at 73.74% of water content is potential for failure. The height of the slope can lead to an increase in surface runoff, but slope stability decreases because rainfall infiltration leads to an increase of water content volumetric to reduce unsaturated soil shear strength (Pei et al., 2020).

Zhang et al. (2020) indicate that the shear strength of granitic soil decreases with decreasing normal stress and/or increasing soil water content caused by the

increase of water content which is more distinguished from the lower fractal dimension of soil. The water has a greater impact on soil shear strength parameters than the fractal dimension in the south, China. Additionally, Zhang et al. (2001) studied surface soil shear strength which is affected by bulk density and water content of soil at dominated material in subtropical China. They find that the dominant influence of bulk density on soil strength is small ranging from 0.01-0.09g cm-3. The change of soil shear strength parameters with different bulk density and soil water content are described by Mohr-Coulomb's failure equation and effective stress principles of unsaturated soils. The linear function of Mohr-Coulomb's equation for saturated soils in effective stress is given as:

$$\tau = c' + (\sigma - u_w) \tan\phi' \quad (2.1)$$

where τ is shear strength, c' is the effective cohesion, σ is total stress, u_w is pore water pressure and ϕ' is effective fiction angle.

Equation of shear strength for unsaturated soils is developed by Fredlund et al. (1978) as:

$$\tau = c' + (u_a - u_w) \tan\phi^b + (\sigma - u_a) \tan\phi' \quad (2.2)$$

where $\sigma - u_a$ is net normal stress, ϕ^b is friction angle with respect to matric suction, u_a is pore air, u_w is water pressure.

El Hariri et al. (2023) have conducted experiment in sandy loam soil shear strength parameters under different water contents in Hungary country. They find the factor of safety of the change slope with varying cohesion and friction angle parameters from the direct shear test. The shear strength parameters grow up as a linear function with increasing normal stress as shown in the drawing of Mohr-Coulomb in Figure 2.3. The water affects shear cohesion and friction angle from the shearing test. The relationship of shear cohesion increases until reaching a maximum point of 27.17 kPa, (at 11.25% of water content), and then the graph goes down with

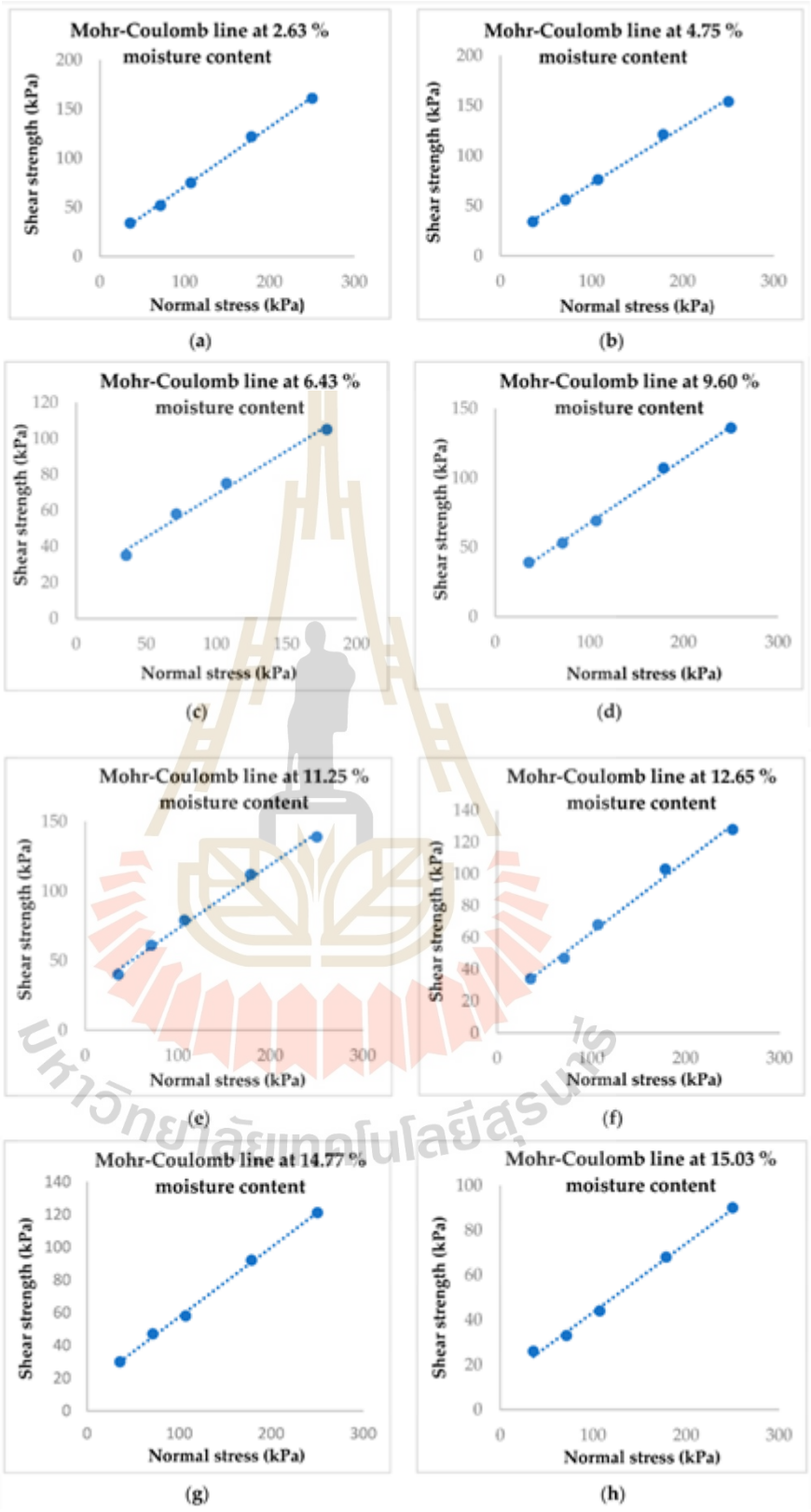


Figure 2.3 Shear strength of sandy loam soil on Mohr-Coulomb diagrams with different water content (EI hariri et al., 2023).

increasing water content in Figure 2.4. The frictional angle diagram decreases continuously with increasing water content in Figure 2.5.

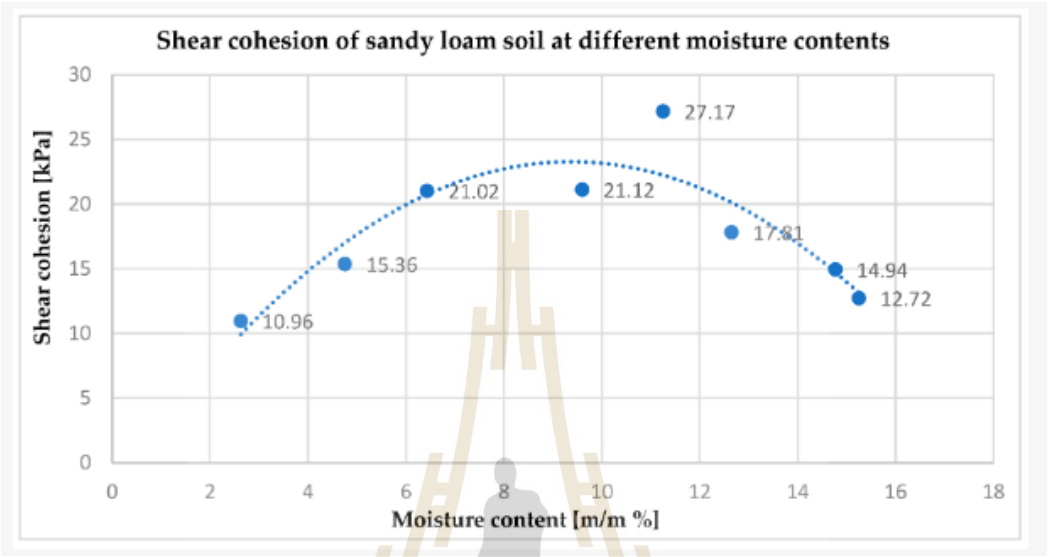


Figure 2.4 Shear cohesion of sandy loam soil with varying water content (EI hariri et al., 2023).

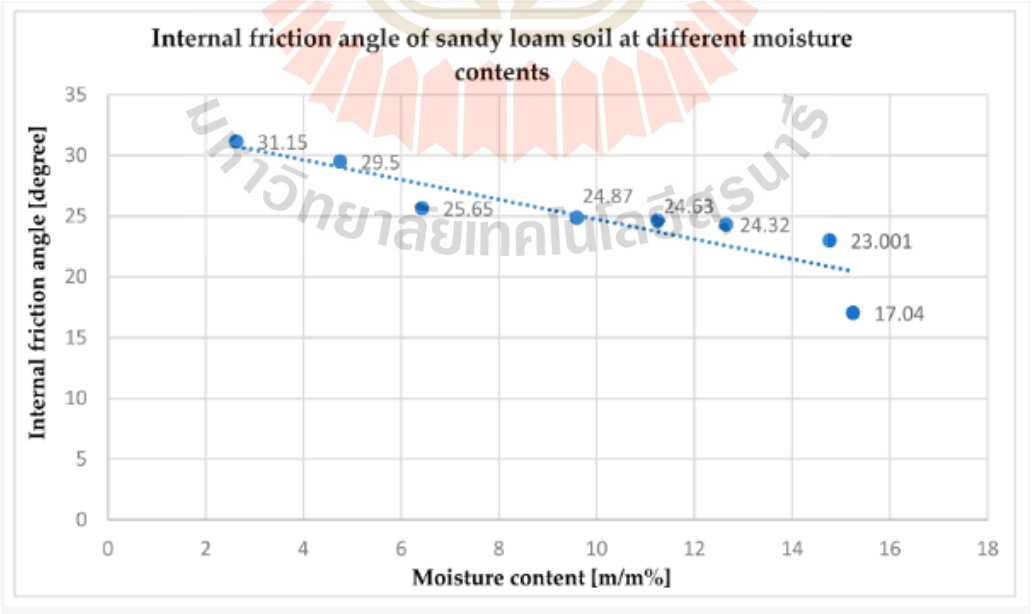


Figure 2.5 Internal friction angle of sandy loam soil with varying water content (EI hariri et al., 2023).

2.4 Effect of slope characters on stability of slope

Slope of the mine is stable before excavation leading to an unstable slope due to excavation. The mass of soil failure is called slide or slope failure. The cases of failures include undercutting the foot of the slope, excavation, gradual disintegration of soil structure, and increasing pore pressure (Huang, 2012). The main conditions of instability slope of open pit mines are affected by excavation from human activity (slope height and slope angle parameters) and controlled nature (structurally controlled failures and coefficients of variation of soil strength parameters).

Shiferaw (2021) studies the effect of slope height and slope angle on the factor of safety and failure shape of slope based on the reduction of strength. Results indicate that the stability of slope increases with the decrease of slope height and slope angle. The different rate of increasing stability of the slope depends on soil types and the geometry of the slope. The decrease of slope height to less than 3 m tends to be an increasing factor of safety as shown in Figure 2.6. The influence of decreasing slope angle with increasing factors of safety is approximately linear and the correlation coefficient indicates a strong relation in Table 2.1. The rotational slide has 3 types which occur in fine-grained and homogeneous soil (Figure 2.7). The first base slide occurs from the boundary of the criteria surface over an arc inclosing of entire slope. The second toe slide occurs from the boundary of the criteria surface arch passing through the toe of the slope and finally slope sliding from the boundary of the criteria surface occurs on the slope surface.

Wang et al. (2023) study failure mechanisms and stability of slope analysis of the Danushan open-pit slope under unloading conditions from excavation. They find crack initiation angle increasing due to the increase of side pressure coefficient, slope angle, and friction angle. The increasing initiation angle crack leads to the occurrence of failure accidents during the unloading and excavation (instability) of slope open-pit mines. Figure 2.8 shows initiation angle crack increases with increasing slope angle. The slope angle is less than 50° with increases dramatically initiation angle crack because horizontal stress and horizontal unloading have more effect on the crack propagation. The ultimate safety slope height decreases linearly with increasing crack length

because increasing crack length leads to the increased fracture risk of the cracked rock mass under unloading (Figure 2.9).

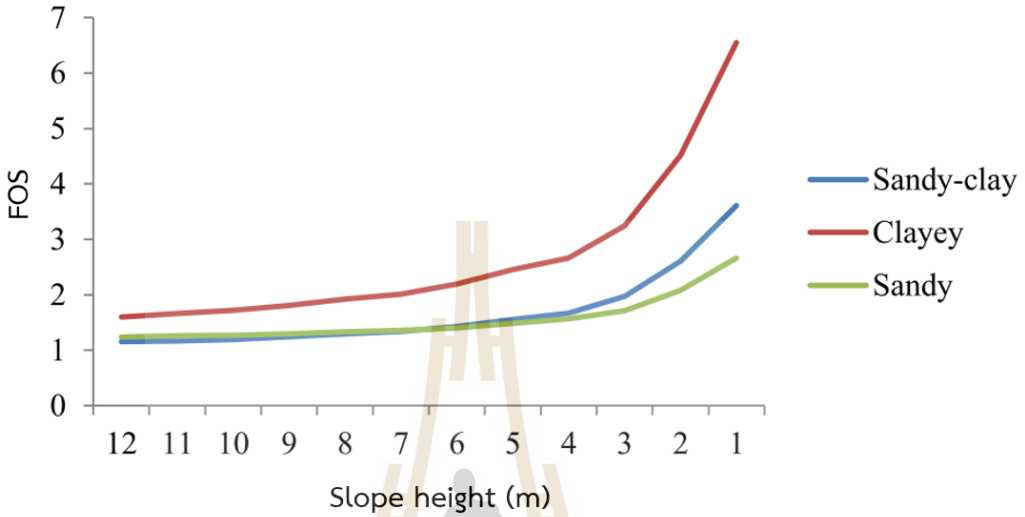


Figure 2.6 Slope height decrease versus FoS (Shiferaw, 2021).



Figure 2.7 Types of slope failure a) base slide, b) toe slide, and c) slope slide (Shiferaw, 2021)

Table 2.1 Slope angle and factor of safety (Shiferaw, 2021).

α	tan α	FOS		
		Sandy-Clay	Clayed	Sandy
36.87	0.75	0.9231	1.3978	0.9096
33.69	0.667	1.0363	1.5426	1.0425
30.96	0.600	1.1466	1.6392	1.1640
28.61	0.545	1.2547	1.7364	1.2942
26.56	0.500	1.3566	1.8437	1.4250
24.78	0.462	1.4393	1.9469	1.5616
23.20	0.429	1.5211	2.0364	1.7254
21.80	0.400	1.5995	2.1268	1.8564
20.56	0.375	1.6930	2.2294	1.9837
19.44	0.353	1.7933	2.3296	2.1049
18.43	0.333	1.8677	2.4187	2.2181
17.53	0.316	1.9471	2.5094	2.3365
r		-0.9824	-0.9787	-0.9730

มหาวิทยาลัยเทคโนโลยีสุรนารี

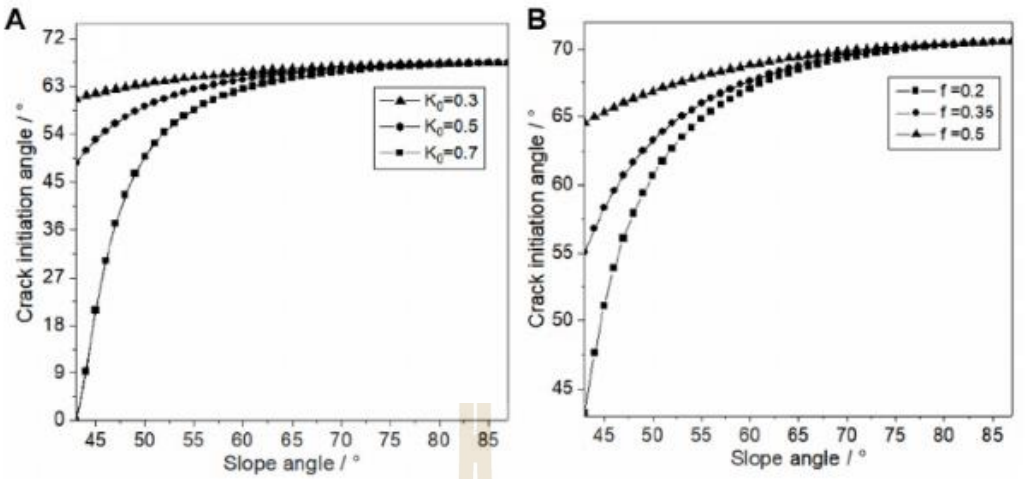


Figure 2.8 Variation of the crack initiation angle with the slope angle A) effect of side-pressure coefficient (K0) and B) effect of the side-friction coefficient (f) (Wang et al., 2023).

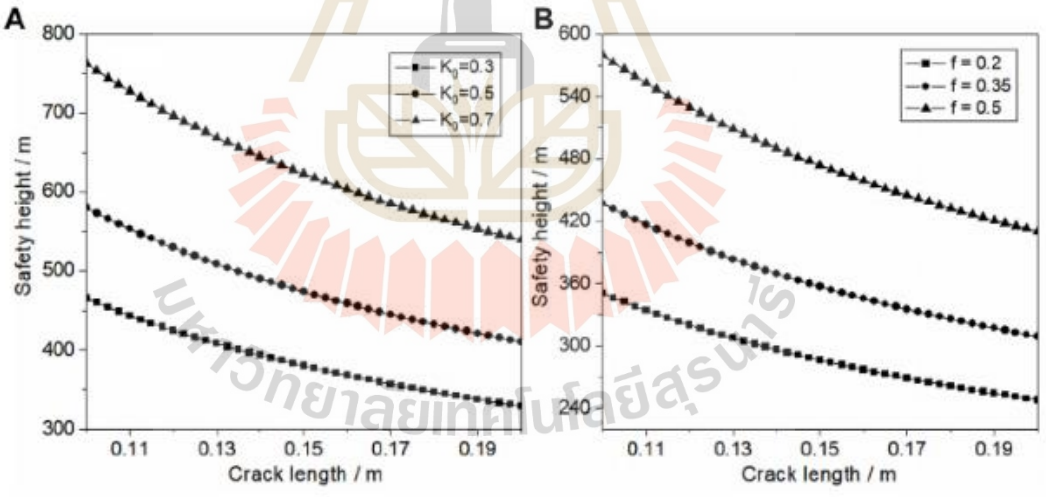


Figure 2.9 Variation of the slope safety height with crack length A) effect of side pressure coefficient (K0) and B) effect of the side-friction coefficient (f) (Wang et al., 2023).

Zhao et al. (2023) studied the factor of safety of heterogeneous slopes in the north and south metal open-pit mine of Tanjianshan gold mine, China. They find the factor of safety of heterogeneous rock slope and the homogeneous slope is sensitive to the bench face angle and varying failure types. The failure of a homogeneous slope for low strength material is normally a local failure ranging from a few to tens of meters and high strength material is the failure of the whole slope. The heterogeneous slopes normally expose failures in weak material or fault, so the failure is localized landslides. The models are simulated by the properties in Table 2.2 and lithologies in Figure 2.10. The bench face angles depend on each location as shown in Figure 2.8 including a) initial design slope, b) modifying slope (65°-55°), c) modifying slope (55°-50°), d) modifying slope (50°-49°), e) modifying slope (50°-49°), f) modifying slope (49°), g) modifying slope (48°), h) modifying slope (45°), i) modifying slope (43°), j) modifying slope (42°), k) modifying slope (41°). The six conditions are calculated as shown in Figures 2.11 and 2.12. The factor of safety do not show increasing linearly with the decrease of slope angle (Figure 2.13) due to different location and lithologies leading to a different factor of safety.

Table 2.2 The mechanical and physical properties of rockmass (Zhao et al., 2023).

Lithology code	**Lithology**	**Density (kg/m^3)**	**E (GPa)**	**Poisson's ratio**	**Tensile strength (MPa)**	**C (MPa)**	**Friction angle (Degree)**
TDP	Marble	2,750	9.63	0.19	0.14	0.31	31.49
MGG	Gabbro	2,750	14.14	0.31	0.61	0.61	27.8
TPO	Phyllite	2,750	2.4	0.1	0.03	0.06	23.96
Gravels	Gravels	2,000	0.5	0.45	0	0.015	30
Fault/ shear	Fault/ shear	2,750	2.5	0.4	0.004	0.025	15.3
Average	-	2,727	3.2	0.17	0.038	0.083	23.6

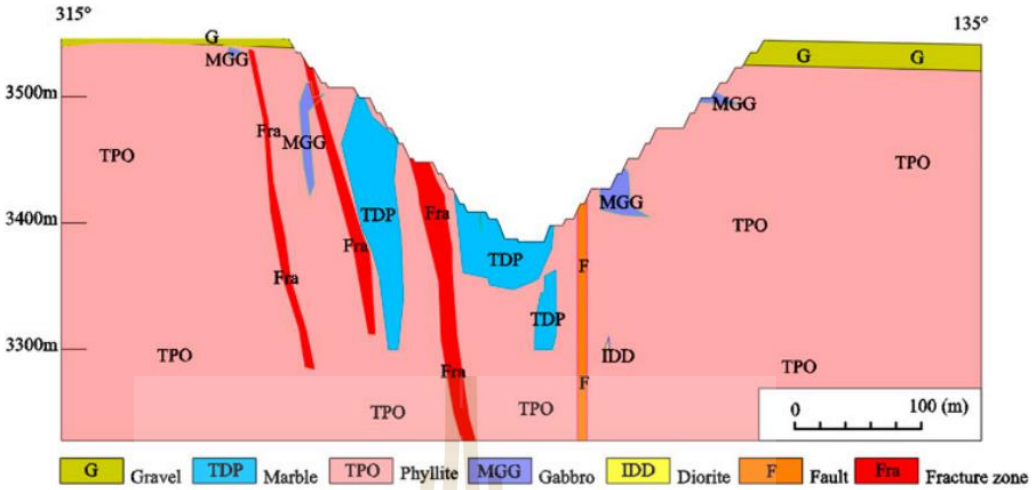


Figure 2.10 The lithology profile on schematic diagram (Zhao et al., 2023).

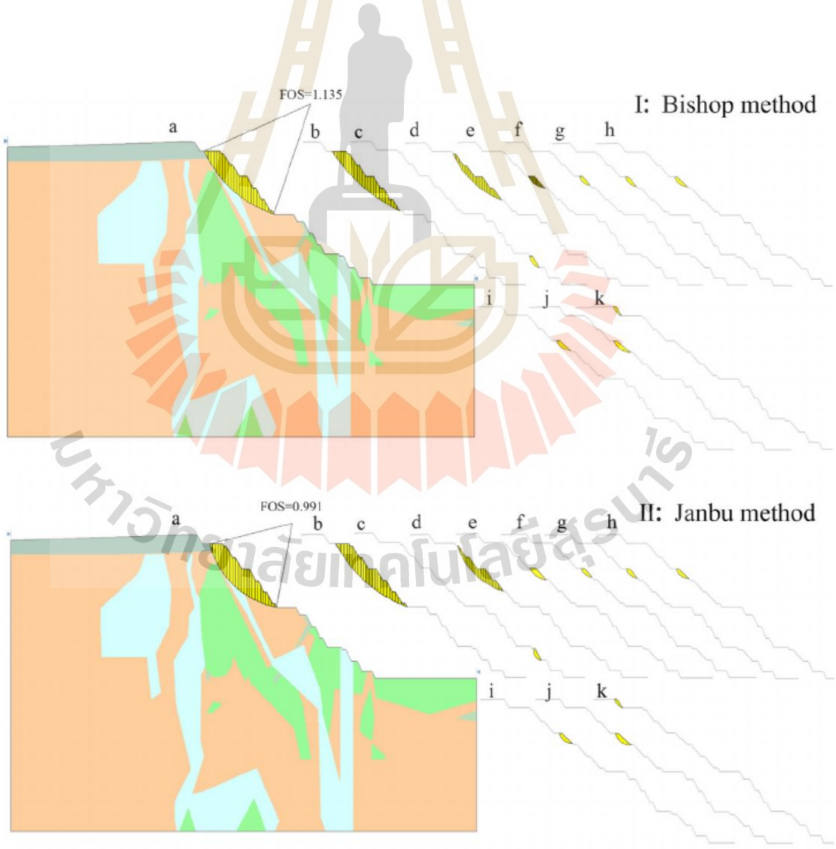


Figure 2.11 Calculation process of factor of safety slope by I) Bishop and II) Janbu method (Zhao et al., 2023).

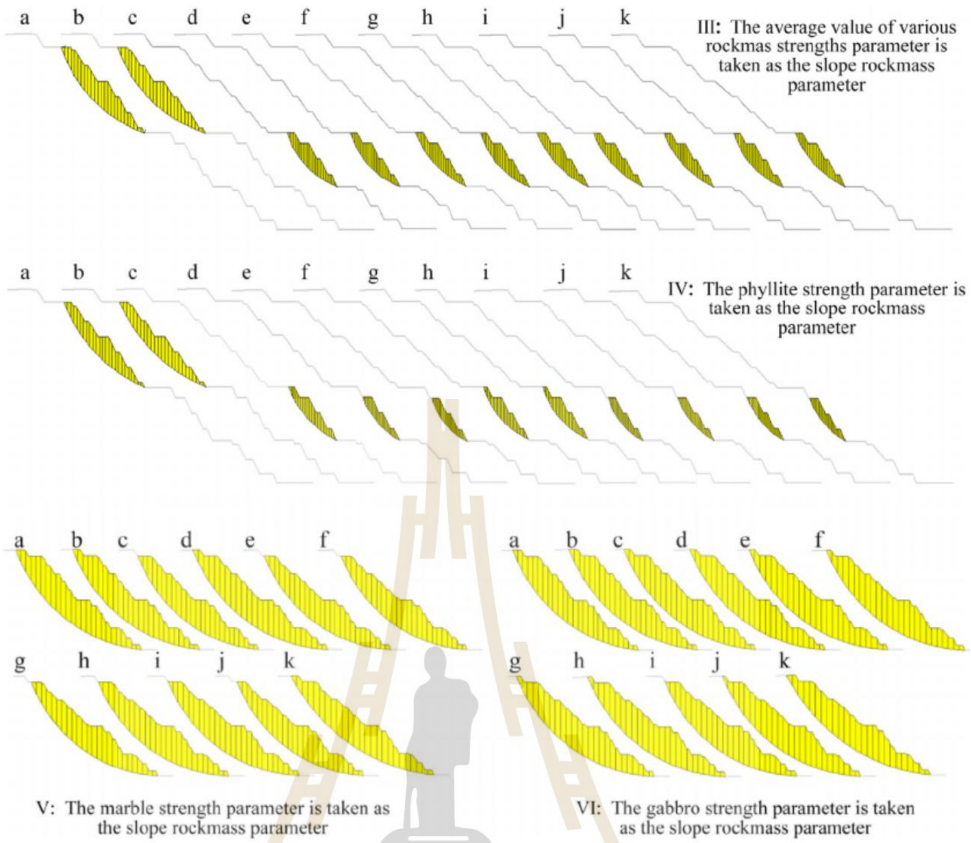


Figure 2.12 The changing of safety factor and failure location (Zhao et al., 2023).

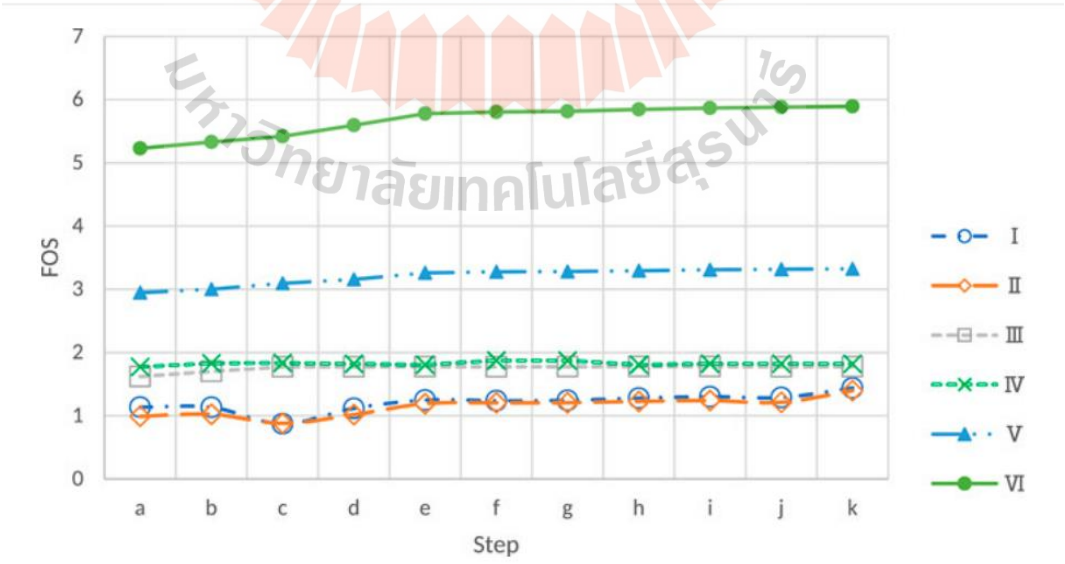


Figure 2.13 Variation of the FOS with different locations and conditions (Zhao et al., 2023).

2.5 Effect of mineral compositions on slope stability

Quartz is high durability which is durable on weathering (Fahy and Guccions, 1979; Gunsallus and Kulhawy, 1984; Shakoor and Bonelli, 1991). For soil minerals, the grain size is lower than 0.002 millimeters including talc, mica, chlorite, and smectite. Generally, the surface of soil minerals is a negative electrical charge which is able to balance by absorbtion of the positive electrical charge of solutions (Mitchell, 1993). A significant property of soil minerals is swelling which ability of swilling minerals are from high to low as montmorillonite, illite, halloysite, and kaolinite. Additionally, the swelling of atoms is high to low as lithium, potassium, calcium, magnesium, and hydrogen. The swelling could reduce the durability of weathering but it slightly affects the strength.

Charkley et al. (2019) studied the effect of mineral contents on the shear strength of 11 artificial compacted quartz and clay mixtures (kaolinite and montmorillonite) under wet-dry cycles. Results indicate that the cohesion and friction angle are associated with clay minerals proportion and several wetting and drying cycles. Generally, kaolinite dominated mixtures are more sensitive to the changes in cohesion strength parameters than dominated montmorillonite mixtures, and the reduction of friction angle is insignificant. Observation of increasing kaolinite proportion leads to increasing cohesion and decreasing friction angle. The cohesion increases from 67.7 up to 97.7 kPa while the friction angle decreases from 30.4° to 18.9° for kaolinite 30% up to kaolinite 70%, respectively. For kaolinite 70% until 100% results show a decrease in friction angle and cohesion as shown in Figure 2.14. The friction angle and cohesion from the direct shear test are affected by clay mineral proportions. The drying-wetting process on specimens is dramatically reduced in all clay mixtures.

Ioanna et al. (2009) investigated the geotechnical and mineralogical properties of weak rocks from Central Greece. Results indicate that the geotechnical behavior of weak rock is associated with mineral composition and texture. Durability and strength are found to be influenced by high percentages of carbonate minerals and/or reduction of clay mineral content. Research on the prediction of the long-term

influence of strength of weak rocks by Fuenkajorn and Sri-in (2009) indicates the relationship of mineral composition from test results that clastic rocks and schist which contain a high percentage of kaolinite in matrix tend to degrade much quicker than other material under water influences with slake durability testing. The slaty shale with high mica content is disintegrated easily under wet condition as well.

2.6 Computer simulations of slope stability

Slope stability is crucial considered the potential slope failure which can destroy the building construction and harm to human activities. The computer simulation is one method for estimating likelihood of slope failure in advance due to preventing the hazards to human live. The limit equilibrium method is a conventional method used to analyse factors of safety. This method is many published models to use as Janbu (1954), Bishop (1955), Nonveiller (1965), Morgenstern and Price (1965) and Sarma (1979). The soft material is always occurred by circular failure which is described the detail of stability analysis of the simplified Bishop and Janbu method by Huang (2012).

Su et al. (2022) studied the steep slope stability and slope angle optimization of open-pit slopes based on the limit equilibrium method and numerical simulation at K mine in Myanmar. Results indicate that the factor of safety of the designed slope is higher than the allowable slope stability by using limit equilibrium analysis which is the stable slope. The limit equilibrium analysis method which used mechanical parameters detailed in Table 2.3 is calculated by simplified Bishop (B) and Morgen Prince (M-P) method on A, B, C, and D areas, respectively representing the East, South, West, and North area of K open-pit mine. The results of the limit equilibrium method are in Figure 2.15 and Table 2.4. The equations of simplified Bishop and Morgen-Prince methods can be expressed as:

$$K = \frac{\sum_i \left[c_i L_i + \left(W_i \sec \alpha_i - U_i L_i \right) \right] \frac{1}{1+\tan \varphi_i \tan \alpha_i / K}}{\sum_i \left(W_i \sin \alpha_i + Q_i \cos \alpha_i \right)} \quad (2.3)$$

where K is factor of safety of circular sliding surface, c_i is cohesion force of block No i, φ_i is internal friction angle of block No i, W_i is weight of block No i and overlying tailings, L_i is bottom edge length of block No i, Q_i is horizontal force acting on block No i, α_i is angle between bottom edge of block No i and U_i is horizontal plane of coordinate axis on block No i:

$$X=\lambda f(x) E \qquad \text{Morgen-Prince equation} \qquad (2.4)$$

where X is tangential force between soil strips, E is normal force between soil strips, and λ is constant. Calculation results indicate that many calculations of the simplified Bishop method are accurate calculation and closer to the allowable safety factor than the Morgen-Prince method. The factors of safety decrease gradually with the increase of slope angle in Table 2.4. The influence of rainfall on slope stability of simplified Bishop and Morgen-Prince methods is that the factors of safety are reduced by 9.07~16.19% and 9.24~15.93%, respectively. The numerical analysis is simulated by FLAC3D analysis on A and B models (Figure 2.16). Simulation results for models A and B are shown in Figures 2.17 and 2.18, respectively. The minimum slope stability of models A and B are 1.51 and 1.43 which both are higher than the allowable slope stability of 1.25 and 1.25. Both models are in a stable state.

มหาวิทยาลัยเทคโนโลยีสุรนารี

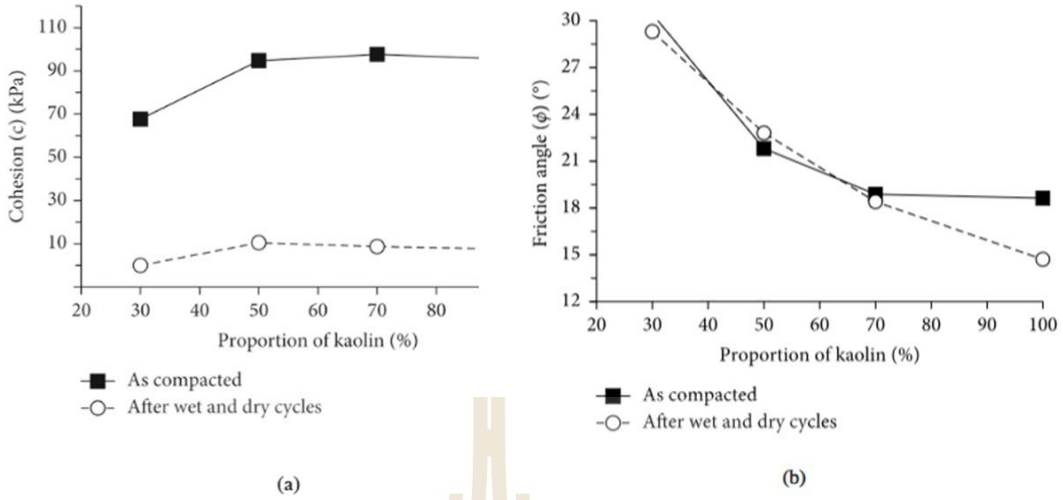


Figure 2.14 Comparison of shear strength parameters between the compacted and subjected to wetting-drying of kaolinite-quartz proportion: a) cohesion and b) friction angle (Charkley et al., 2019).

มหาวิทยาลัยเทคโนโลยีสุรนารี

Table 2.3 Mass mechnical parametoers (Su et al., 2022).

Weathering/Rock types	Density (g/cm^3)	Elastic Modulus E/(MPa)	Poisson Ratio μ	Cohesion C/(MPa)	Friction angle φ(Degree)
Strongly/ andesite porphyry	2.23	241.83	0.3	0.16	24
Moderately/ andesite porphyry	2.39	1561.44	0.3	0.25	32
Slightly/ andesite porphyry	2.58	3587.58	0.22	0.76	37
Strongly/ pyroclastic rock	2.15	284.52	0.29	0.17	25
Moderately/ volcanic clastic rock	2.26	1060.40	0.23	0.20	30
Slightly/ volcanic clastic rock	2.43	4062.90	0.29	0.67	36
Moderately/ biotite hornblende mountain porphyry	2.56	2953.59	0.25	0.60	34
Slightly/ biotite hornblende mountain porphyry	2.64	7884.14	0.22	1.10	39
Slightly/sandstone	2.59	4010.65	0.2	0.70	35
Quaternary soil	1.96	6	-	0.036	11.41
Waste rock of waste dump	1.91	750	0.29	0.035	32

มหาวิทยาลัยเทคโนโลยีสุรนารี

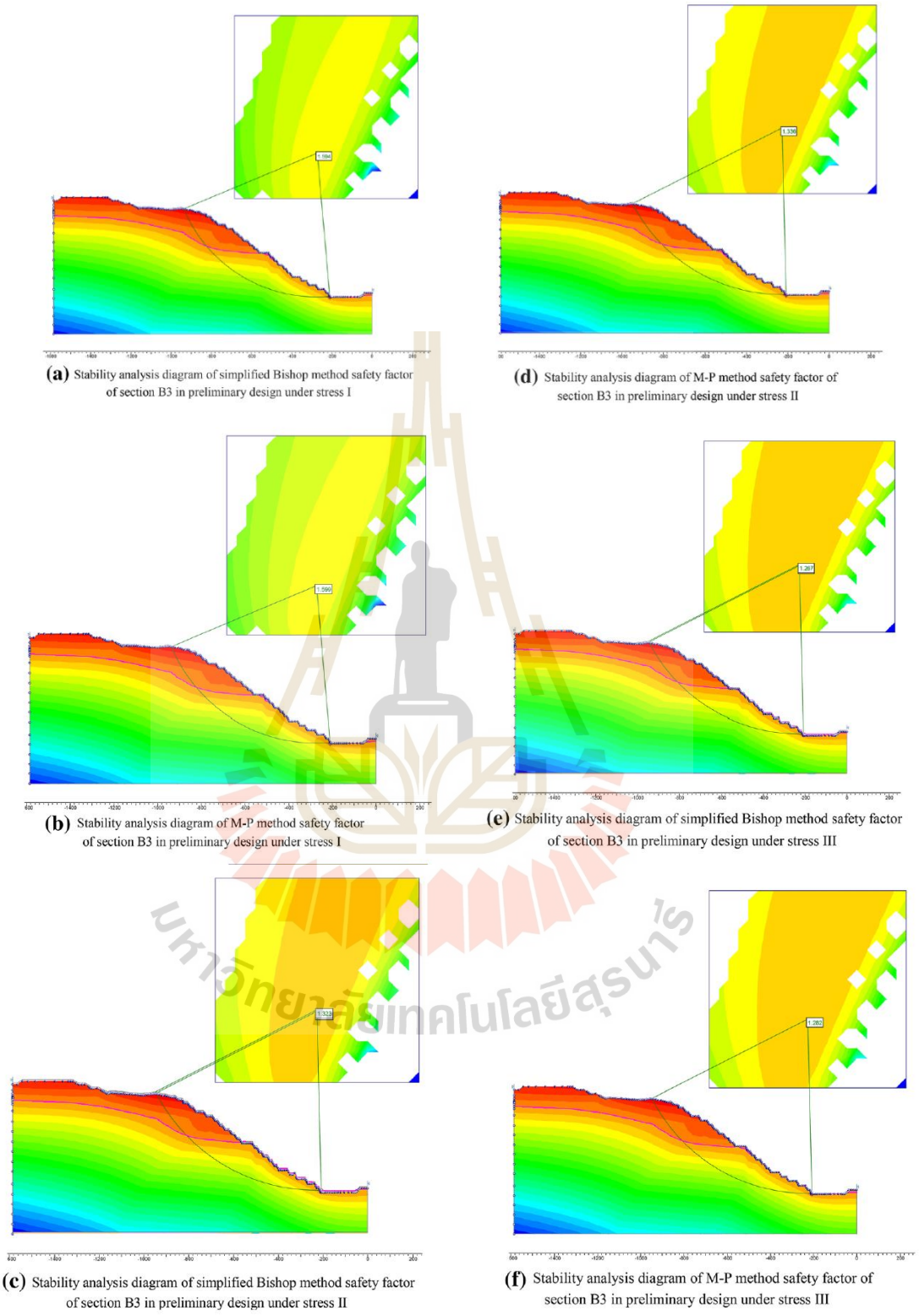


Figure 2.15 Examples of stability analysis of simplified Bishop and M-P method of each section and zone (Su et al., 2022).

Table 2.4 Designed safety of factor results (Su et al., 2022).

Sections	Overall slope angle (°)	Analysis method	Safety of factor			
			Condition I	Condition II	Condition II	Condition IV
A1	39.4	B	1.706	1.432	1.366	1.705
		M-P	1.707	1.439	1.378	1.706
A2	38.4	B	1.554	1.321	1.266	1.378
		M-P	1.557	1.330	1.272	1.382
B1	38.8	B	1.509	1.282	1.230	1.356
		M-P	1.507	1.289	1.235	1.357
B2	39.3	B	1.557	1.313	1.258	1.350
		M-P	1.567	1.331	1.278	1.363
C1	30.7	B	1.958	1.578	1.505	1.853
		M-P	1.957	1.583	1.510	1.854
C2	24.5	B	2.398	1.868	1.776	2.275
		M-P	2.399	1.876	1.783	2.276
D1	28.9	B	2.160	1.742	1.659	2.016
		M-P	2.160	1.749	1.666	2.016
D2	34.2	B	1.910	1.602	1.529	1.721
		M-P	1.906	1.610	1.538	1.722

มหาวิทยาลัยเทคโนโลยีสุรนารี

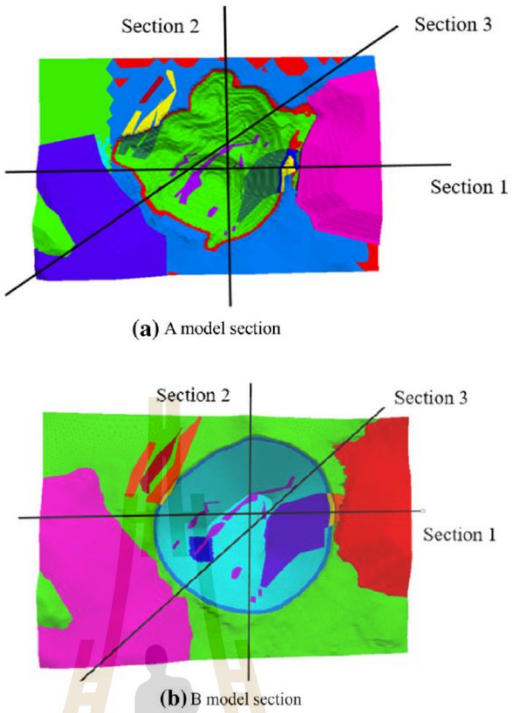


Figure 2.16 Location of A and B model sections (Su et al., 2022).

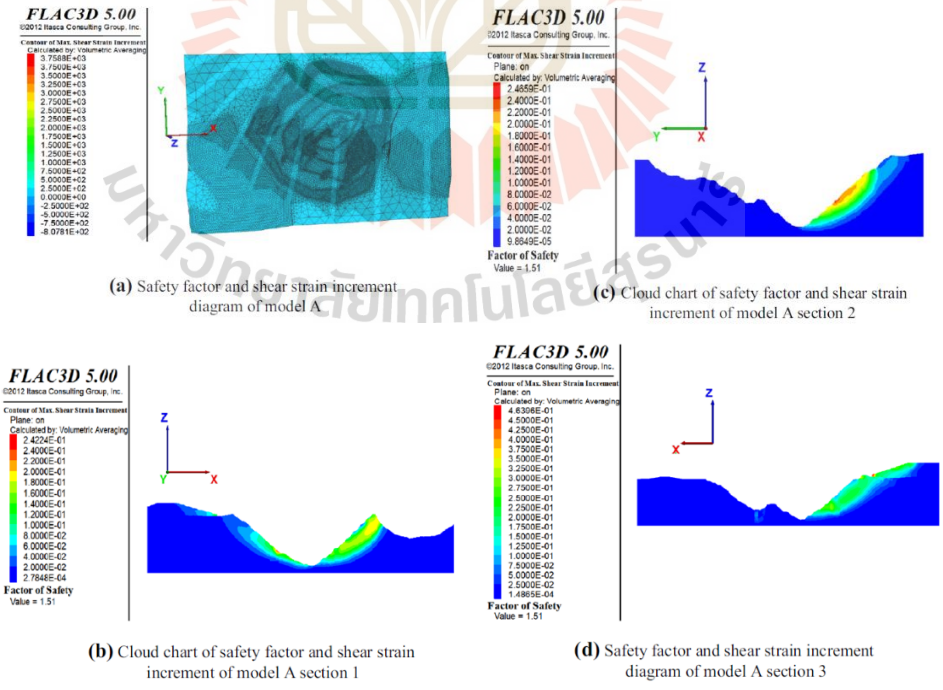
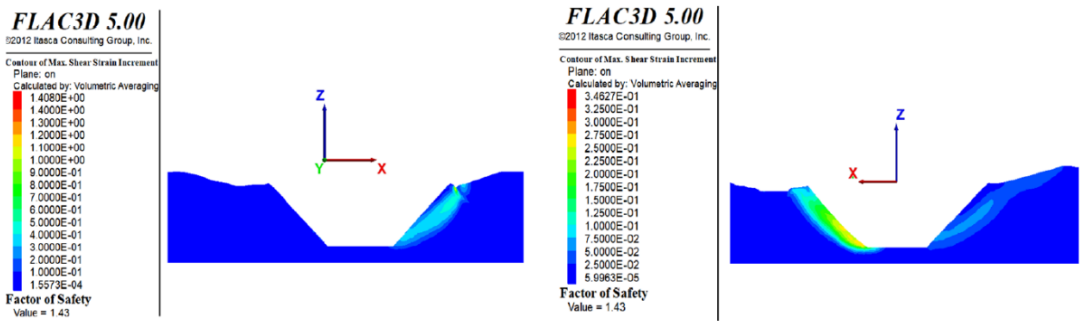


Figure 2.17 Cloud chart of safety factor and shear strain increment of model A (Su et al., 2022).



(b) Cloud chart of safety factor and shear strain increment of model B section 1

(d) Cloud chart of safety factor and shear strain increment of model B section 3

Figure 2.18 Cloud chart of safety factor and shear strain increment of model B (Su et al., 2022).

Beyabanaki (2020) studied a comparison between using finite difference and limit equilibrium methods for failure analysis for different weak layers of slopes with a 0.5 m thickness of the weak layer. The factor of safety analysis is performed using FLAC program version 8.0 and SLIDE version 9 with properties of materials in Table 2.4 and the case considered investigated in Figures 2.19 and 2.20. The results of different weak layer conditions are studied 4 conditions as 1) horizontal weak layer 5m above toe as shown in Figures 2.21 and 2.22) horizontal weak layer 1 m above toe in Figures 2.23 and 2.24) inclined weak layer with slope of 29° in Figures 2.25 and 2.26, and weak layer with steep slope of 57° in Figures 2.27 and 2.28. Both slope stability analysts show that the minimum factor of safety of finite difference method results is smaller than the limit equilibrium method for all cases. In horizontal weak layer conditions shows a smaller potential failure surface. The weak layer with a 57° slope condition predicts a smaller potential failure surface on limit equilibrium analysis. The summary of the results is in Table 2.6.

Table 2.5 Properties of rock and weak layer (Beyabanaki, 2020).

Material	Unit weight (kN/m)	Cohesion (kPa)	Friction angle (degrees)
Rock (Siltstone)	27	44	39.2
Weak layer	25	8	15.9

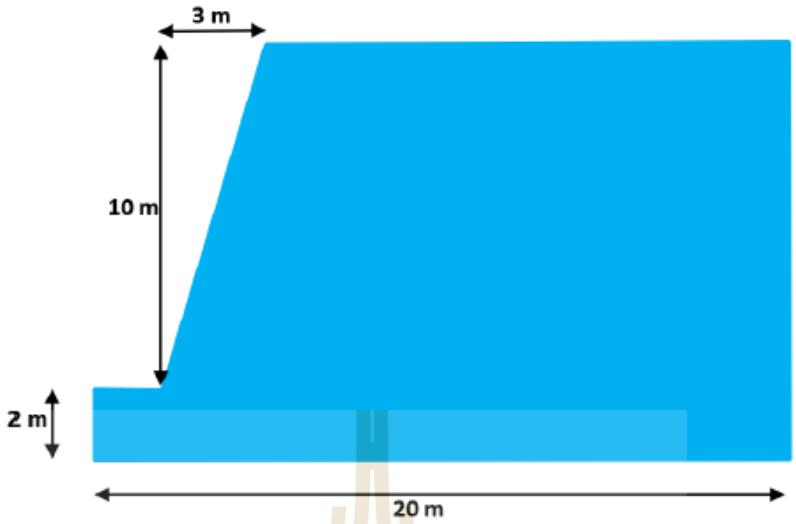


Figure 2.19 Dimension of the analyzed slope (Beyabanaki, 2020).

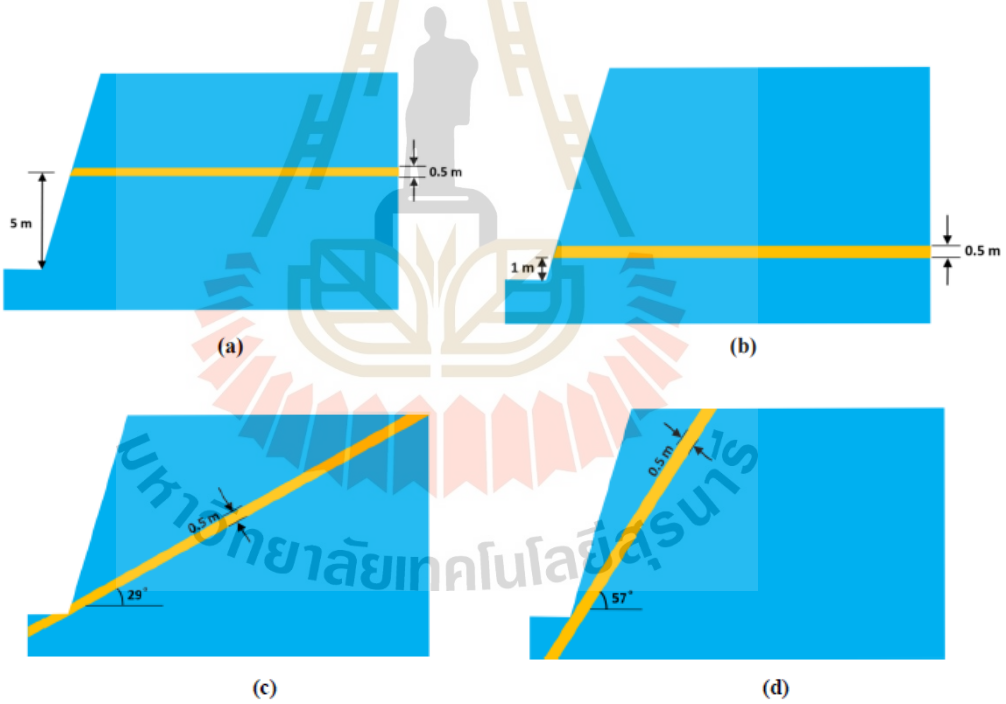


Figure 2.20 Case considered for weak layer: a) horizontal weak layer 5 m above toe, b) horizontal weak layer 1 m above toe, c) inclined weak layer with an angle of 29° with respect to horizontal, d) weak layer with an inclination of 57° (Beyabanaki, 2020).

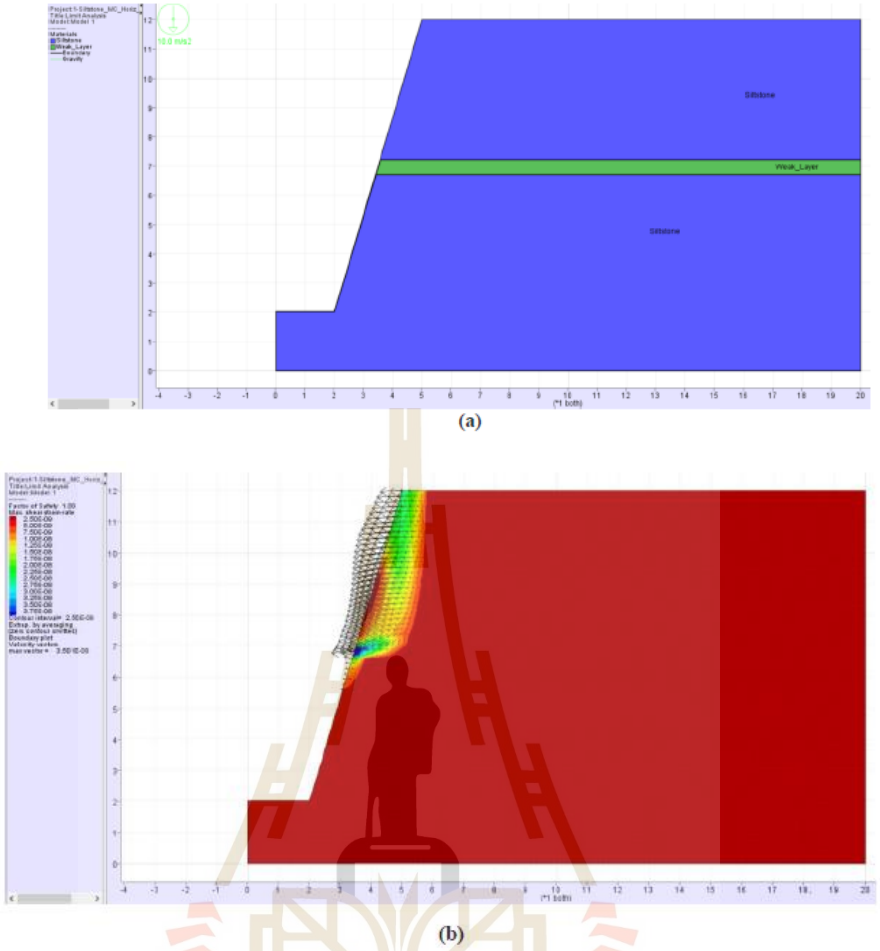


Figure 2.21 FLAC modelling for case 1: a) model configuration and b) modeling results (Beyabanaki, 2020).

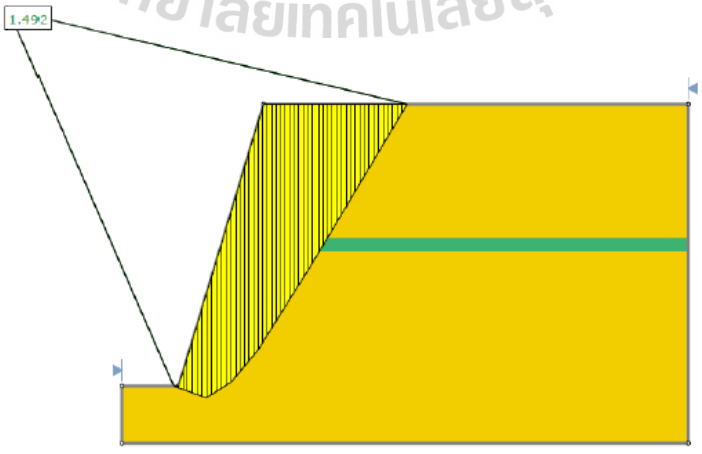


Figure 2.22 LEM analysis result for case 1 (Beyabanaki, 2020).

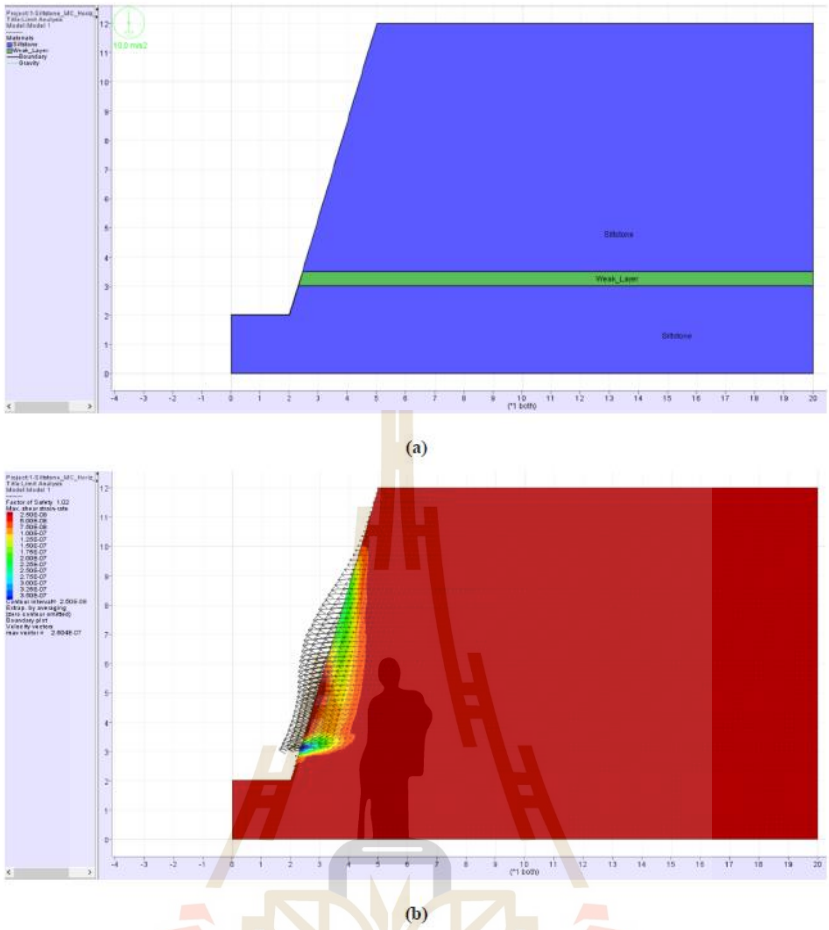


Figure 2.23 FLAC modelling for case 2: a) model configuration and b) modeling results (Beyabanaki, 2020).

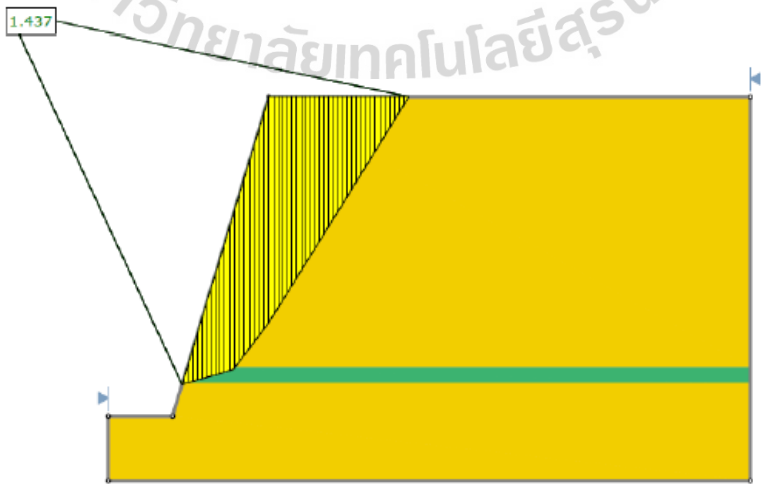


Figure 2.24 LEM analysis result for case 2 (Beyabanaki, 2020).

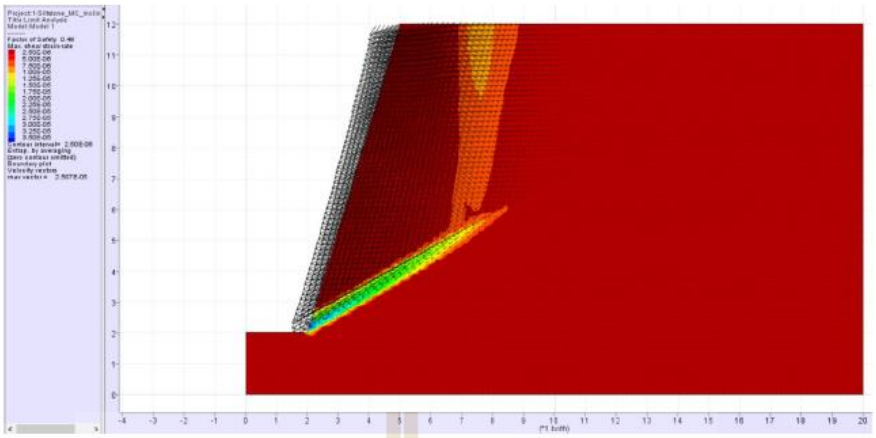


Figure 2.25 FLAC modelling for case 3: a) model configuration and b) modeling results (Beyabanaki, 2020).

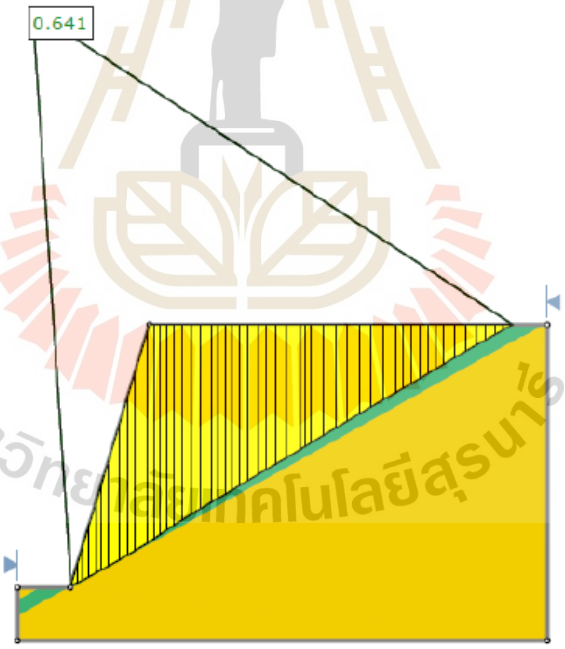


Figure 2.26 LEM analysis result for case 3 (Beyabanaki, 2020).

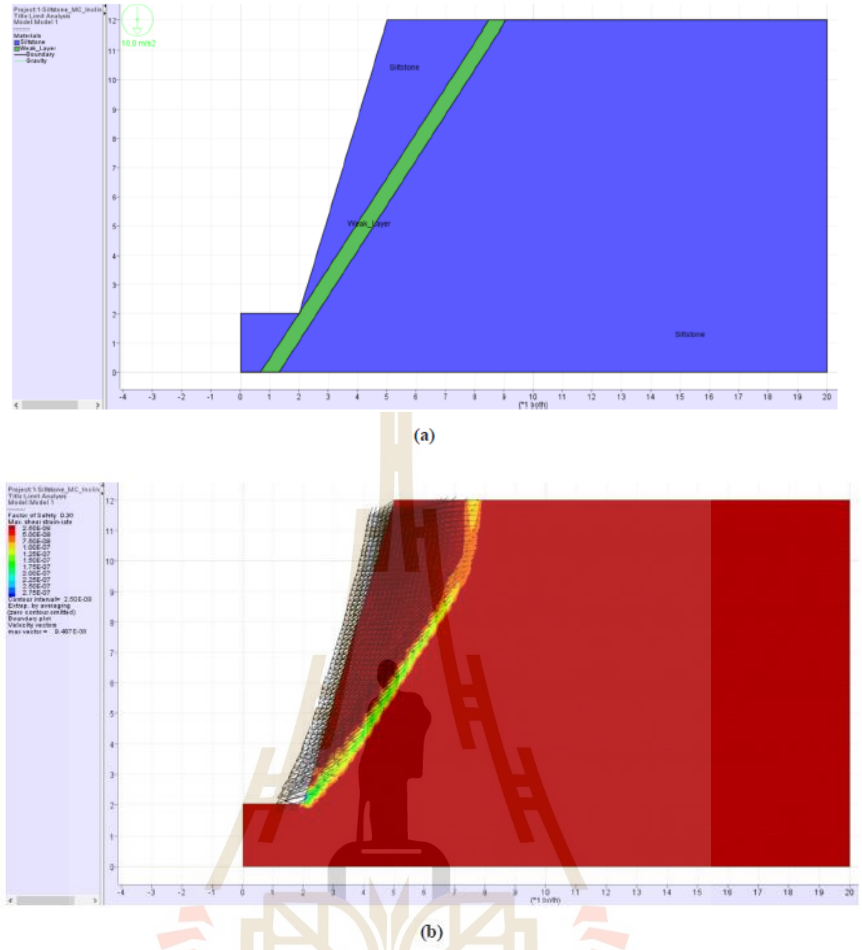


Figure 2.27 FLAC modelling for case 4: a) model configuration and b) modeling results (Beyabanaki, 2020).



Figure 2.28 LEM analysis result for case 4 (Beyabanaki, 2020).

Table 2.6 Summary of minimum of safety factor results by FDM and LEM analysis (Beyabanaki, 2020).

Case No.	Detail condition	Minimum of factor of safety result	
		FDM	LEM
1	Horizontal weak layer in the middle of slope	1.00	1.49
2	Horizontal weak layer close to slope base	1.02	1.44
3	Slope with 29°inclined weak layer	0.48	0.64
4	Slope with 57°inclined weak layer	0.36	0.39

มหาวิทยาลัยเทคโนโลยีสุรนารี

CHAPTER III

STUDY AREA

3.1 Introduction

The Phu Kham mine was assessed by Ramli and Lucas (2021), Mining One Consulting company extend cutback slope at south wall. This chapter describes the location of the Phu Kham mine, the failure of the south wall, lithology and structure control at the south wall, and stability analysis using Slide3 model software.

3.2 Location of Phu Kham Mine

PanAust Limited operates the Phu Kham open pit copper-gold mine, locates approximately 110 kilometers north of Vientiane in Laos. The site location is shown in Figure 3.1.



Figure 3.1 Location of Phu Kham mine, Laos (Ramli and Lucas, 2021).

3.3 Failure of South Wall

In 2018, the inspection of south wall slope conditions by observation of the site found the occurring failures, as shown in Figure 3.2. The upper south wall slope (above 500 mRL) has experienced batter failure in black fault and tuff related to a combination of weak material and redbed structures sub-parallel for the wall (Figure 3.3). The lower slope (below 500 mRL) is developed in the weak rock mass composed of altered tuff and black fault which have slaked to soil material (Figure 3.4).

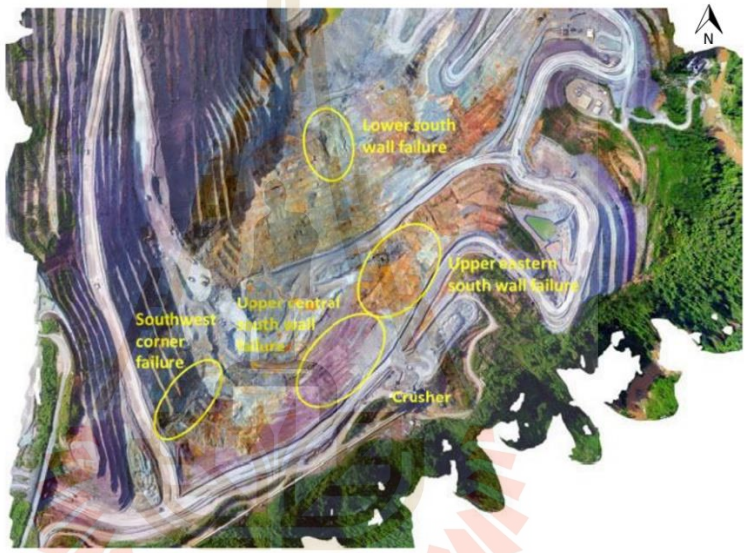


Figure 3.2 Location of failure on south wall at Phu Kham mine (Ramli and Lucas, 2021).



Figure 3.3 Upper part of south wall at Phu Kham mine (Ramli and Lucas, 2021).

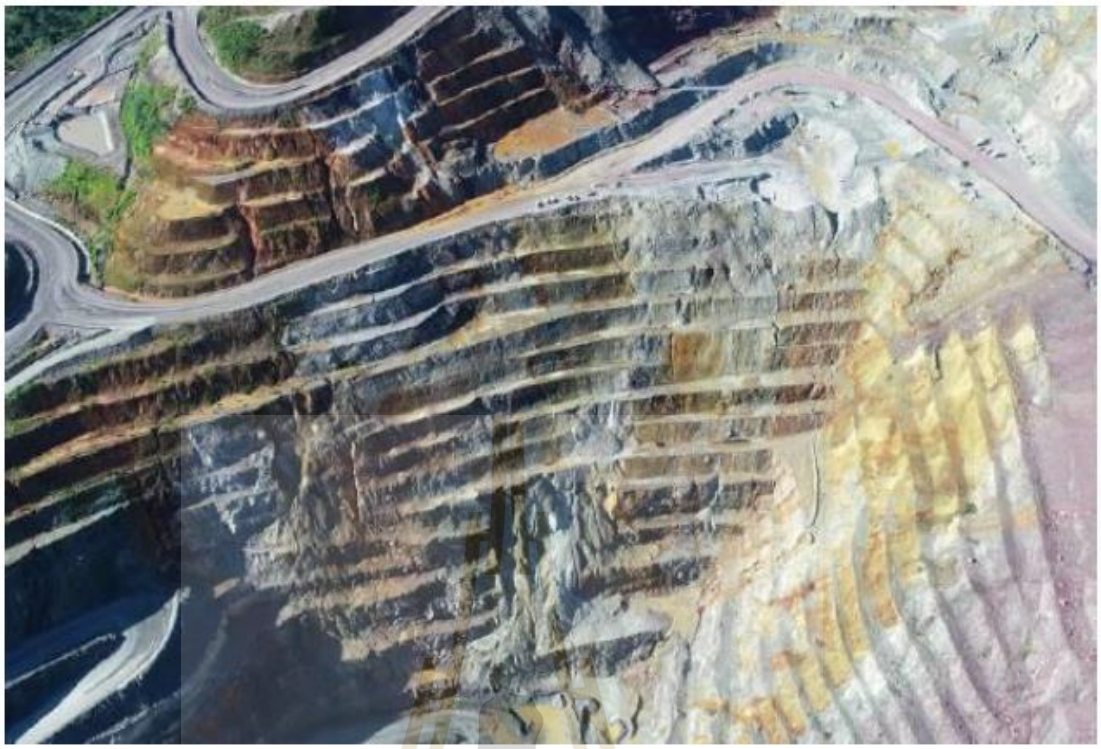


Figure 3.4 Lower part of south wall at Phu Kham mine (Ramli and Lucas, 2021).

3.4 Lithology and structure control at south wall

Many researchers were studied the lithologies and structures of the Phu Kham mine deposit. The Ramli and Lucas (2021) compiled and studied the whole data of the south wall Phu Kham mine to understand the structurally and geologically complex region.

3.4.1 Lithologies and weathering boundaries at south wall

Figure 3.5 shows the major lithology that are be exposed on the 2022 pit design. The lithologies code, strengths, and direct shear test results per lithology are presented in Table 3.1. The tests included unconfined compressive strength (UCS), triaxial compressive strength (TXL) and direct shear (DS) tests results.

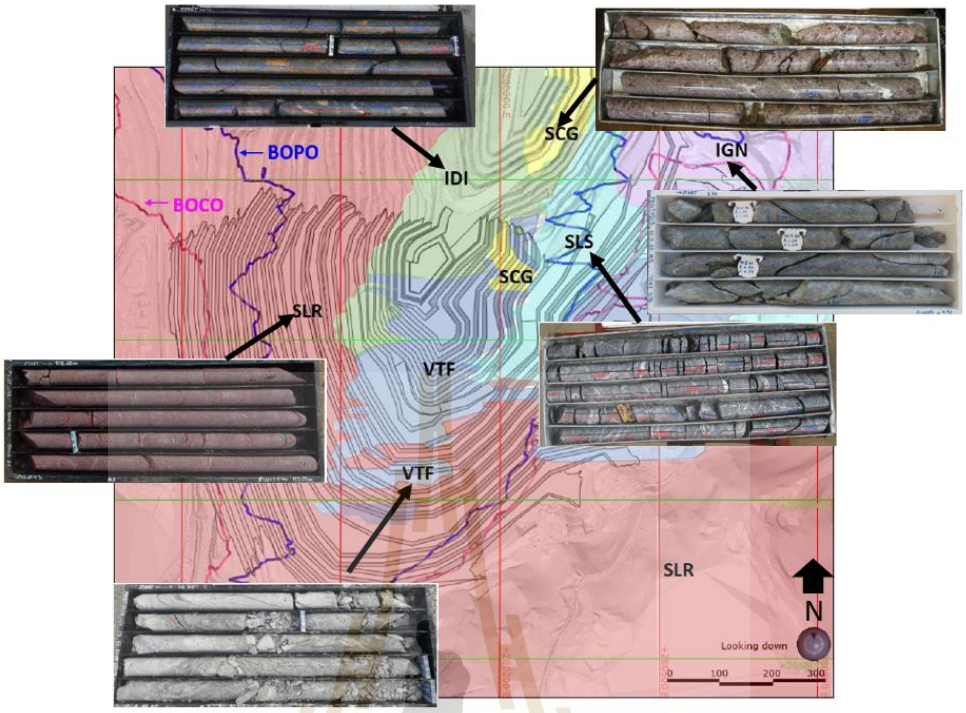


Figure 3.5 Lithologies and weathering boundary of the south wall at Phu Kham mine.

Table 3.1 Summary of laboratory test results per lithology (Ramli and Lucas, 2021).

Code	Lithology	UCS (MPa)	TXL (MPa)	DS (MPa)
VTF	Tuff	61	42	39
SLS	Limestone	89	73	79
IDI	Diorite	89	52	31
SLR	Red siltstone	145	90	118
IGN	Granite	44	30	29
SCG	Conglomerate	57	46	28
-	Fault	-	-	15

3.4.2 Structure control at south wall

The Ramli and Lucas (2021) has classified by combination of lithology, weathering, rock mass quality and structures in the domain by using Leapfrog software as shown in Figure 3.6. The Figures 3.7 and 3.8 describe geological faults at the south wall. There is the overview plan with cross-section line (Figure 3.9) and detail of cross-section (Figure 3.10) against the 2022 pit design with the current topography in February 2021. The fault of locations and their cross-cutting relationship are based on pit mapping, aerial photography, and drilling data. The cross-section slices developed between "Black Fault" in the west and the "Black Fault 16" in the east (Figures 3.9 and 3.10). The Black Fault 16 appears to be the youngest major structure as it offsets the South Thrust – East Faults in a lateral sense. Figure 3.11 shows core drilling photo of Black Fault 16 material from diamond drilling data. The key to stability controls have defined from the lithologies, major structures and rock mass direction in Figure 3.12.

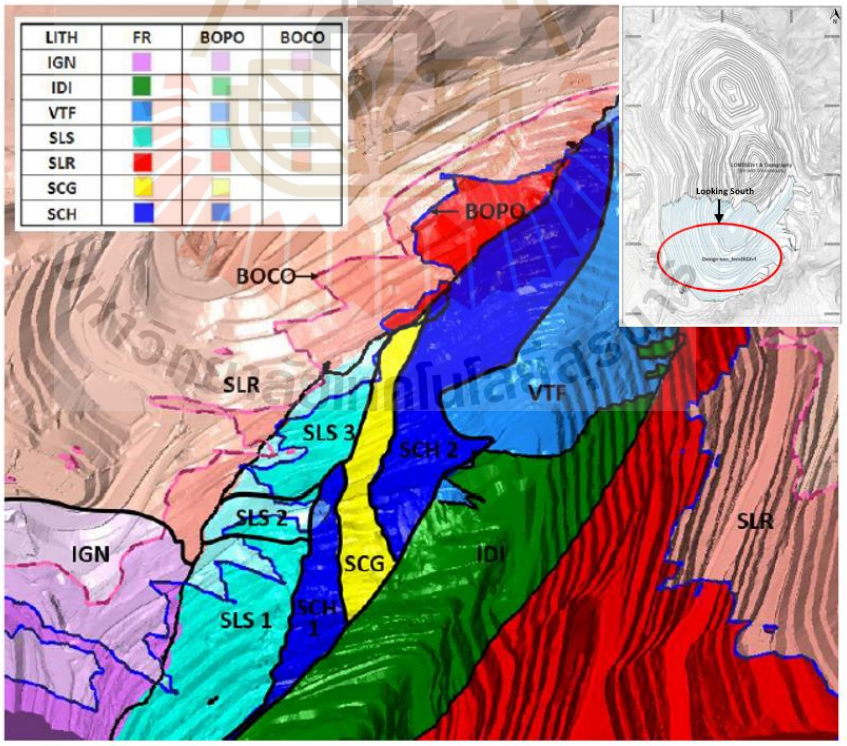


Figure 3.6 Lithologies of the south wall at Phu Kham mine (Ramli and Lucas, 2021).

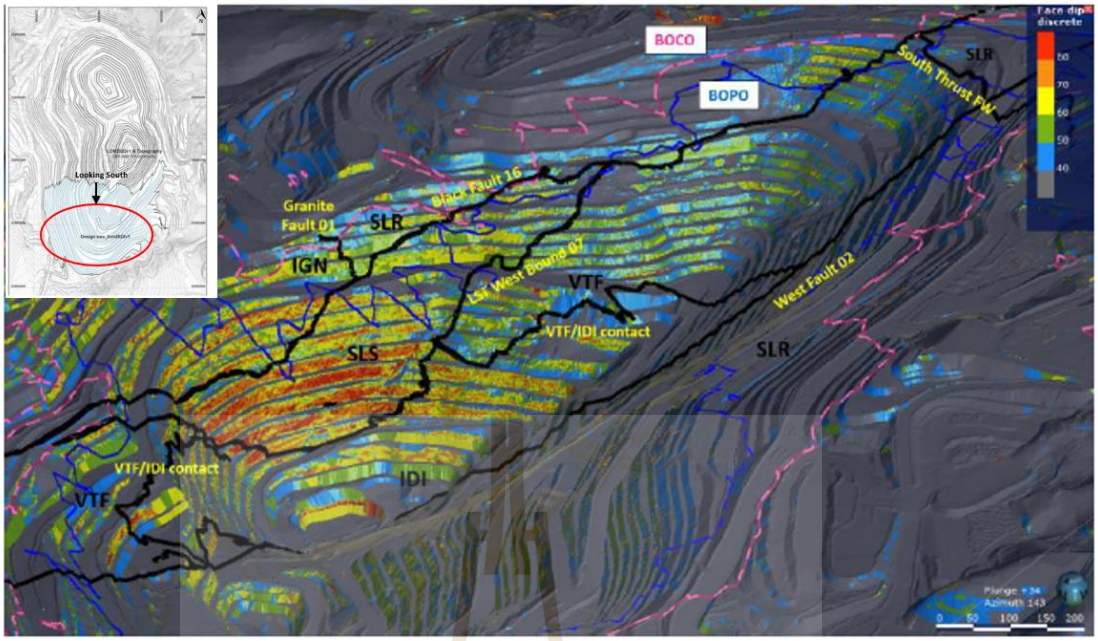


Figure 3.7 Geological faults and lithologies for south wall at Phu Kham mine (Ramli and Lucas, 2021).

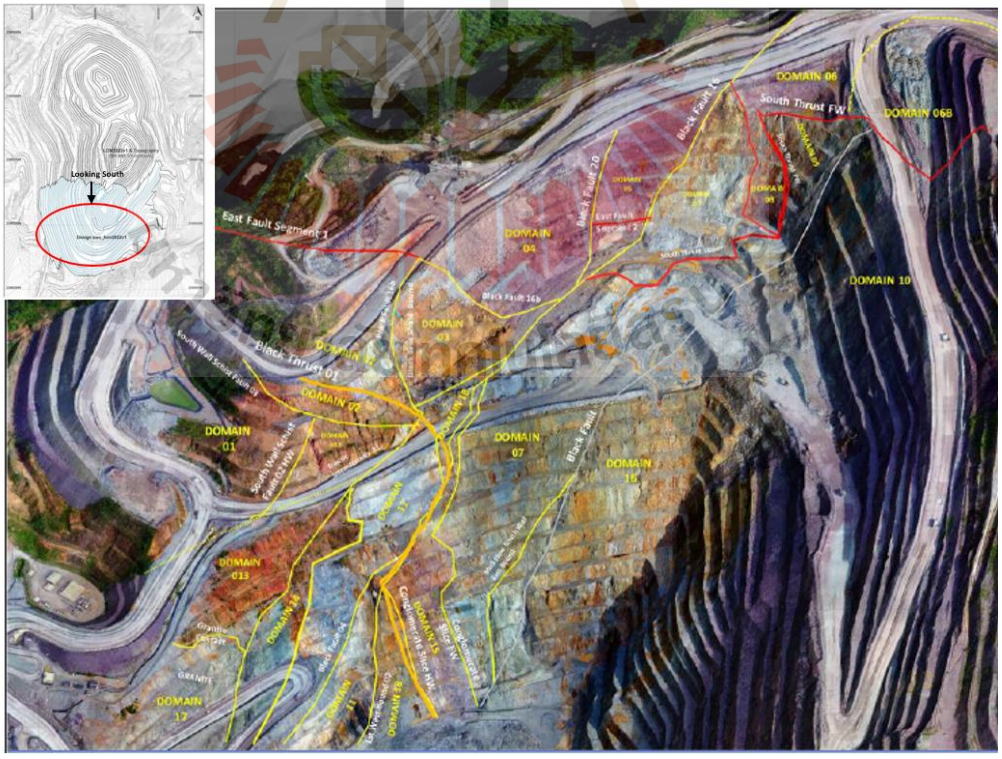


Figure 3.8 Geological faults at south wall at Phu Kham mine (Ramli and Lucas, 2021).

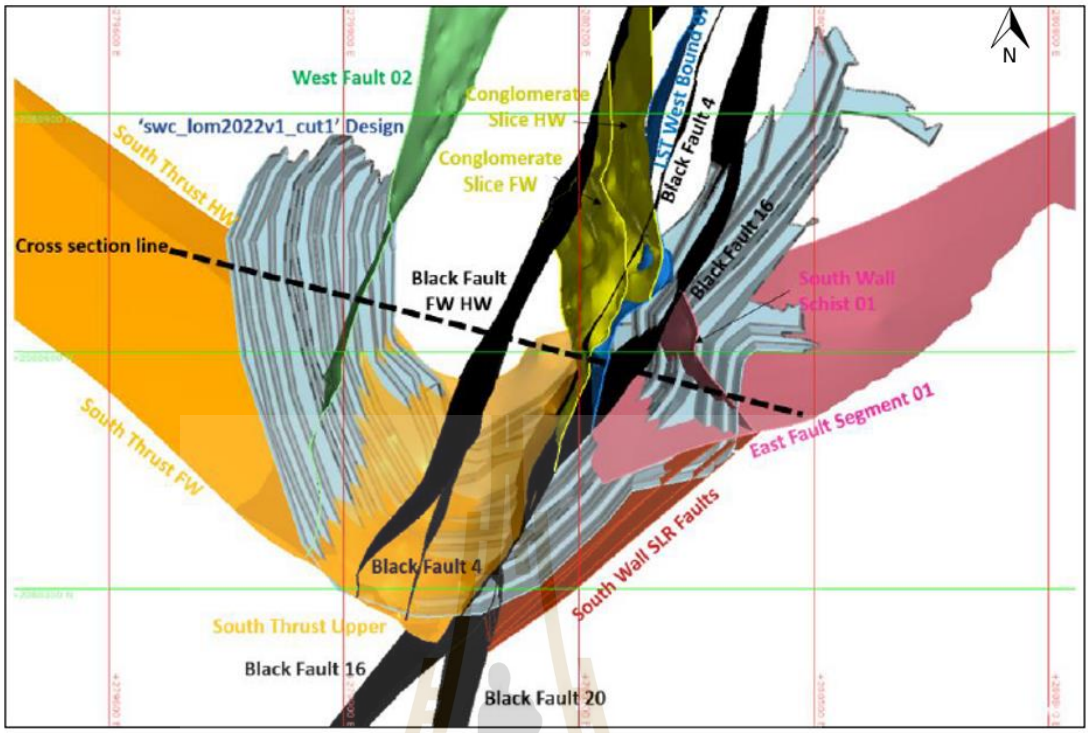


Figure 3.9 Plan of south wall fault network, ±100m slice at 450mRL level plan at Phu Kham mine (Ramli and Lucas, 2021).

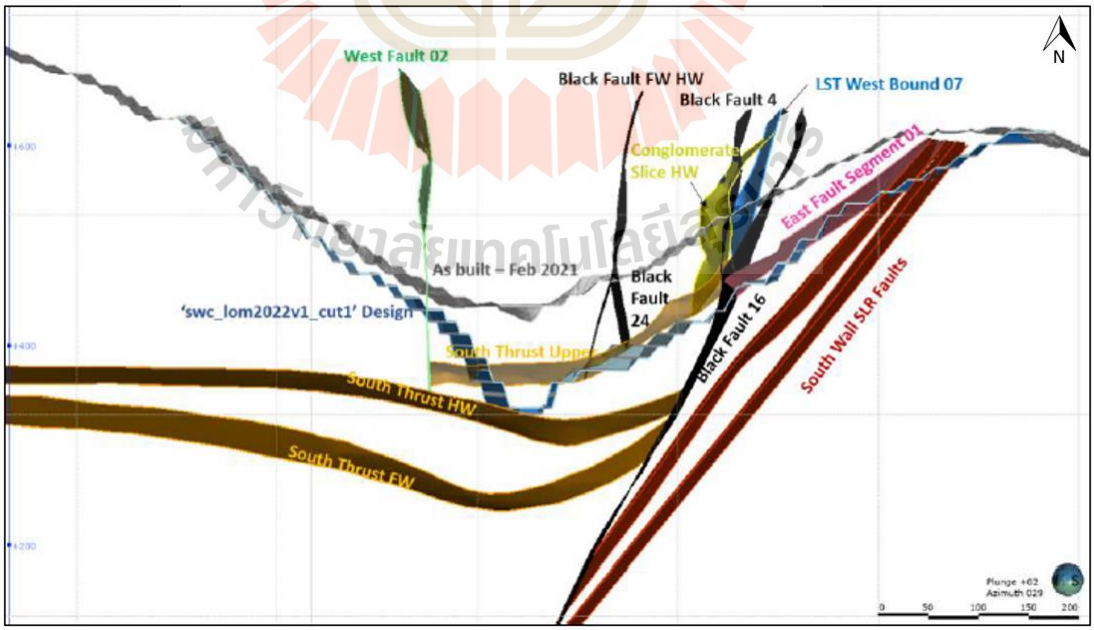


Figure 3.10 South wall cross section, looking north at Phu Kham mine (Ramli and Lucas, 2021).



Figure 3.11 Black fault 16, faulted contact between VTF and IGN with clay alteration at the south wall, Phu Kham mine (Ramli and Lucas, 2021).

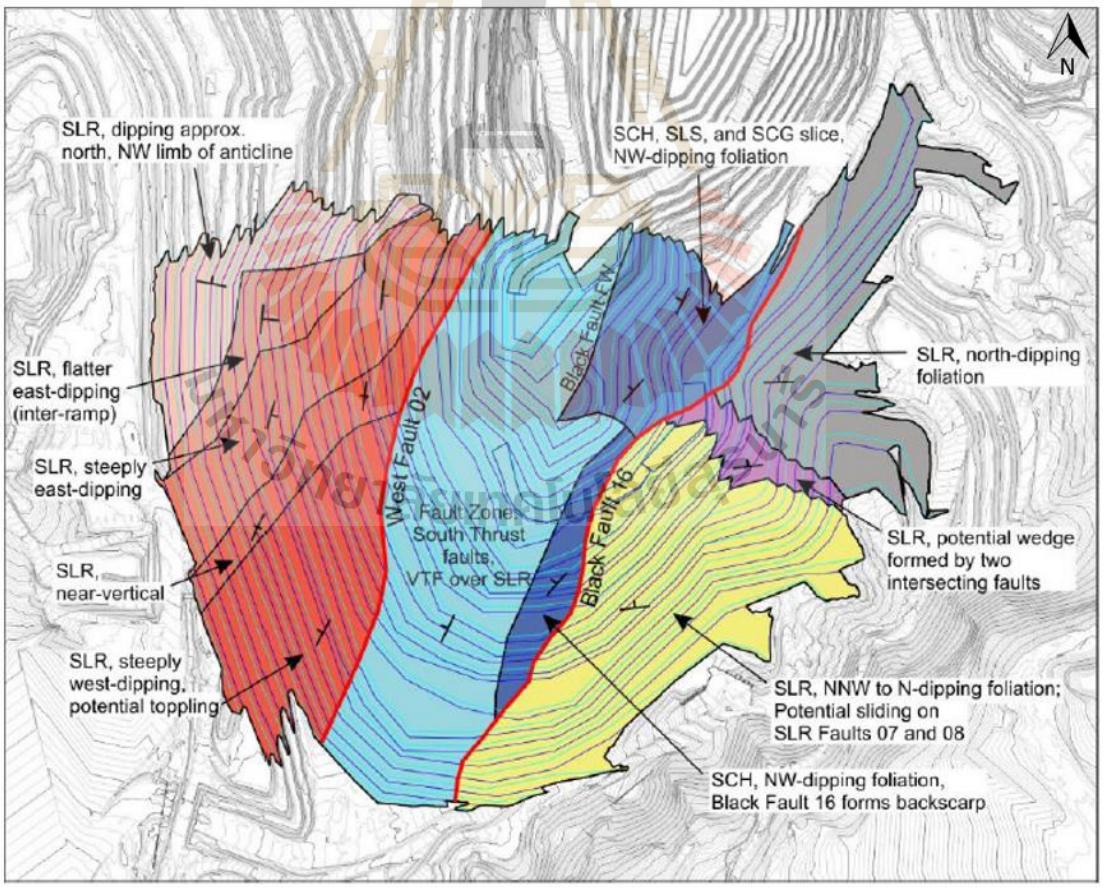


Figure 3.12 Key potential failure mechanism at the south wall, Phu Kham mine (Ramli and Lucas, 2021).

3.5 Stability analysis at south wall

An initial slope stability analysis was conducted using Rocscience Slide 3D software by Ramli and Lucas (2021). The Slide3D have been simplified with rock mass parameters in Table 3.2 and critical faults at the south wall, Phu kham mine. The critical faults were selected from the most likely to drive instability slope on Slide 3D software in Figure 3.13. Stability analysis in the southern slopes shows the slope stability is controlled by the orientation of the SLR bedding. There are also critical fault interactions that contribute to the slope stability as there are several north-dipping faults intersect the southern slopes. The Slide 3D was applied as follows:

Weathering domain boundaries (BOCO and BOPO) have provided for the weathered, transition and fresh material

Lithological domain boundaries have been assessed based on geological surface,

Faults have been explicitly modelled with blocks of rock mass modelled using the generalized Hoek-Brown strength model. The SLR domain has been modelled using generalized anisotropic strength model,

The generalized limit equilibrium method of analysis was used along with the noncircular Cuckkoo search method,

The model utilizes a Hoek-Brown disturbance factor, D value of 0.7 throughout,

Ellipsoid surface shapes with composite surface have been used for model.

The Slide 3D model includes the critical faults model from King (2015) which are most likely to impact slope stability. The faults include as:

Black fault16,

South Thrust,

South Thrust Upper,

SLR fault 07 FW and HW,

SLR fault 08 FW and HW,

LST west bound 07,

West fault 02,

Conglomerate roof 02,

Lst west bound 07,

East fault segment 01,

South wall schist 01.

The groundwater has been presented as pore pressure from observation of drain holes. There are two cases for the wet season: a case with horizontal drain holes, and a case without drain holes in which only passive depressurization is allowed to occur, as a sensitivity case.

The results of slope stability analysis show that the failure occurs predominantly along the faulted planes, mainly the South Thrust Upper and South Thrust FW. The stability analysis results for the south wall are adequate factor of safety (FOS) values for base case, fault sensitivity case and no depressors drain hole. The base case fault strength with groundwater and drain holes yielded a FOS of 1.30 (Figure 3.14). The fault sensitivity case yielded a FOS of 1.24 for a larger inter-ramp instability in Figure 3.15. The FOS of ground water sensitive case with base case fault strength is 1.39 for no depressors drain hole, as shown in Figure 3.16.

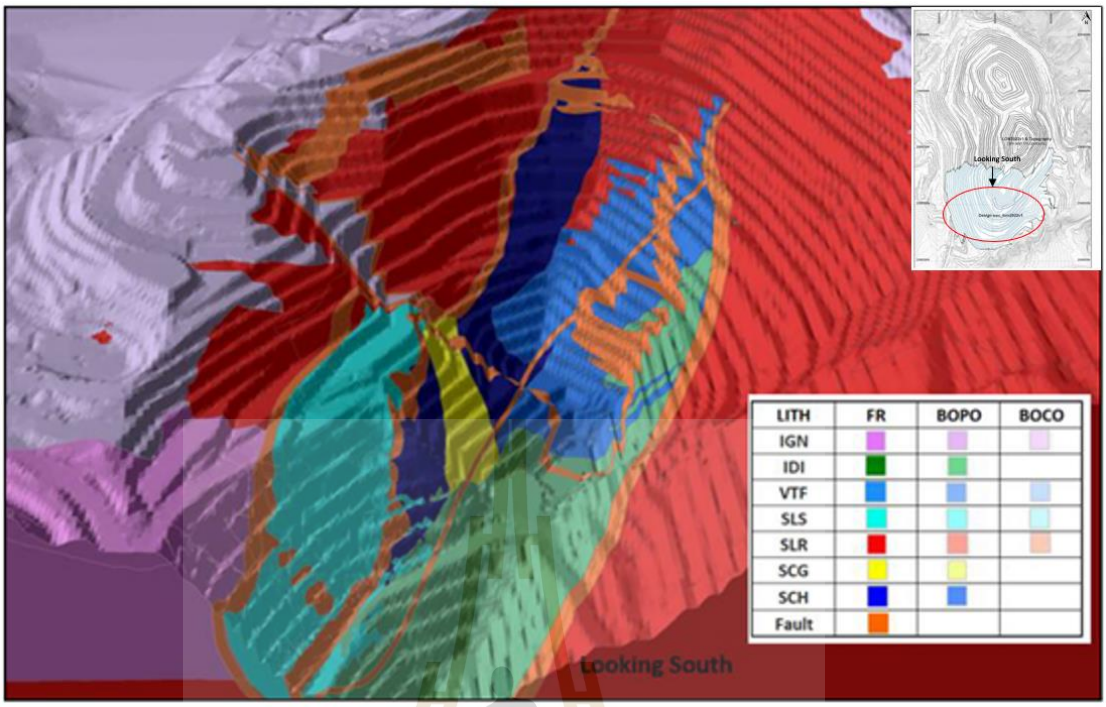


Figure 3.13 Slide3D model at south wall, looking south (Ramli and Lucas, 2021).

มหาวิทยาลัยเทคโนโลยีสุรนารี

Table 3.2 Rock mass shear strength parameters used for analysis (Ramli and Lucas, 2021).

Material	Unite weight (kN/m^3)	GSI (35^{th} percen-tile)	Young's Modulus (Median)	Rock		Foliation		Aniso-tropic Factor
				σ_o (MPa)	mi	σ_o (MPa)	mi	
SLR (Fresh)	26	66	23	30	15	15	8	2
SLR (Transition)	26	52	23	17	15	6	8	2
VTF	27	59	31	50	16	20	8	2.5
SCH1	27	56	31	50	16	20	8	2.5
SCH2	27	39	31	50	16	20	8	2.5
IDI	27	62	26	40	25	20	13	2
SCG	26	45	35	60	19	-	-	-
SLS1 (Fresh)	26	64	28	40	19	20	9	2
SLS2	26	46	28	20	19	5	9	2
SLS3 (Fresh)	26	62	28	40	19	20	9	2
SLS3 (Transition)	26	46	28	20	19	5	9	2
IGN (Fresh)	26	52	7	35	32	25	16	2.5
IGN (Transition)	26	30	7	35	32	25	16	2.5

มหาวิทยาลัยเทคโนโลยีสุรนารี

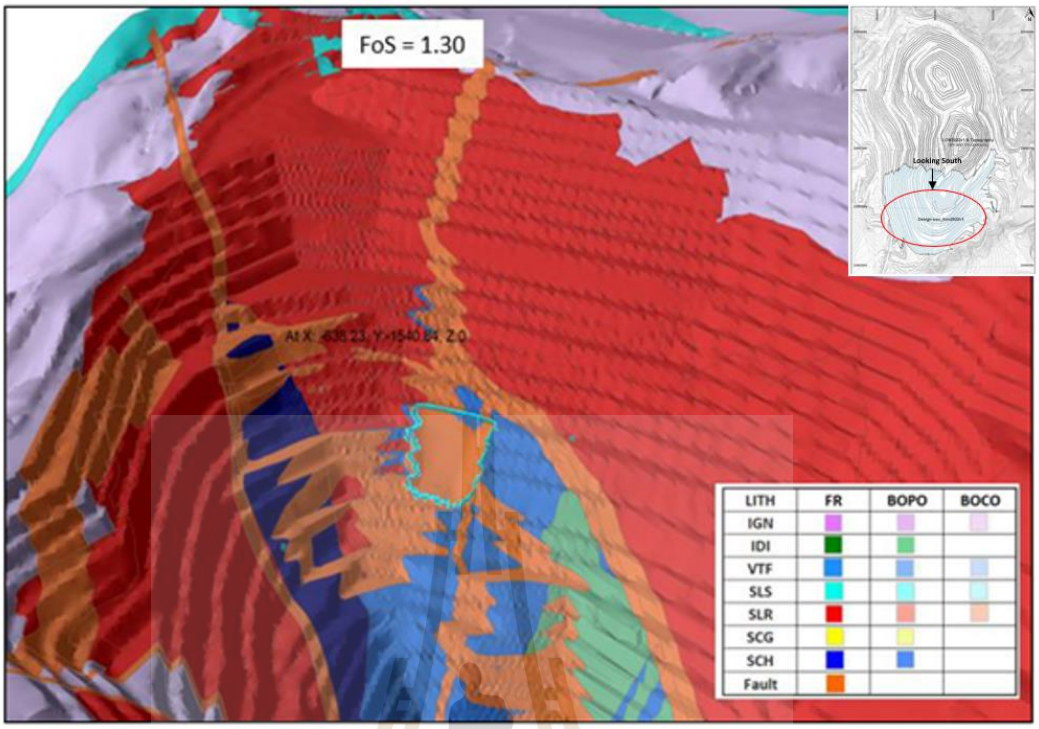


Figure 3.14 FoS for south wall, base case fault strength (Ramli and Lucas, 2021).

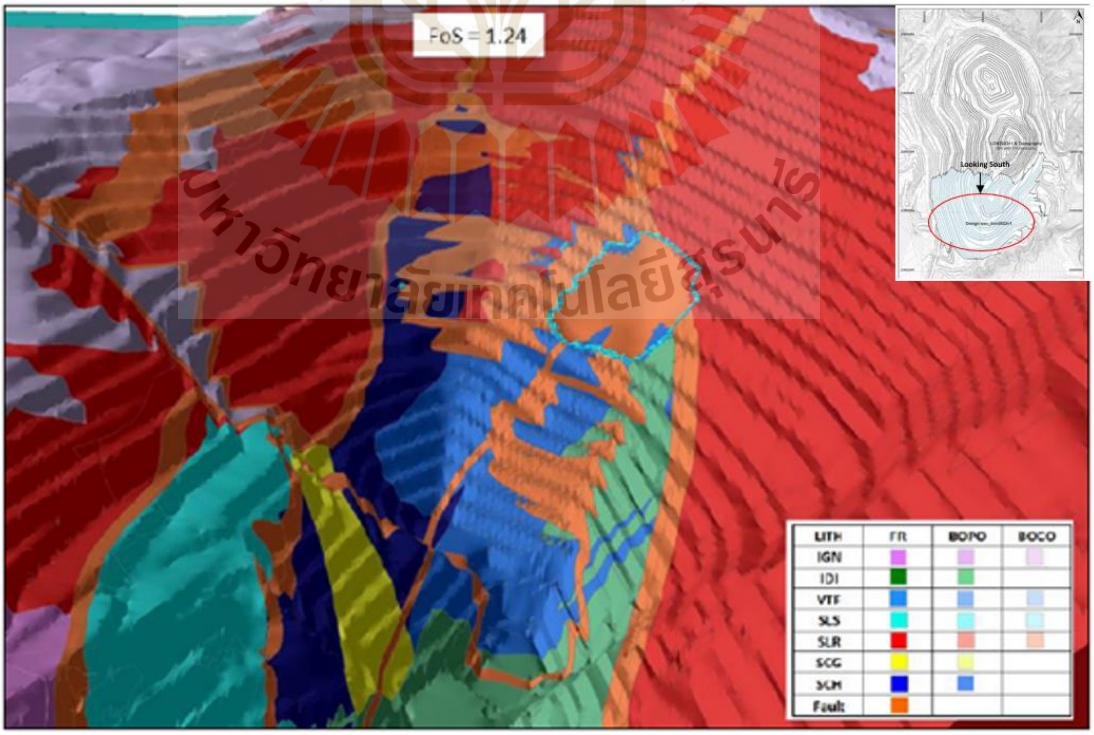


Figure 3.15 FoS for south wall, fault strength sensitivity case (Ramli and Lucas, 2021).

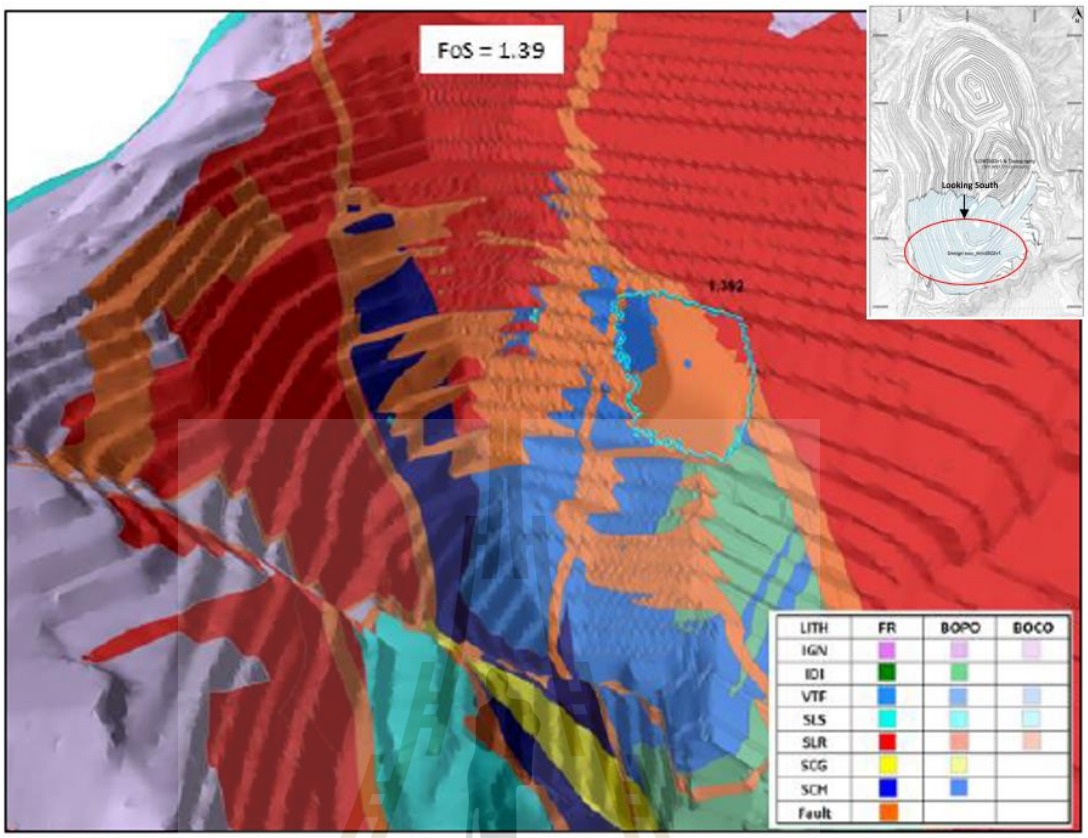


Figure 3.16 FoS for south wall, groundwater sensitivity case (Ramli and Lucas, 2021).

มหาวิทยาลัยเทคโนโลยีสุรนารี

CHAPTER IV
SAMPLE COLLECTION AND PREPARATION

4.1 Introduction

The mudflow material is selected as a test sample for this study. The material is divided into two types: black fault (BSH) and volcanic tuff (VTF). These samples are obtained from the Phu Kham mine. They also have a significant influence on stability of south wall of the open pit mine. This chapter describes sample collection, physical and chemical properties tests. Physical property tests provide water content, specific gravity, sand cone test, grain size analysis, and Atterberge's limit test. Chemical property tests involve XRF and XRD analysis.

4.2 Sample collection

Figure 4.1 gives material names, and depth from which they have been collected at borehole PKGT0093, pad construction at 519mRL. BSH sample was collected from depth ranging from 1.4 to 2.8 m and VTF was collected from depth ranging from 7.4 to 8.7 m of depth of drilling. For each sample, a minimum of 10 kg had been collected for the direct shear tests with varied water contents, and for the physical and chemical properties tests. The weak materials have been observed on the south wall at 390 to 570 mRL of bench elevation of Phu Kham open pit mine (Figure 3.1). Weak materials including BSH and VTF are weakened during the rainy season. They are collected for soil identification and classification following the ASTM D2487 and ASTM D2488 standards.

4.3 Physical property test

4.3.1 Natural water content

Natural water content is the quantity of water in the mass of soil in the field. It is determined by using the ASTM A2216 standard. The natural water content of the soil is evaluated by:

$$w, \% = [(W_s - W_d)/ W_d] \times 100 \quad (4.1)$$

where w is percentage of water content, W_s is mass of soil at the field and W_d is mass of dry soil in an oven for 12 to 16 hours at 110 °C ± 5 °C. The natural water content results of BSH and VTF are shown in Table 4.1.



Figure 4.1 Collection of drilling samples at PKGT0093.

4.3.2 Specific gravity

Specific gravity (G_s) of soil is the ratio of the density of soil with a density of water at stage temperature by using a pycnometer. The specific gravity test is performed following the ASTM D854 standard. The specific gravity of soil is the density of soil (γ_s) division by the density of water (γ_w) at the same volume. it is determined from the ratio of the mass per volume of soil at a stated temperature to the mass per volume of tilled water at a stated temperature. The 25 grams of dried soil is investigated by thoroughly crushing and putting in a pycnometer. The pycnometer is poured by the distilled water until the top water level, which is below the graduation mark in the pycnometer. The pycnometer is wormed up to boil for reducing of influence of entrapped air in the pycnometer. The added water instead entrapped air till the below graduation mark. The temperature is recorded, and the bottle is weighed. The specific gravity of soil is determined using the relations:

$$\gamma_s = [(W_3 - W_1) \times \rho_w] / [(W_2 - W_1) - (W_4 - W_3)] \quad (4.2)$$

$$G_s = \gamma_s / \gamma_w \quad (4.3)$$

where γ_s is density of soil, γ_w is density of water at stated temperature, W_1 is weight of an empty pycnometer, W_2 is weight of the pycnometer filled with distilled water up to the graduation mark, W_3 is weight of the pycnometer filled with soil material, W_4 is weight of pycnometer filled with soil material and distill water after entrapped air is removed. The specific gravity results of BSH and VTF are given in Table 4.1.

4.3.3 Sand cone test

Sand cone tests were performed on 15th June 2021 to determine the density of the field using a sand pouring cylinder. The test method is relevant to ASTM D1556 standard at south wall, Phu Kham mine in Figure 4.2. The field density of the sand cone test of BSH and VTF samples are defined (Figures 4.3 and 4.4). The test is determined from the different mass of volume of sand in a sand pouring cylinder instead of the excavated soil, calculating of hole volume is calculated from the excavated soil. The field density of soil is determined by dividing the mass of the

volume of in-situ soil which is calculated by the sand density (γ_c) value. The sand density is 15.65 kN per cubic meter from the calibration of the Phu Kham laboratory. The field densities of this research are wet density, the mass of excavated soil in the field, and dry density, the mass of drying of excavated soil which is dried by oven machine till out of water content in the sample. The mass of drying of excavated soil is calculated to find dry density. The mass of excavated soil at the field is wet density. The field density of soil is determined using the relations:

$$V=(W_1-W_2) / \gamma_c \quad (4.4)$$

$$\gamma_m=W_3 / V \quad (4.5)$$

$$\gamma_d= W_4 / V \quad (4.6)$$

where W_1 is weight of sand pouring cylinder filled with sand up to full of cylinder, W_2 is weight of the remaining sand in the cylinder after the test, W_3 is the weight of excavated soil, W_4 is the weight of drying excavated soil, V is volume of the hole, γ_m is wet density at the field, γ_d is dry density at the field, γ_c is density of sand which was calibrated at Phu Kham mine laboratory. Field density results of BSH and VTF are given in Table 4.1.

4.3.4. Grain size analysis

The classification of grain size follows the ASTM D422 standard. The main particle sizes are gravel, sand, and fine size grain. The sand size grain is passing material sieve no.4 and retained material sieve no.200 which is particle sizes of 4.74-0.075mm. The fine grain is classified with particle sizes smaller than 0.075 mm (passing sieve no.200). The retained material sieve no.4 is larger than 4.75 mm of particle sizes which is gravel size. The sieve properties of ASTM standard is given in Table 4.2. The passing of sieve analysis of BSH and VTF are shown in Figures 4.5 and 4.6. The results of distributed particle sizes of BSH and VTF are given in Table 4.1.

4.3.5. Atterberge's limit test

Atterberge's limit test classified the behavior of fine grain in relation to water content. The parameters of tests include the plastic limit (PL), liquid limit (LL), and plasticity index (PI) parameters. The test method is performed following the ASTM D4318 standard. The sample preparation is performed to pass the sample on sieve no.40. The liquid limit is determined percentage of water content by the groove closing a length of 13 mm (1/2 inches) along the bottom of the grove after 25 blows. The plastic limit is the water content percentage by stretched material with rolling into 3.2 mm (1/8 inches). The plasticity index is determined by the difference between the liquid limit and the plastic limit. The plastic limit, liquid limit, and plasticity index values of BSH and VTF are given in Table 4.1.

Table 4.1 Summary of physical properties test results of BSH and VTF.

Physical properties		BSH	VTF
Water content, w (%)		6.01	11.71
Specific Gravity, G_s		2.95	2.93
Sand Cone Test	Dry density, γ_d (kN/m^3)	13.30	15.00
	Wet density, γ_m (kN/m^3)	14.81	16.09
Sieve Analysis	Gravel (%)	25.4	12.1
	Sand (%)	20.2	55.4
	Fines (%)	54.4	32.4
Atterberg's limit	Liquid limit, LL (%)	28.4	-
	Plastic limit, PL (%)	14.7	-
	Plastic index, PI (%)	13.7	-
	Class <0.425mm	CL	-

มหาวิทยาลัยเทคโนโลยีสุรนารี

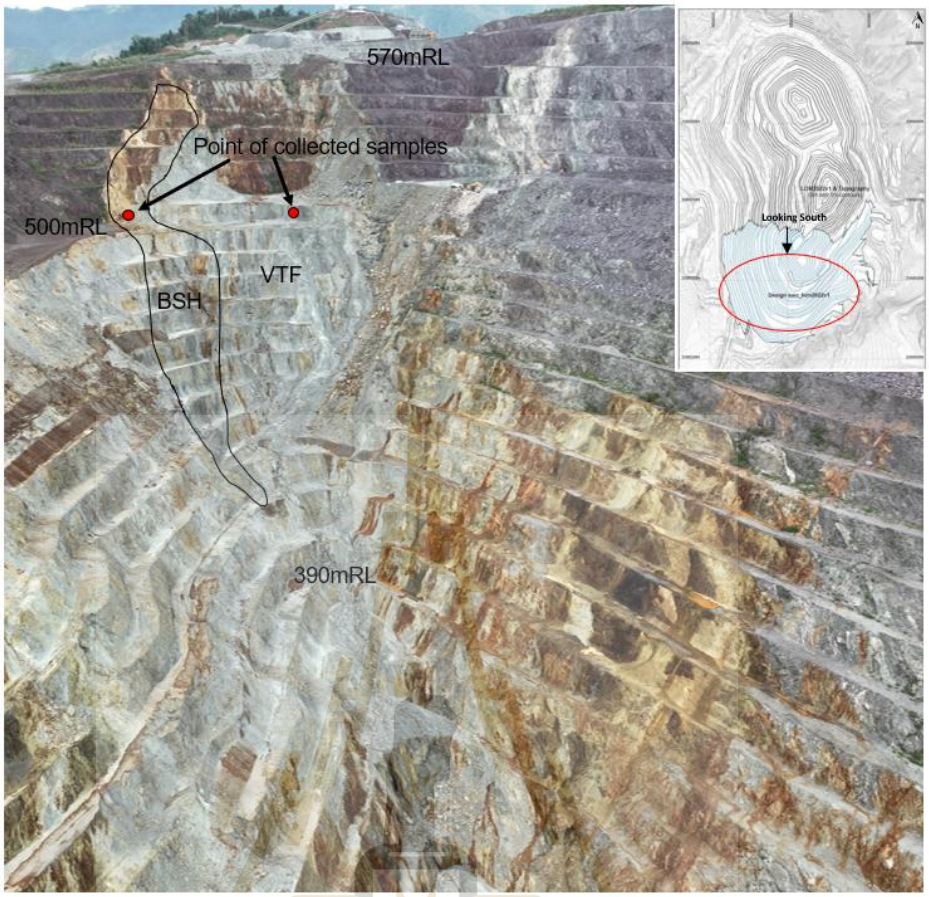


Figure 4.2 Location of collected samples at side wall, Phu Kham mine, Laos.

4.4 Chemical Property Test

The chemical property of samples is determined using X-ray diffraction (see Figure 4.7) and X-ray fluorescence analysis (see Figure 4.8). The samples are tested under air-dry at room temperature of 25° c and oven-dry condition at 110°c. The mineral compositions from XRD analysis are shown in Table 4.3 and XRF results in Table 4.4. The results will be used as basis data to correlate and explain the proportion of minerals and characteristics of each material impact to water based on test results.

Table 4.2 Sieve number and sieve opening following the ASTM D422 standard.

Sieve no.	Sieve opening (mm)
-	19.000
-	9.500
4	4.750
10	2.000
20	0.850
40	0.425
60	0.250
100	0.150
200	0.075
Pan	-



Figure 4.3 Sand cone test of the BSH sample at Phu Kham mine.



Figure 4.4 Sand cone test of the VTF sample at Phu Kham mine.

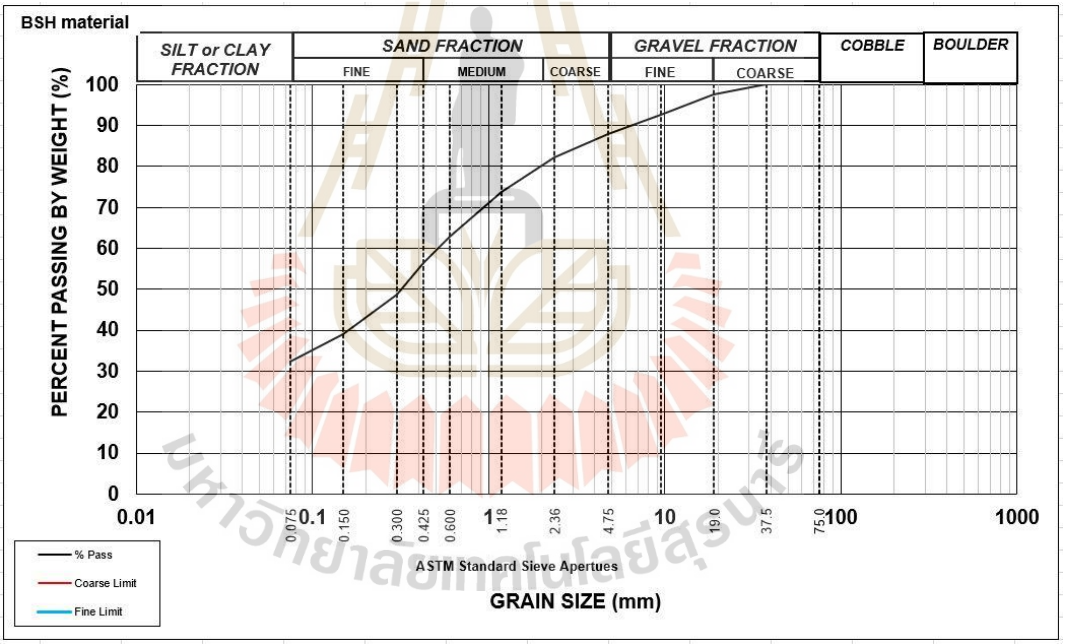


Figure 4.5 Grain size distribution of BSH.

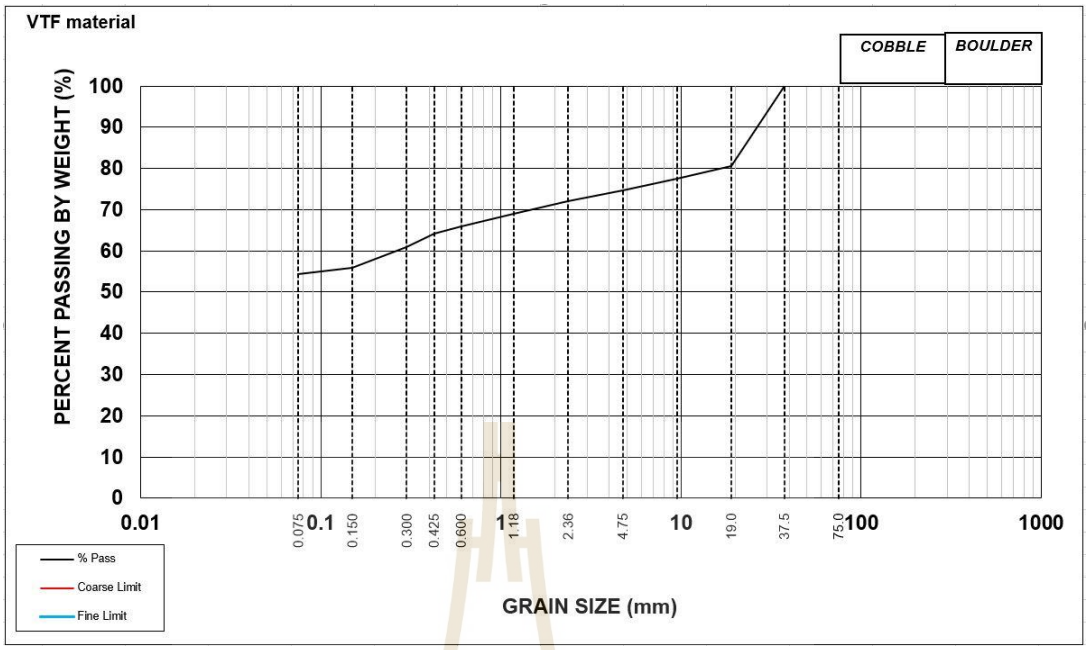


Figure 4.6 Grain size distribution of VTF.



Figure 4.7 X-ray diffraction apparatus at Suranaree University of Technology.



Figure 4.8 X-ray fluorescence apparatus at Suranaree University of Technology.

Table 4.3 Mineral compositions of BSH and VTF by XRD.

Mineral compositions	BSH		VTF	
	Air-Dry (mass%)	Oven-Dry at 25°C (mass%)	Air-Dry (mass%)	Oven-Dry at 25°C (mass%)
Quartz	27.95	6.00	40.90	26.59
Orthoclase	-	-	9.77	21.85
Albite	-	-	0.81	1.03
Kaolinite	42.83	38.58	14.50	17.24
Illite	13.86	7.35	-	-
Nacrite	8.67	11.83	-	-
Muscovite	3.19	6.37	19.95	20.80
Chlorite	-	-	7.41	2.40
Gobbinsite	-	-	1.74	0.88
Butlerite	0.46	2.48	4.19	7.08
Braunite	0.58	1.70	0.71	2.13
Berlinite	1.51	21.14	-	-
Total	100.00	100.00	100.00	100.00

Table 4.4 Mineral compositions of BSH and VTF by X-ray fluorescence.

Formula	BSH		VTF	
	Air-Dry (mass%)	Oven-Dry(mass%)	Air-Dry (mass%)	Oven-Dry(mass%)
Na_2O	4.61	0.78	-	
MgO	2.38	1.78	3.54	3.24
Al_2O_3	28.84	27.73	19.92	18.98
SiO_2	58.10	60.19	66.59	59.84
SO_3	2.66	2.84	3.47	2.32
K_2O	1.19	1.32	2.98	3.20
TiO_2	0.55	0.66	0.43	0.45
Cr_2O_3	0.02	0.02	0.01	0.02
MnO_2	-	-	0.02	0.02
Fe_2O_3	2.96	3.89	2.54	3.17
CuO	0.49	0.64	0.17	0.20
ZnO	0.03	0.03	0.11	0.13
Rb_2O	0.01	0.01	0.02	0.02
Rh_2O_3	-	-	0.12	8.35
BaO	-	-	0.01	0.00
SrO	0.03	0.03	-	-
ZrO_2	0.04	0.01	-	-
PbO	0.09	0.08	0.09	0.08
Total	100.00	100.00	100.00	100.00

มหาวิทยาลัยเทคโนโลยีสุรนารี

CHAPTER V

DIRECT SHEAR TESTING

5.1 Introduction

The direct shear test is performed to determine the shear strength behavior of materials in study area. The results are required as data input in numerical simulation of slope stability models. This Chapter describes the test method, apparatus, and results.

5.2 Sample preparation

Two types of samples are collected from the South wall in the Phu Kham pit. These include the black fault (BSH) and volcanic tuff (VTF). Figures 4.1 show the BSH and VTF samples from drilling database.

A set of direct shear tests on compacted soil samples with varying water contents 0%, 5%, 10%, 15%, 20%, 25%, 30% to 35% by weight are conducted on BSH and VTF samples. The percentages of natural water contents of BSH and VTF are 6.01 and 11.71, respectively (Table 4.1).

Both samples are dried in the oven to remove water content in material before shearing (Figures 5.1 and 5.2). The dried samples were mixed with the calculated volume of water at each percentage of water content and were compacted to nearly dry density obtained from sand cone test before shearing. The volume of water is calculated by the required percentage multiply with weight of dried sample in shear box. After shearing test, the material is dried and then taken to mixed water in the next condition for next shear test.

5.3 Test method

The direct shear test procedure is performed follows the ASTM D3080-04 standard practice. Figure 5.3 shows the direct shear apparatus at Suranaree University of Technology. The dimension of shear box has a diameter per thickness of 2:1. The shear box is 60 mm of diameter and 30 mm of thickness. The prepared sample which is mixed with the calculated volume of water is compacted by proctor energy before testing. The test condition includes normal stress value from different elevation of surface and collected location. Shear testing series is performed under normal loads ranging from 206.9 kPa to 620.7 kPa corresponding to overburden pressures 390-570 mRL. The depth of mine of excavation about 180 meters from ground level is shown in Figure 4.2. The tests are sheared under a constant displacement rate of 0.1 mm/minutes.

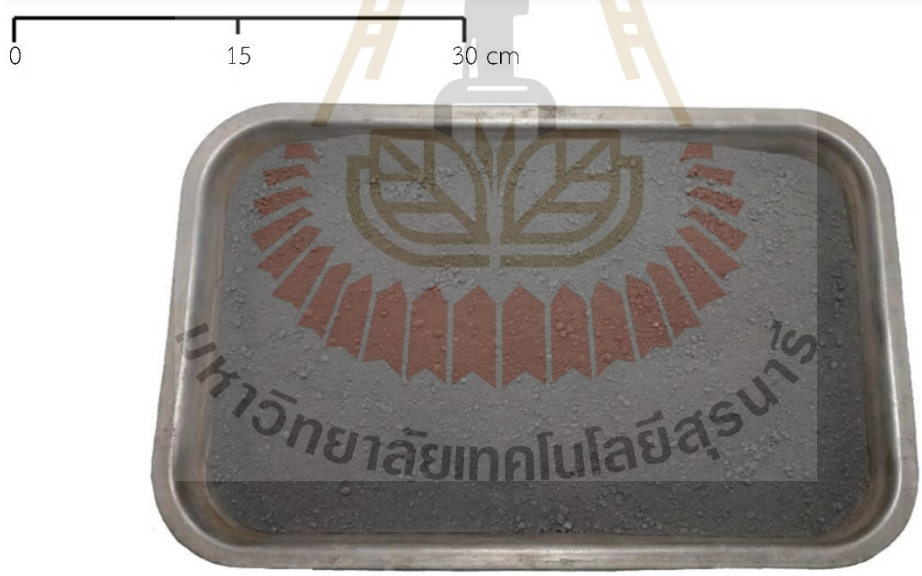


Figure 5.1 BSH sample under dry condition for direct shear test.

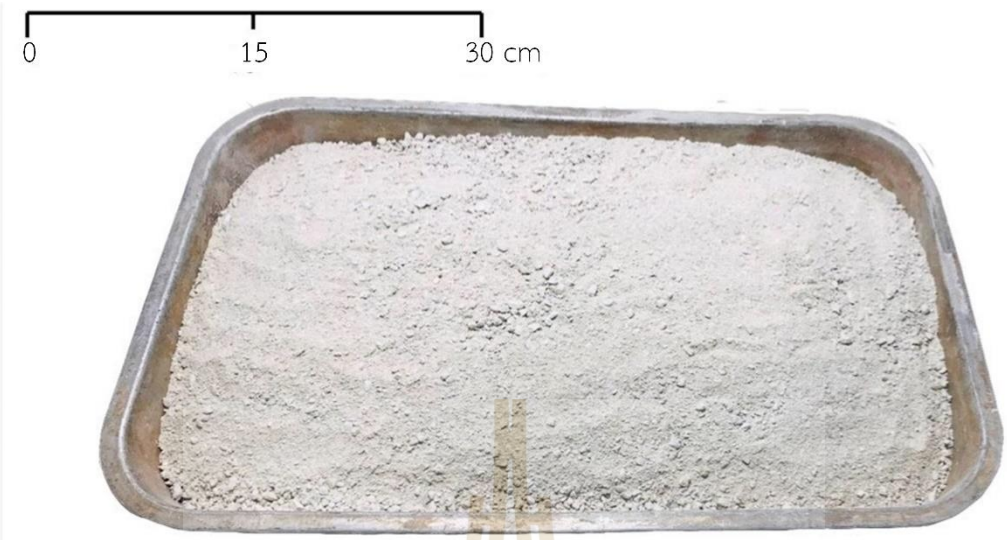


Figure 5.2 VTF sample under dry condition for direct shear test.



Figure 5.3 Direct shear test apparatus at Suranaree University of Technology Laboratory.

มหาวิทยาลัยเทคโนโลยีสุรนารี

5.4 Test results

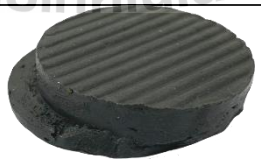
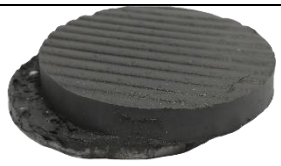
Twenty-four BSH and twenty-four VTF specimens have been tested under varying normal loads and water contents. The pictures of post-test specimens obtained from the direct shear test are given in Table 5.2

Direct shear test results are plotted as a function shear strength with displacement and function shear strength with normal stress for shearing parameters, as shown in Figures 5.4 to 5.19. Results show that shear strength is increased with increasing normal load test. The three normal loads are performed by direct shear test for the investigation of cohesion and friction angle values in each water content condition. BSH and VTF data are summarized peak shear stress, and shear strength data are shown in Tables 5.3 and 5.4, respectively.

Figure 5.20 shows the relation of shear stress varying different water contents. The result indicates that shear stress is decreased with increasing water content at the same normal load condition.

มหาวิทยาลัยเทคโนโลยีสุรนารี

Table 5.1 Post-test BSH and VTF of direct shear test with various water contents.

Water contents	BSH	VTF
0%		
5%		
10%		
15%		
20%		
25%		
30%		
35% 0 2 4 6 cm		

มหาวิทยาลัยเทคโนโลยีสุรนารี

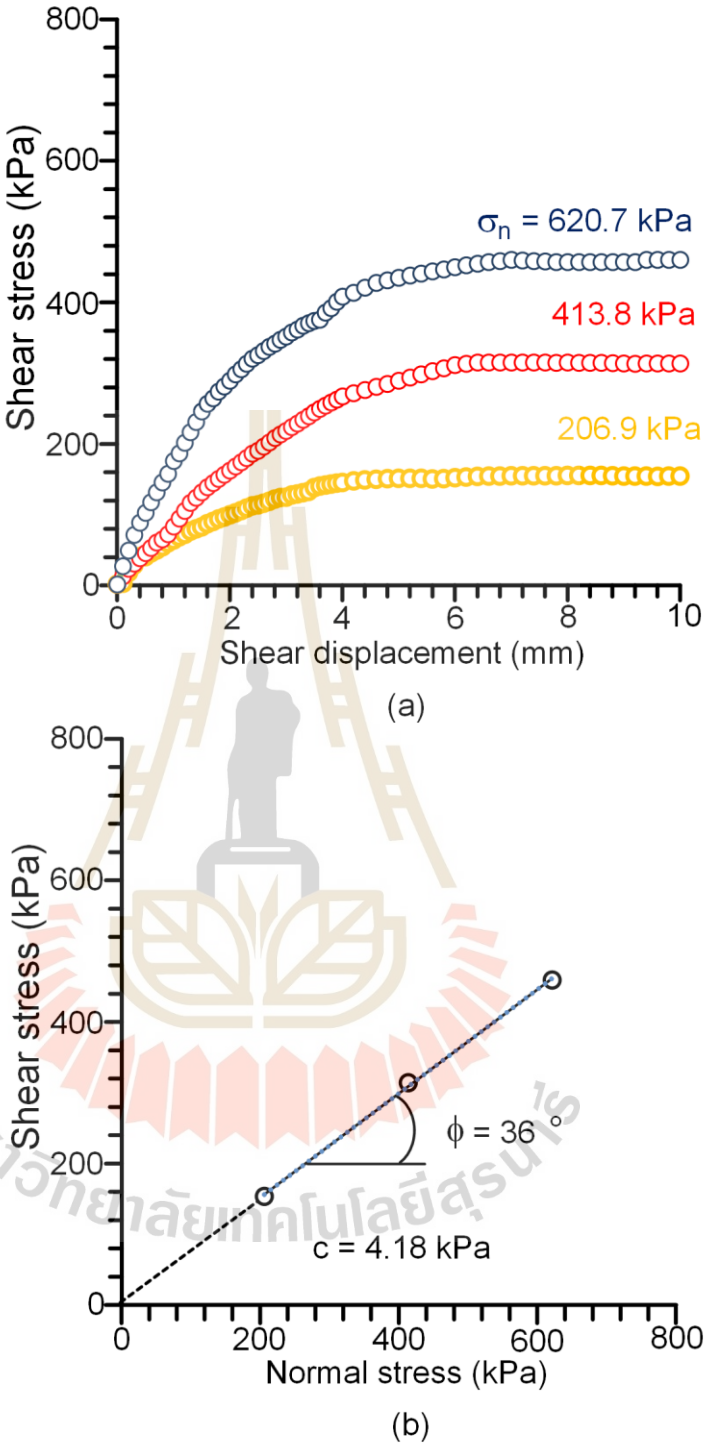


Figure 5.4 Relationships of shear stress with displacement (a) and shear stress with normal stress of BSH at 0% water content condition (b).

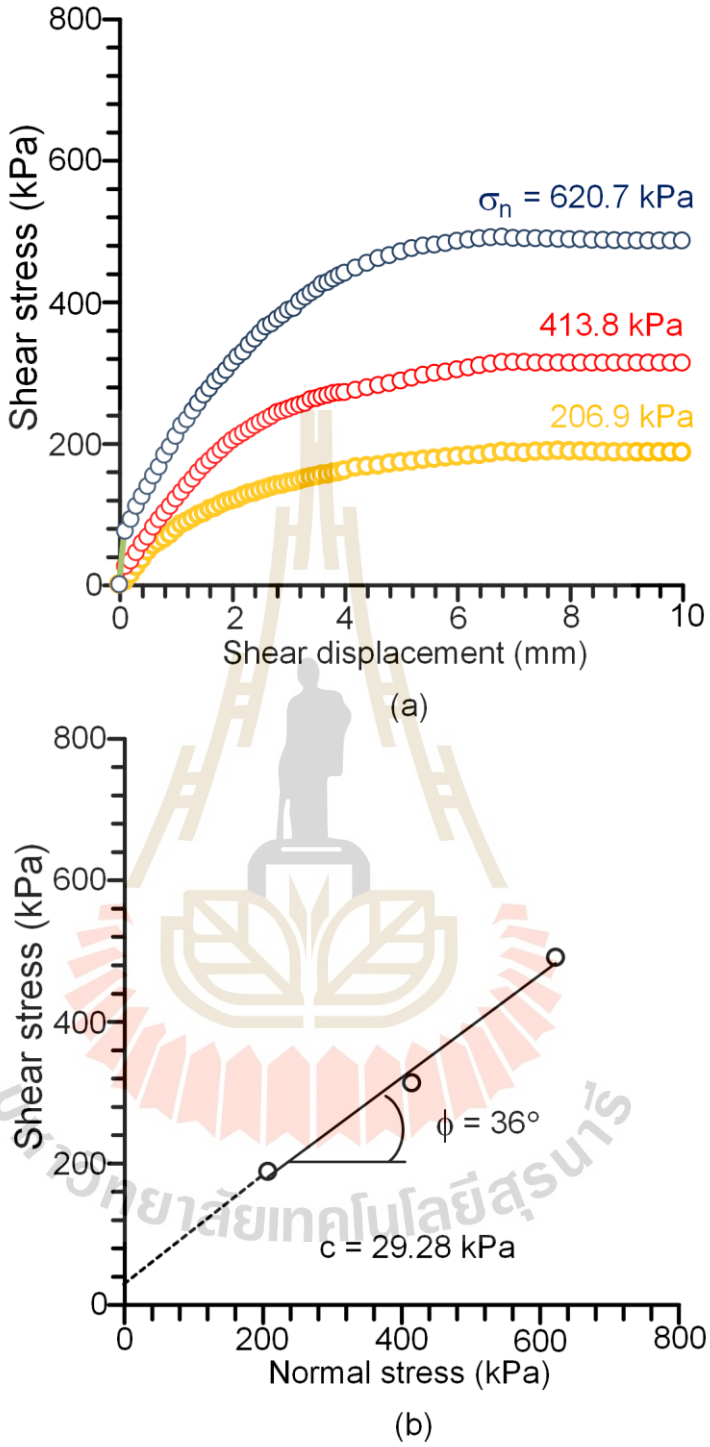


Figure 5.5 Relationships of shear stress with displacement (a) and shear stress with normal stress of BSH at 5% water content condition (b).

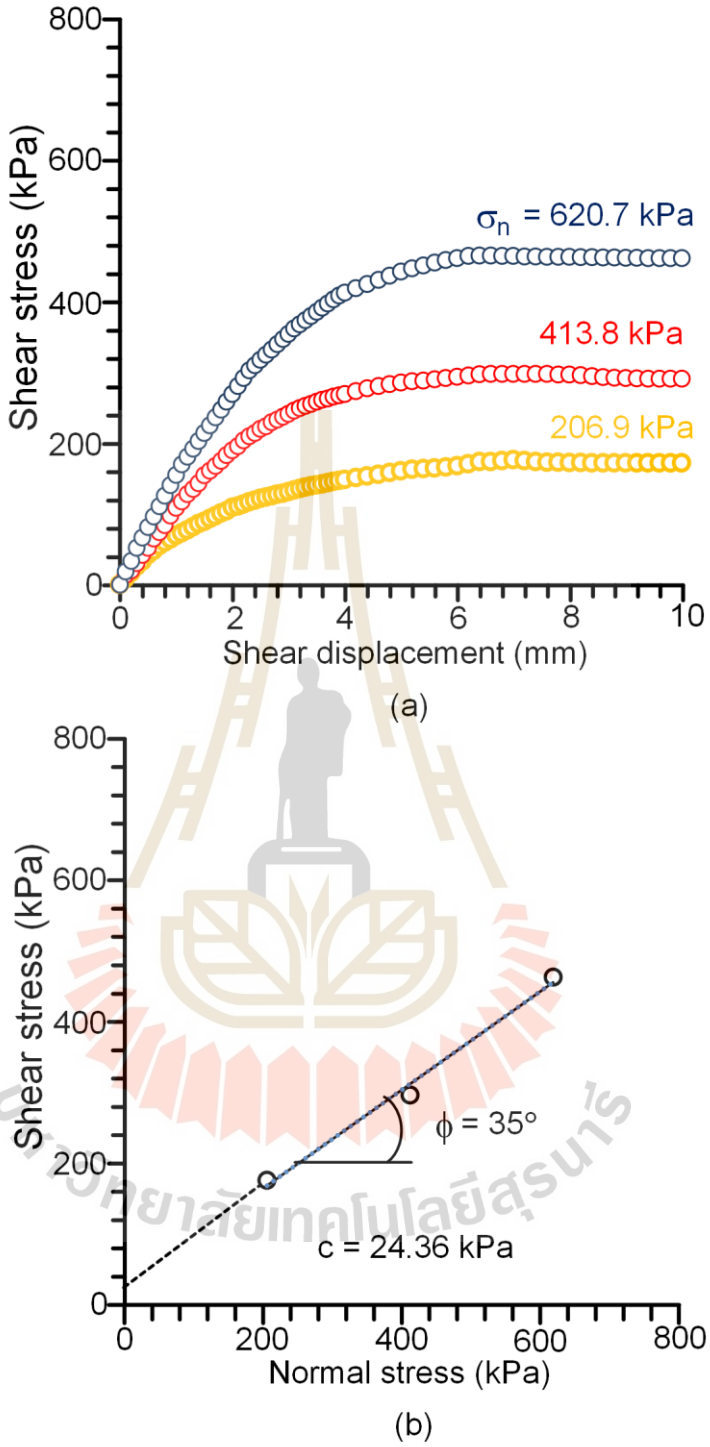


Figure 5.6 Relationships of shear stress with displacement (a) and shear stress with normal stress of BSH at 10% water content condition (b).

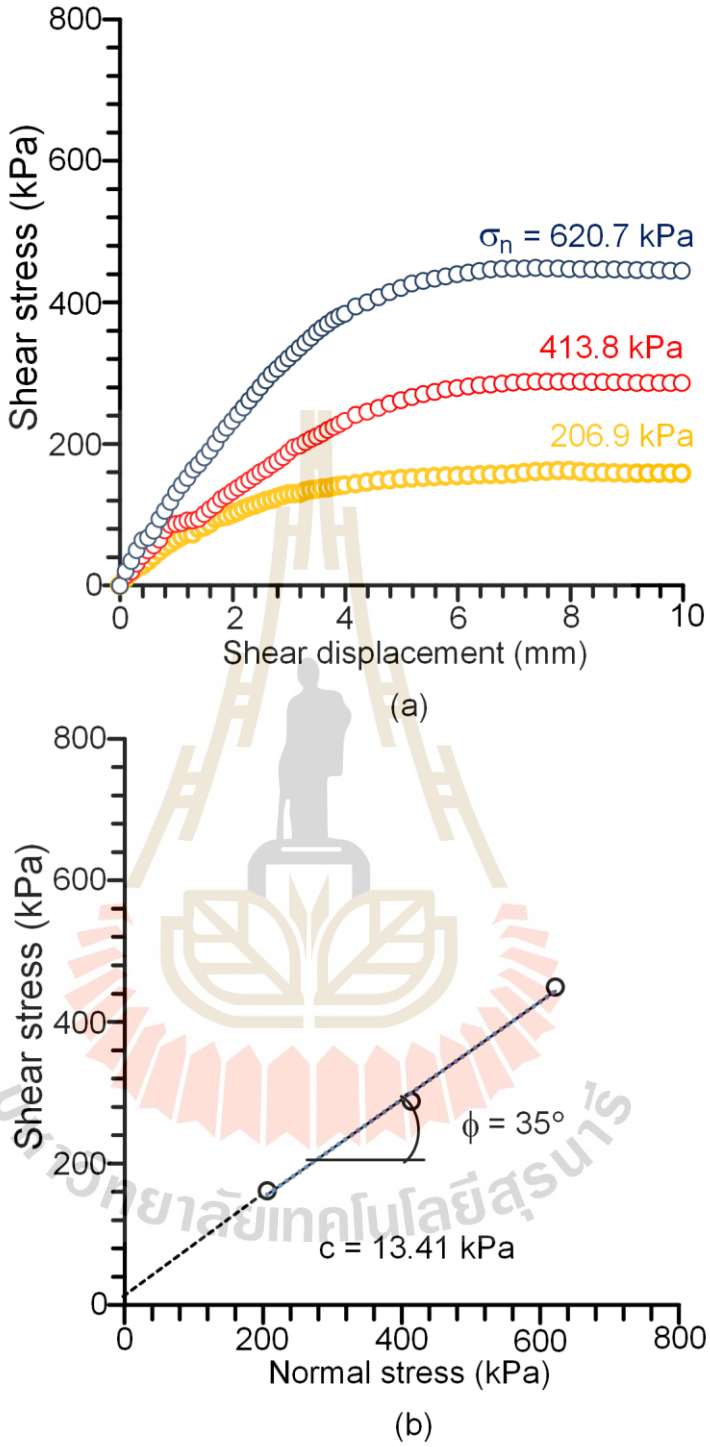


Figure 5.7 Relationships of shear stress with displacement (a) and shear stress with normal stress of BSH at 15% water content condition (b).

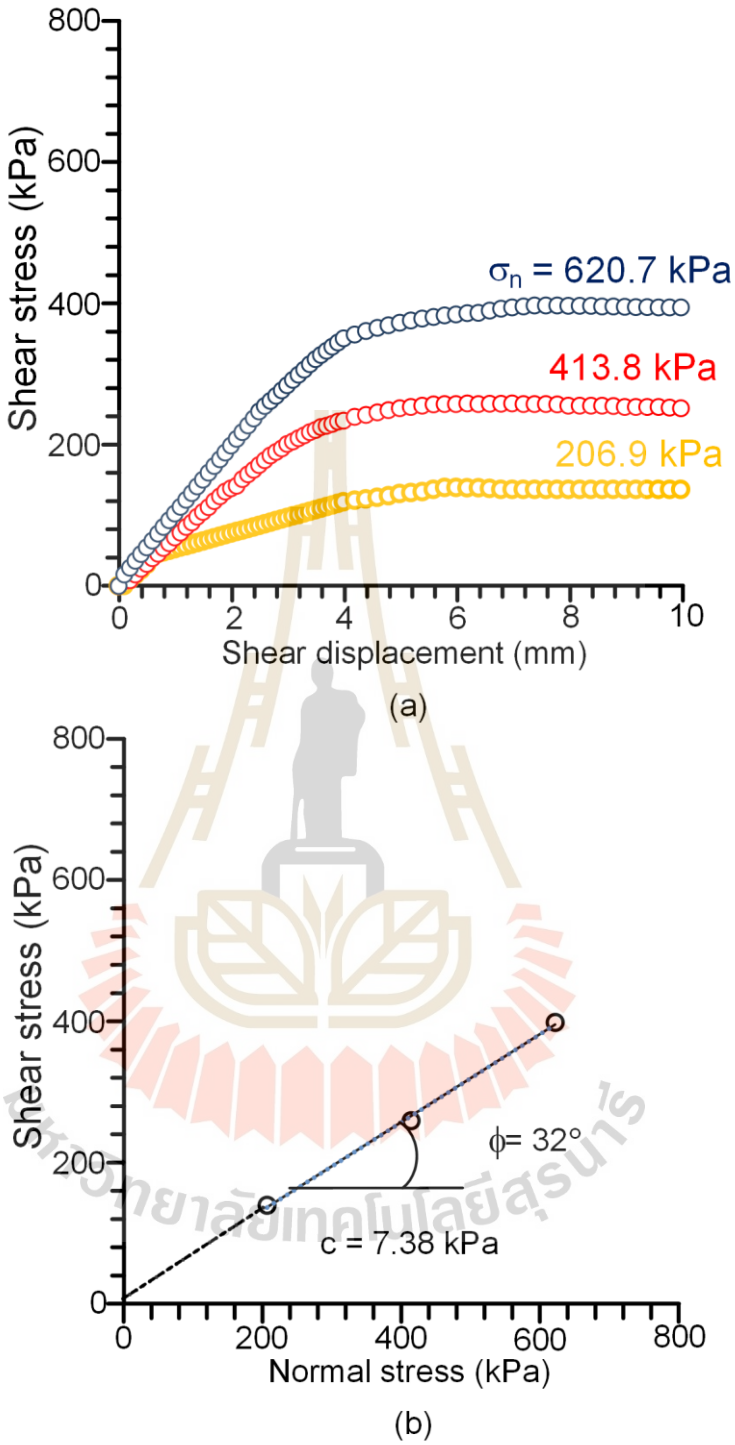


Figure 5.8 Relationships of shear stress with displacement (a) and shear stress with normal stress of BSH at 20% water content condition (b).

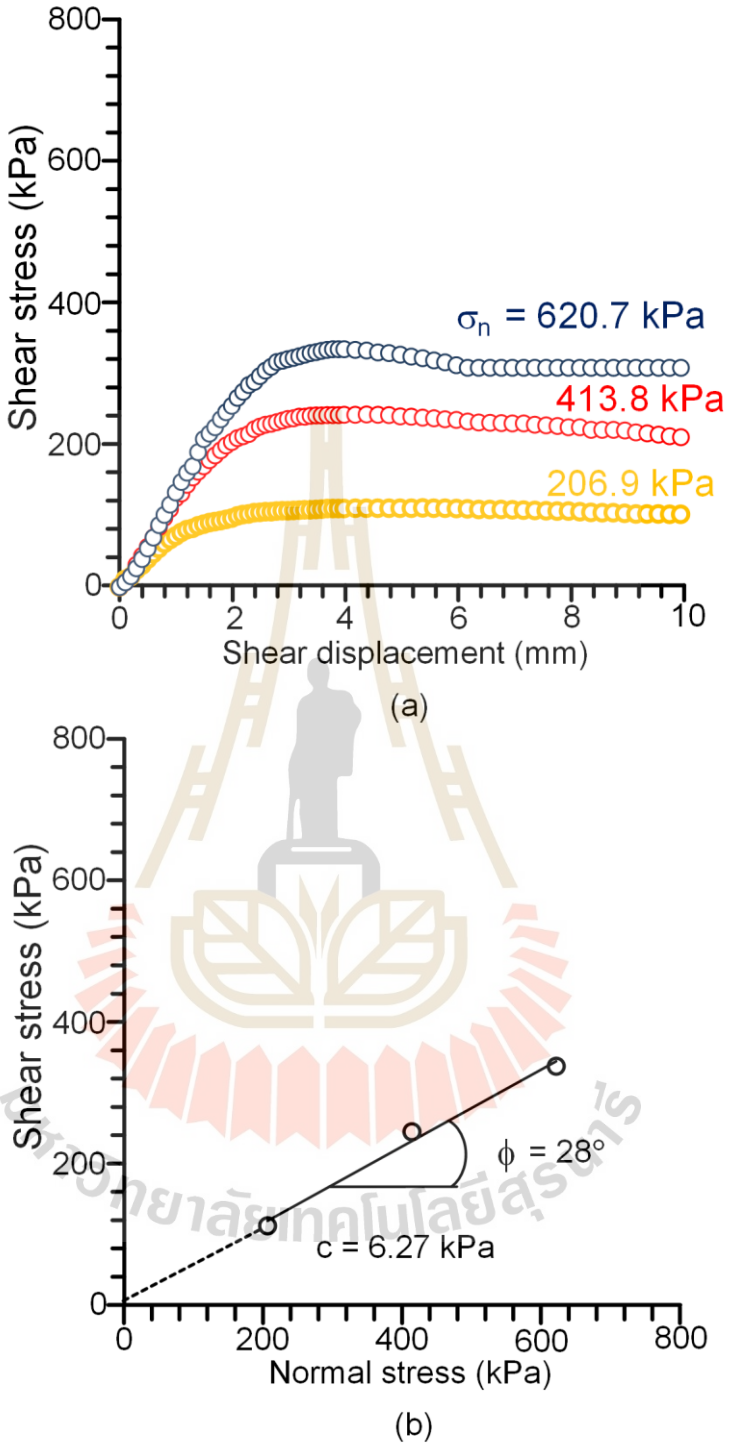


Figure 5.9 Relationships of shear stress with displacement (a) and shear stress with normal stress of BSH at 25% water content condition (b).

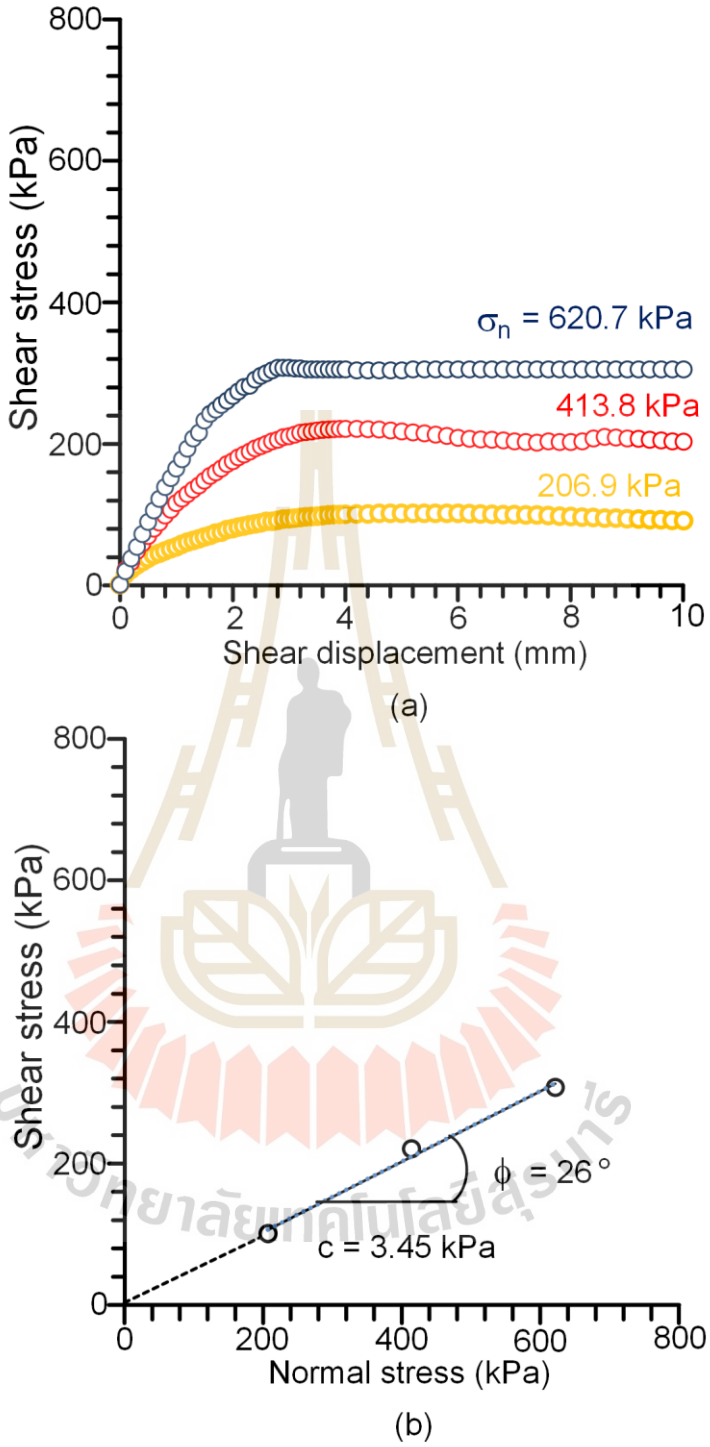


Figure 5.10 Relationships of shear stress with displacement (a) and shear stress with normal stress of BSH at 30% water content condition (b).

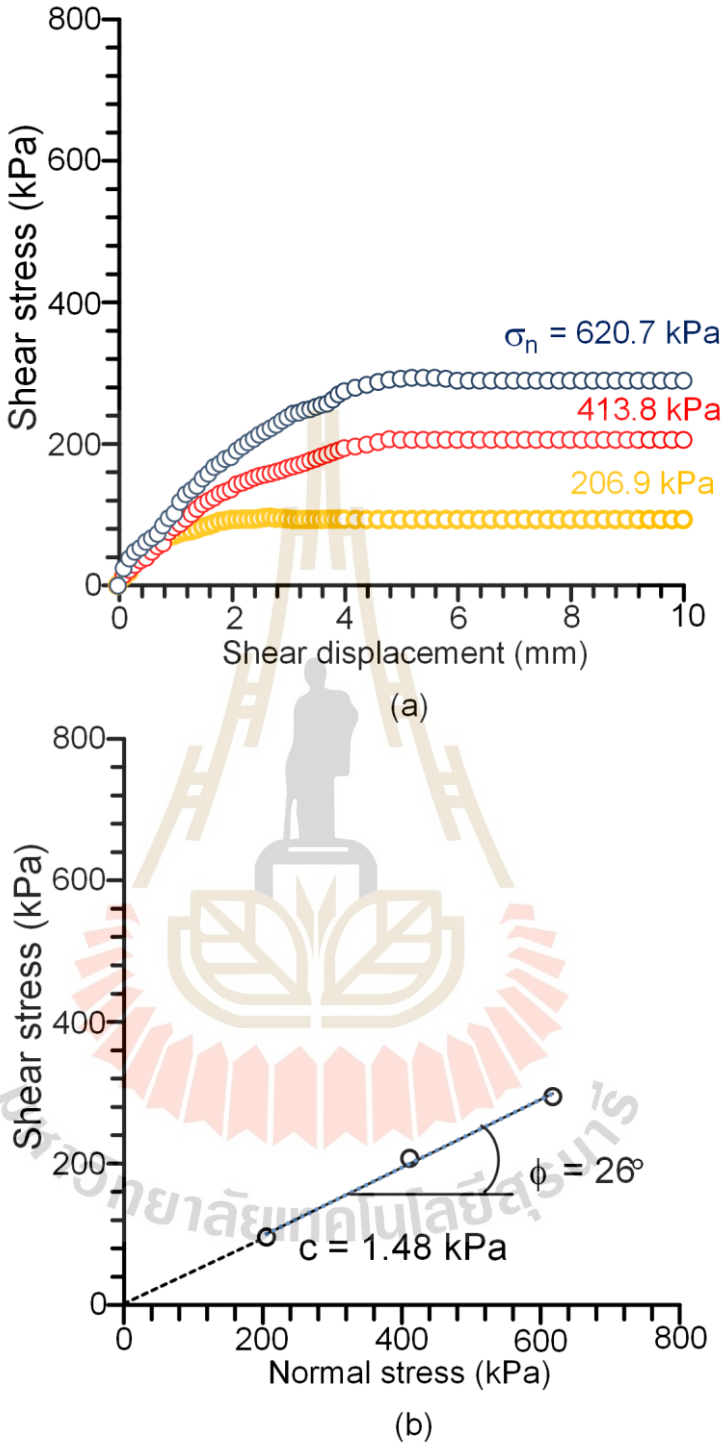


Figure 5.11 Relationships of shear stress with displacement (a) and shear stress with normal stress of BSH at 35% water content condition (b).

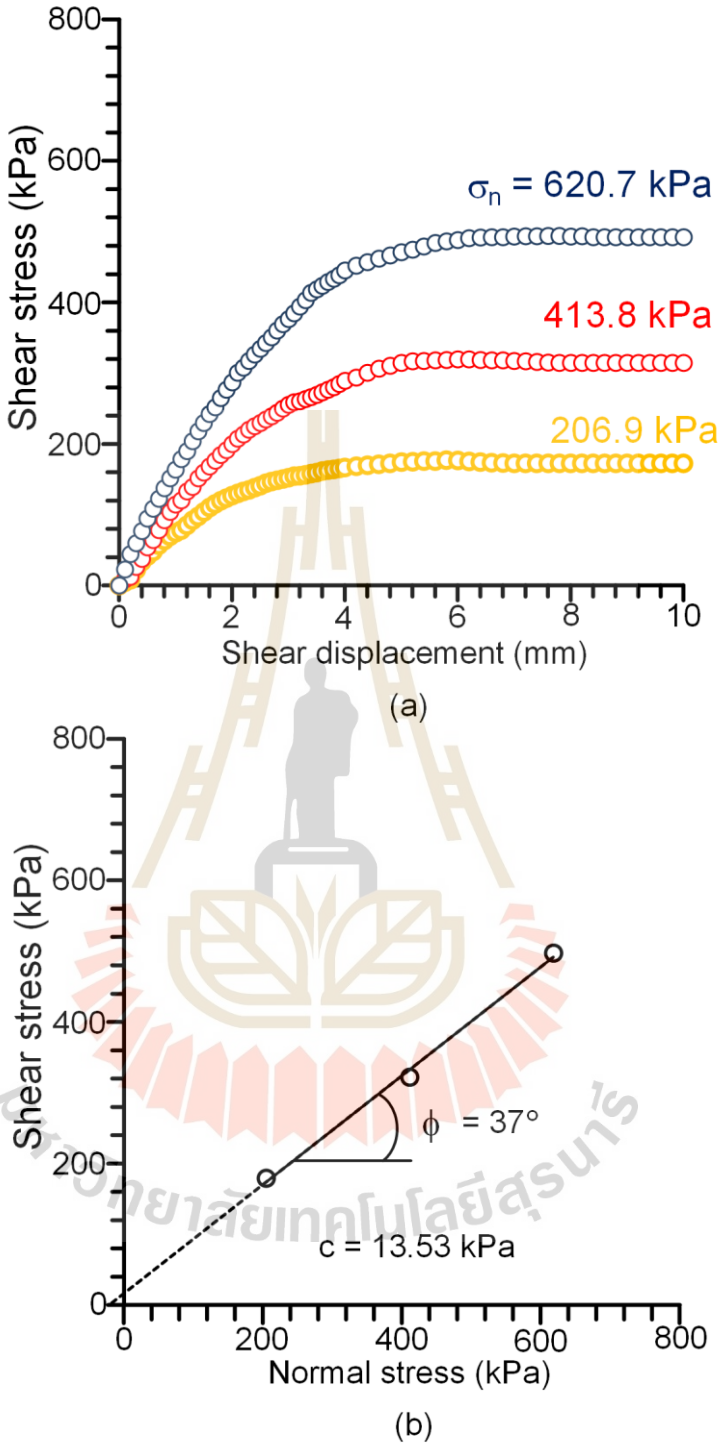


Figure 5.12 Relationships of shear stress with displacement (a) and shear stress with normal stress of VTF at 0% water content condition (b).

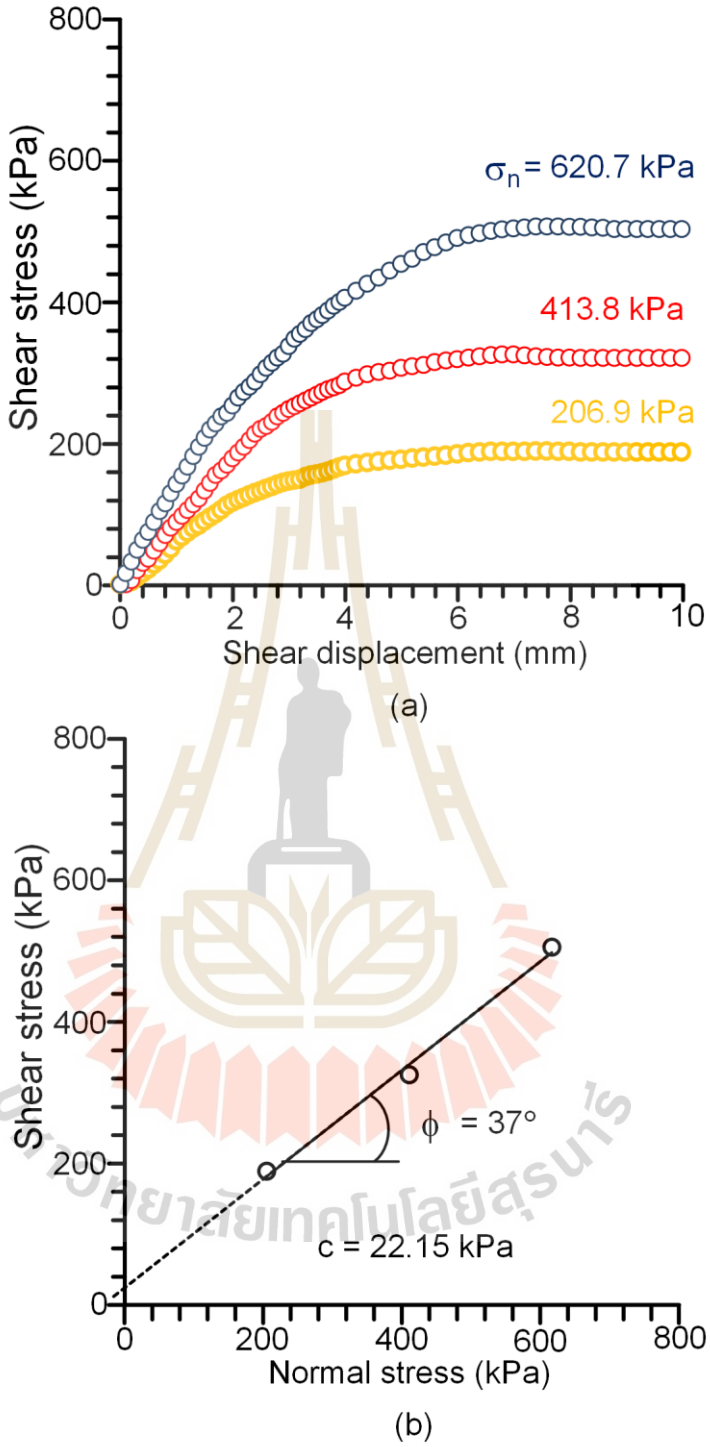


Figure 5.13 Relationships of shear stress with displacement (a) and shear stress with normal stress of VTF at 5% water content condition (b).

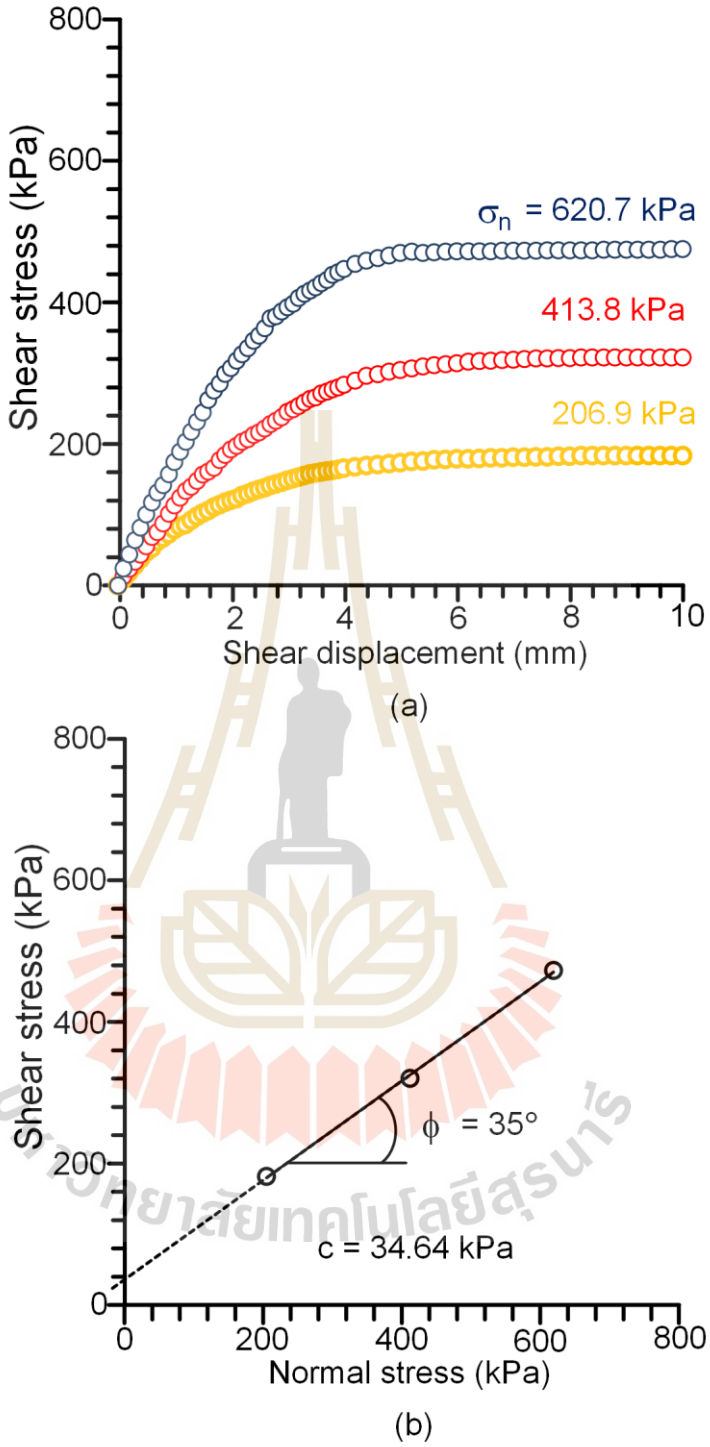


Figure 5.14 Relationships of shear stress with displacement (a) and shear stress with normal stress of VTF at 10% water content condition (b).

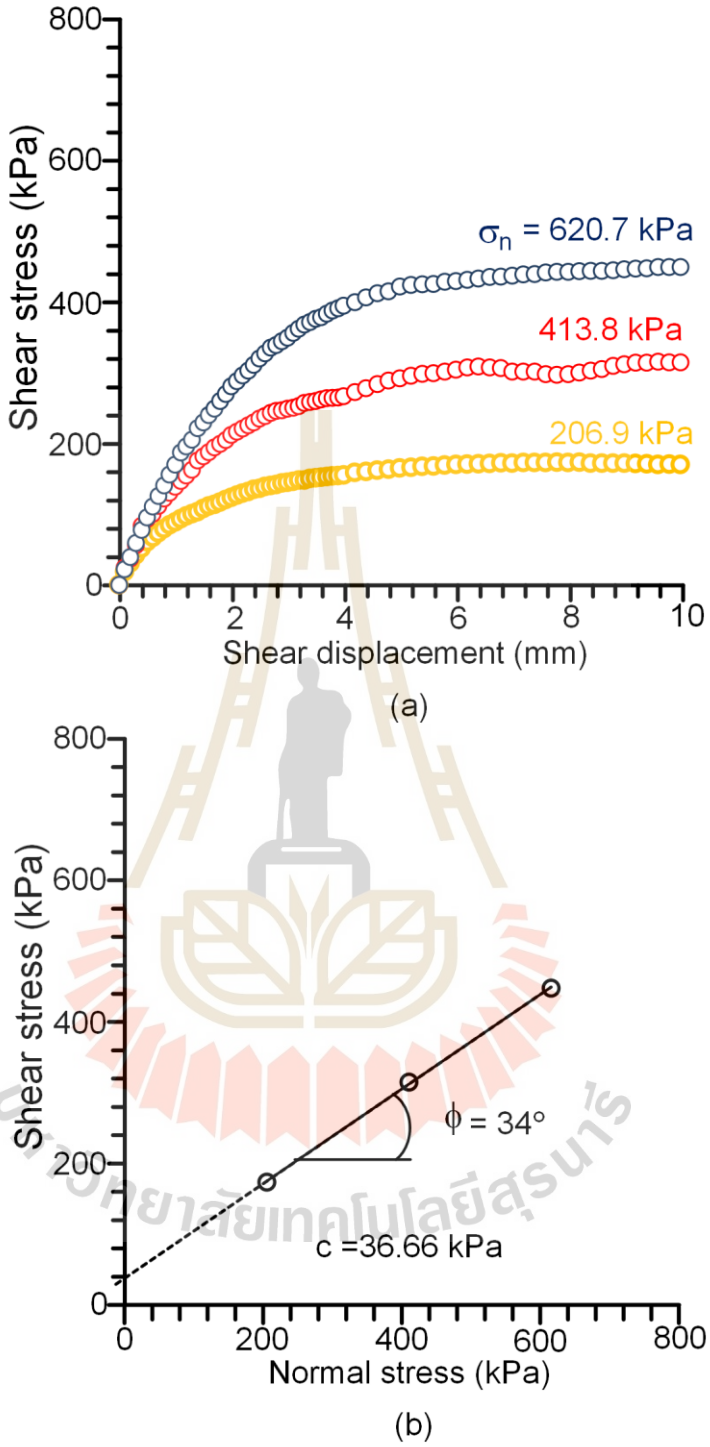


Figure 5.15 Relationships of shear stress with displacement (a) and shear stress with normal stress of VTF at 15% water content condition (b).

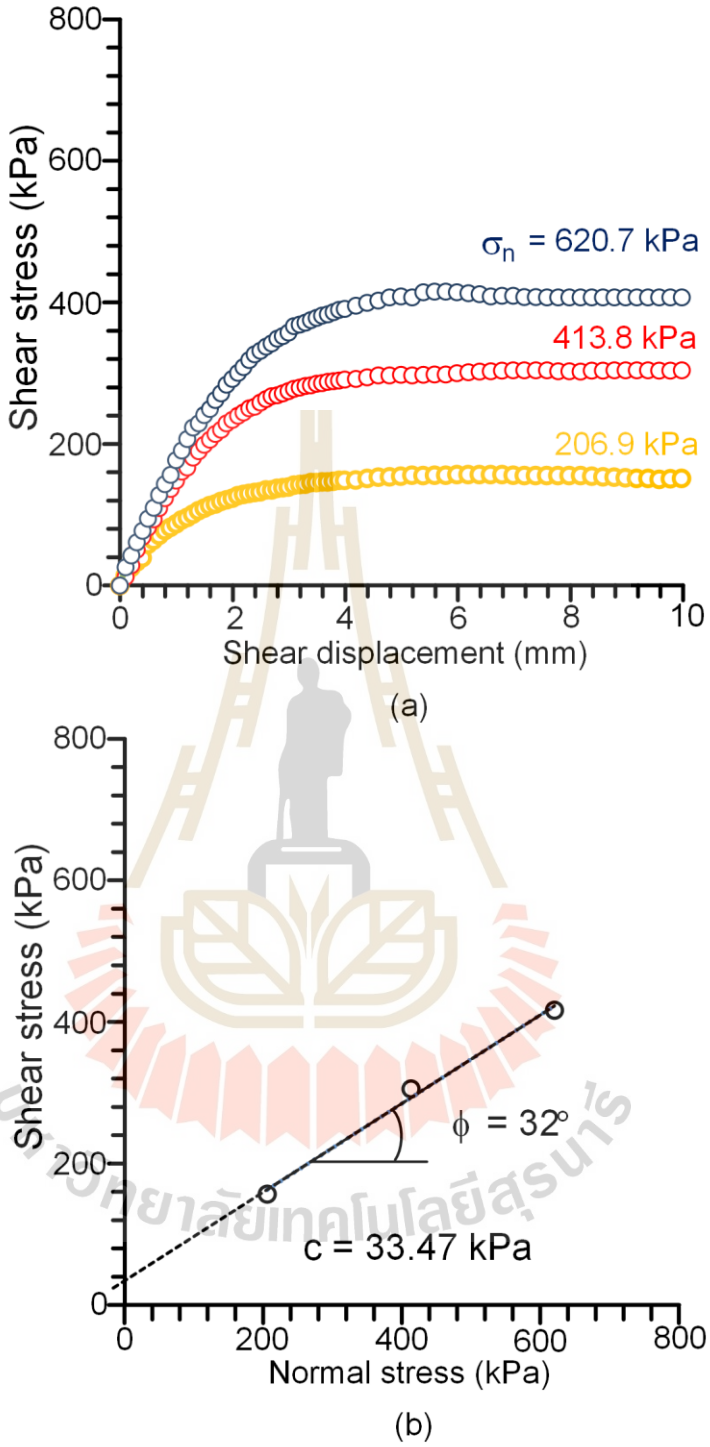


Figure 5.16 Relationships of shear stress with displacement (a) and shear stress with normal stress of VTF at 20% water content condition (b).

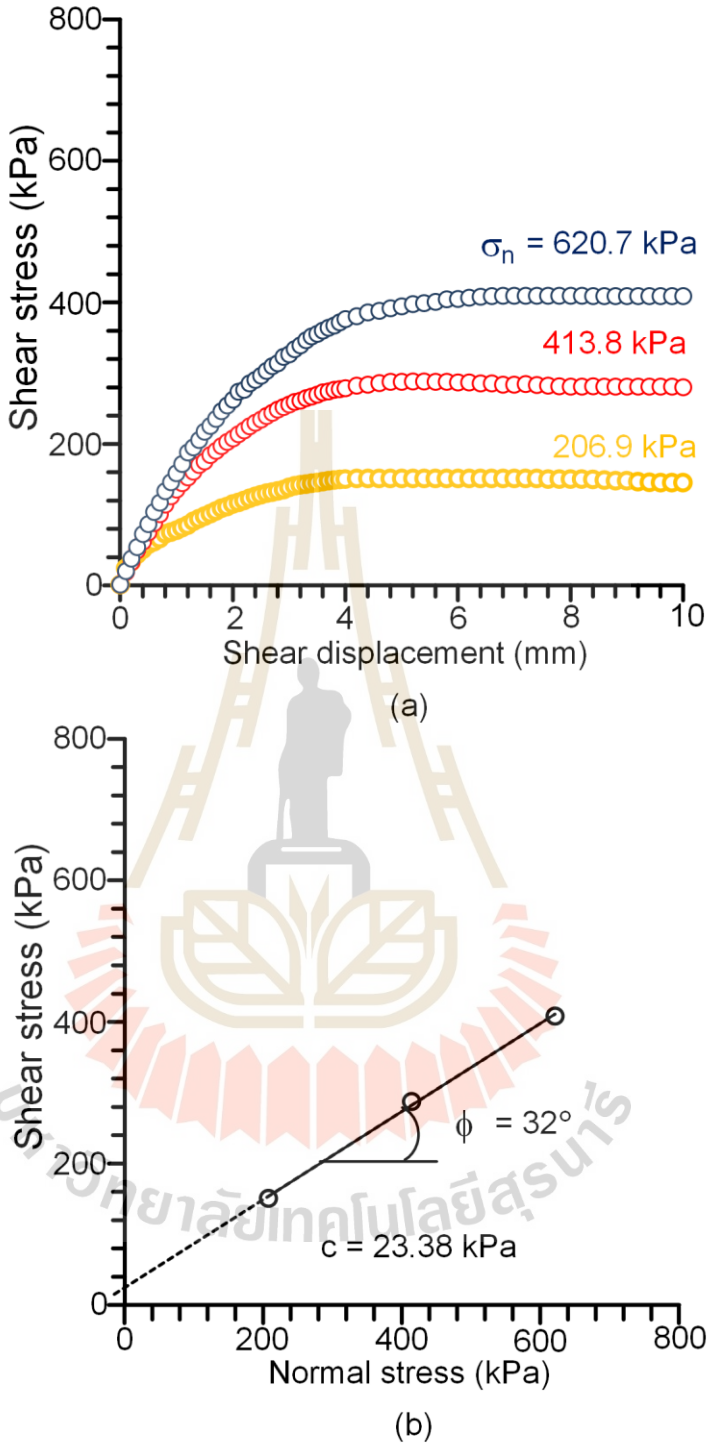


Figure 5.17 Relationships of shear stress with displacement (a) and shear stress with normal stress of VTF at 25% water content condition (b).

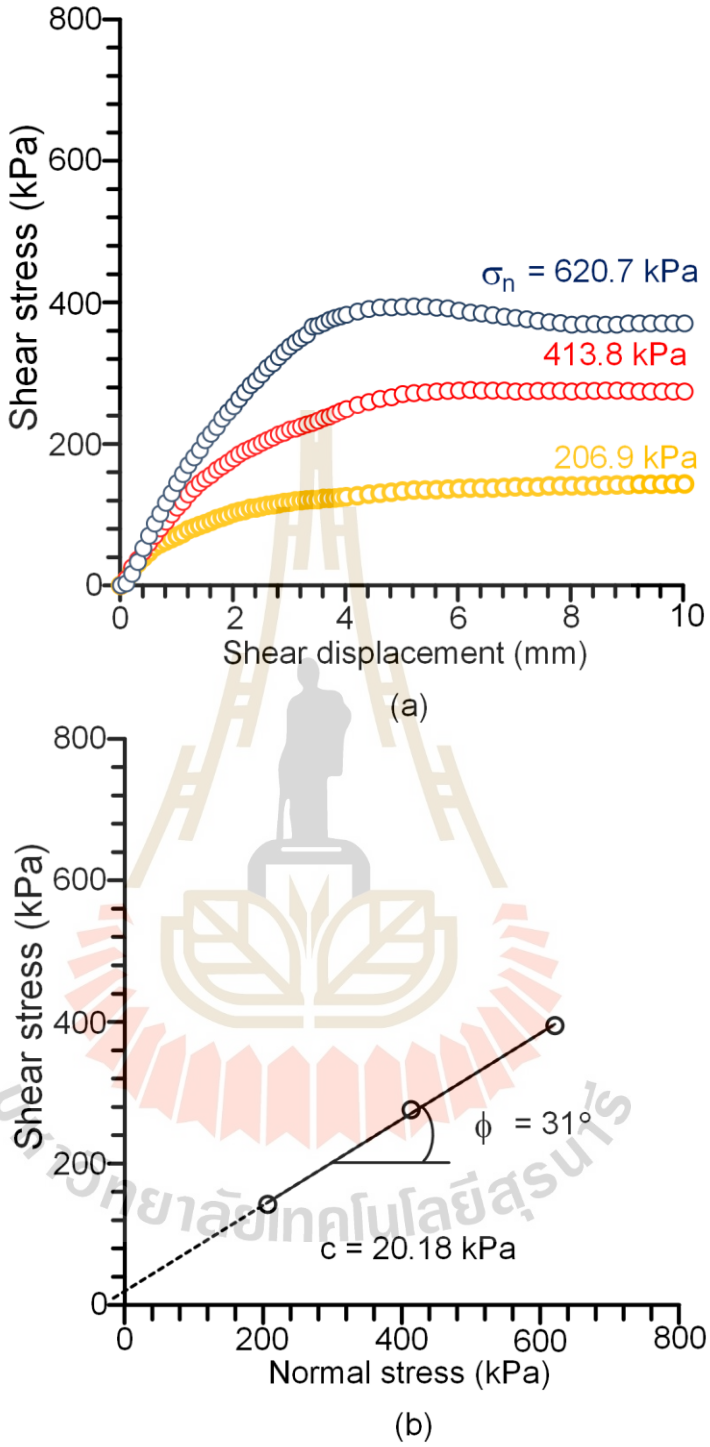


Figure 5.18 Relationships of shear stress with displacement (a) and shear stress with normal stress of VTF at 30% water content condition (b).

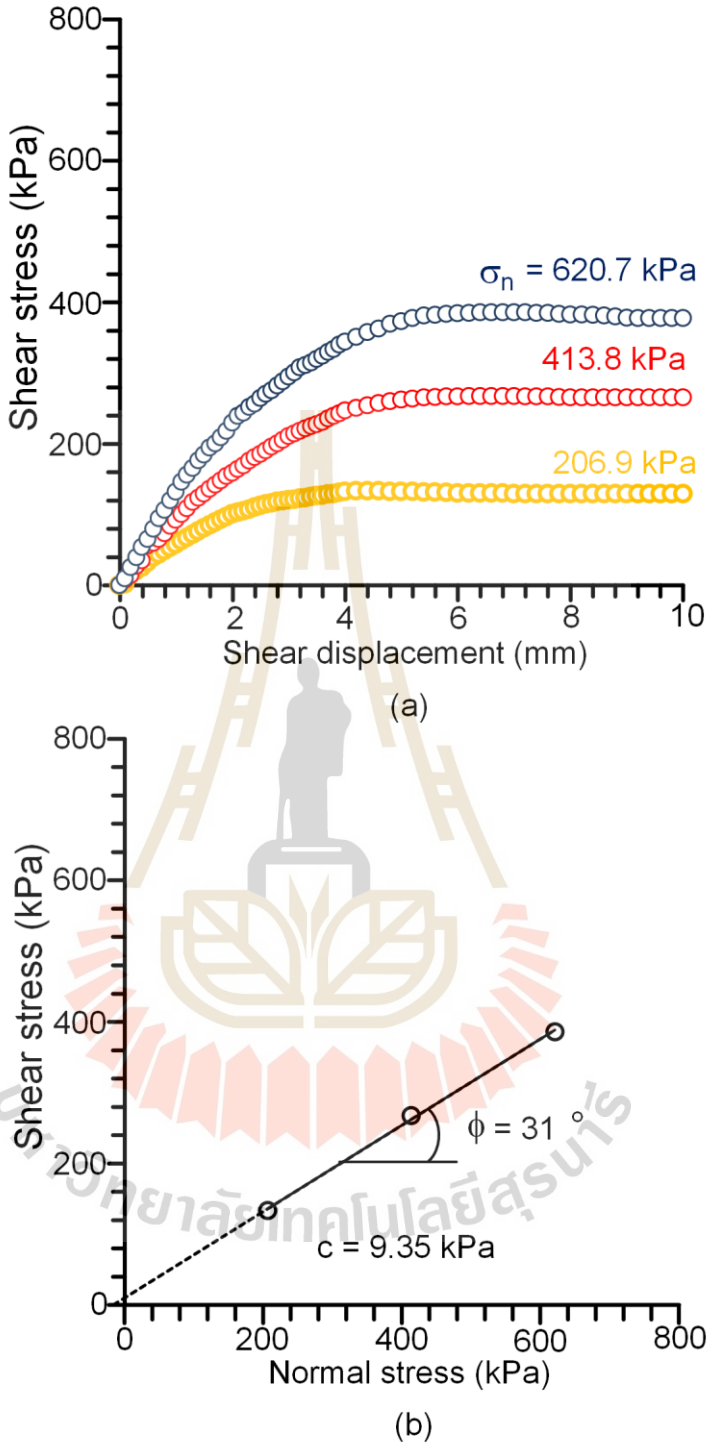


Figure 5.19 Relationships of shear stress with displacement (a) and shear stress with normal stress of VTF at 35% water content condition (b).

Table 5.2 Peak shear stress and shear parameters of BSH for 390-570 mRL

Water content (%)	Peak shear stress (kPa)			Cohesion	Friction angle
	206.9 kPa	413.8 kPa	620.7 kPa	(kPa)	degree
0	203.9	327.7	512.4	4.18	36
5	189.0	313.7	490.9	29.28	36
10	176.4	297.5	465.1	24.36	35
15	162.4	287.9	448.8	13.41	35
20	139.5	258.4	397.2	7.38	32
25	111.8	244.0	336.3	6.27	28
30	100.8	220.0	306.4	3.45	26
35	96.3	206.7	293.8	1.48	26

Table 5.3 Peak shear stress and shear parameters of VTF.

Water content (%)	Peak shear stress (kPa)			Cohesion	Friction angle
	206.9 kPa	413.8 kPa	620.7 kPa	(kPa)	degree
0	177.2	319.6	493.9	13.53	37
5	188.2	324.8	505.7	22.15	37
10	183.1	321.9	474.7	34.64	35
15	173.1	315.2	448.8	36.66	34
20	156.5	304.1	414.9	33.47	32
25	149.9	287.2	408.2	23.38	32
30	143.2	276.1	394.2	20.18	31
35	132.9	267.2	385.3	9.35	31

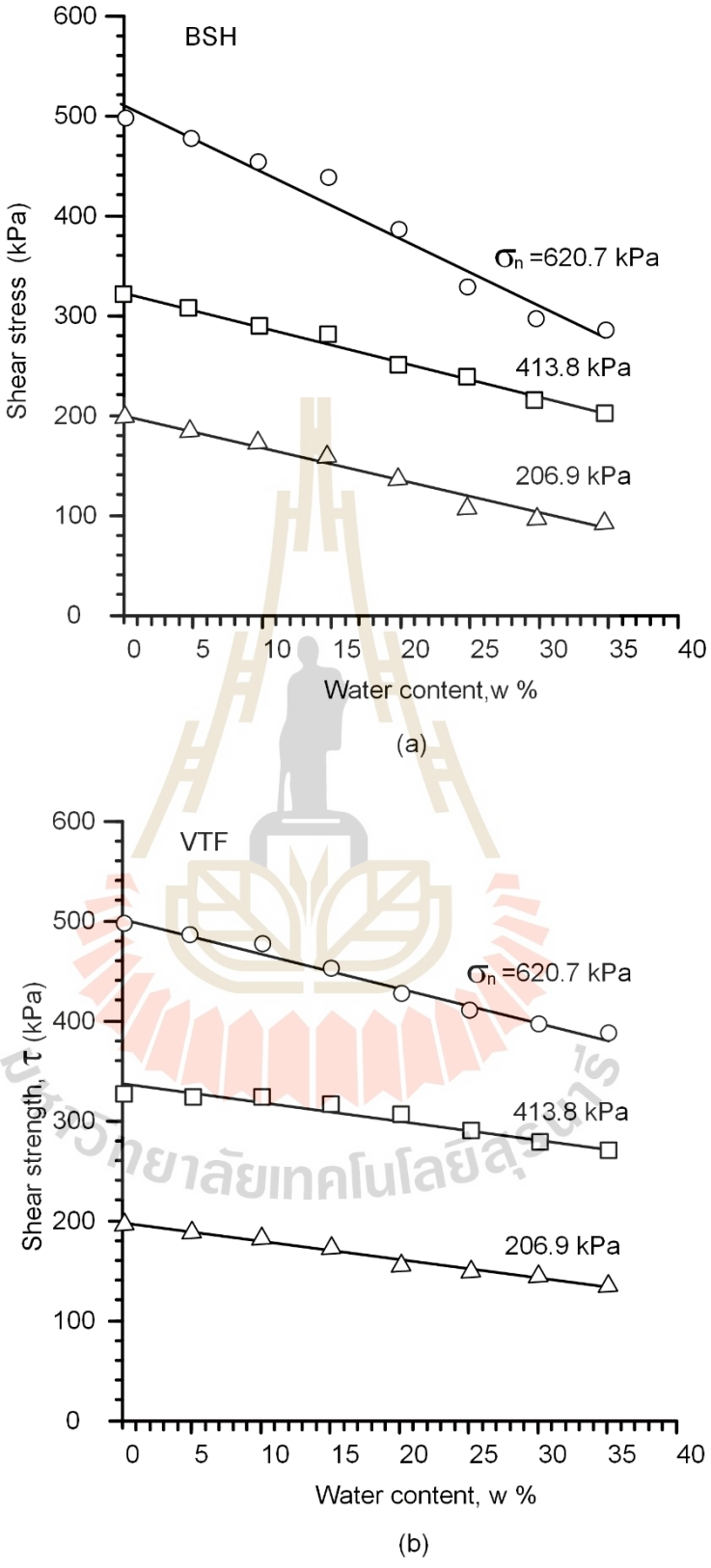


Figure 5.20 Shear strength as a function of water content of BSH (a) and VTF (b) at different normal stress.

CHAPTER VI

NUMERICAL SIMULATIONS

6.1 Introduction

This chapter describes the results of slope stability analysis using limit equilibrium method in Slide 2D software. The numerical simulation is performed to determine slope stability under water contents with varying slope face angles, heights and shear parameters (cohesion and friction angel) from test results. The simulation models uses mechanical properties from laboratory and study area results.

6.2 Slope geometry

The distance between the fault and toe is 130 m, between the toe and left boundary is 100 m, and between the crest and right boundary is 50 m. The slope face angles are varied from 20, 30, 40, 50 to 60 degrees, and the slope heights are 50, 100, 150, and 200 m. The fault of BSH is 2 m in thickness. Figure 6.1 shows the representative boundary condition of the slope. The boundary shows a hanging wall of various VTF material, and the footwall is SLR material. The BSH seam will cut on the slope face (see Figure 6.1 (a)) while in case of unexposed BSH on the slope due to steep slope angle or low slope height of models see Figure 6.1 (b). The models use mechanical properties obtained from laboratory and study area results (Tables 6.1 and 6.2). The tables show unit weight, cohesion (c), and friction angle (ϕ) of BSH and VTF from laboratory test but SLR properties from study area data (Table 3.2).

Table 6.1 Summary of mechanical properties using in the simulation.

Material	Unit weight (kN/m^3)	Strength criteria	UCS (kPa)	GSI	Mi	D
SLR	26	Generalized Hoek Brown	30000	66	15	0.7

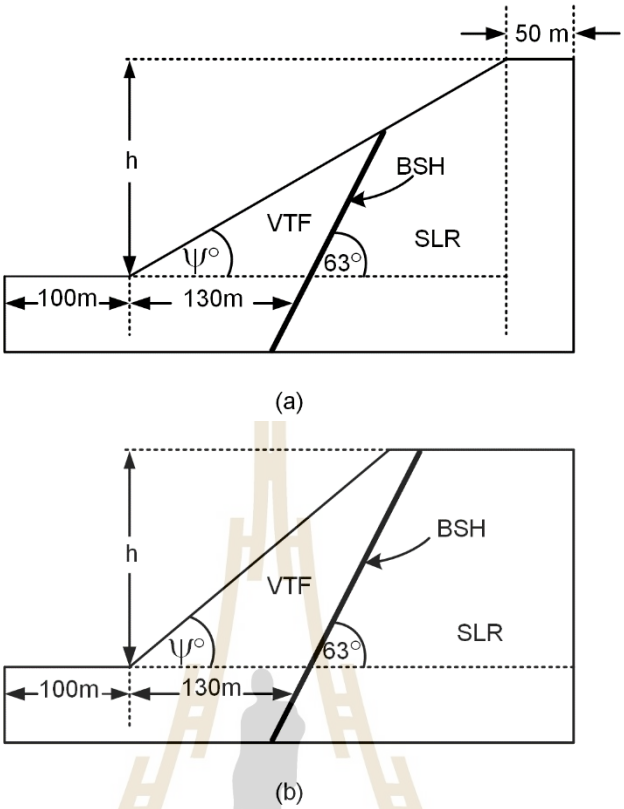


Figure 6.1 Boundary conditions of exposed BSH on slope (a) and unexposed BSH on slope (b).

Table 6.2 Summary of cohesion and friction angle used in simulations for BSH and VTF

Water content (%)	BSH		VTF	
	c (kPa)	ϕ (degrees)	c (kPa)	ϕ (degrees)
0	4.18	36	13.53	37
5	29.28	36	22.15	37
10	24.36	35	34.64	35
15	13.28	35	36.66	34
20	7.38	32	33.46	32
25	6.27	28	23.37	32
30	3.45	26	20.17	31
35	1.48	26	9.35	31

6.3 Simulation model

The computer simulations are performed by using SLIDE2D software based on the limit equilibrium slope stability method. The geometric and boundary conditions were defined in the analyses to identify the Phu Kham mine slope with various slope face angles and slope heights. The mechanical properties (cohesion, c, and friction angle, ϕ) obtained from the laboratory results are inputted in the model (see Table 6.2). The models are studied with the Bishop method (Bishop, 1955) by the Mohr-Coulomb equation. The cohesion and friction angles of VTF (hanging wall) and BSH (black fault) are varied following different water contents and maintained constant shear strength of SLR (footwall)

6.4 Simulation results

6.4.1. Effect of slope face angle

Slope face (ψ) are varied from 20, 30, 40, 50 and 60 in Figures 6.2 and 6.3. These figures show the results of simulated slope as a function of slope face angles and slopes heights with various water contents of BSH at 5, 20 and 35%, and of VTF at 0, 5, 10, 15, 20, 25, 30 and 35%. The results indicate that the factors of safety (FS) decrease with increasing slopes face angles and water contents. The water contents of BSH are less sensitive on slope stability. Effect of slope face angle is related with slope height value.

6.4.2. Effect of position of exposed BSH plane on slope face

The BSH plane is defined at 63 degrees and distance from toe to plane at 130 m on the simulation model. This study defines 2 cases, exposed and unexposed of weak BSH plane on slope face while models were simulated. The case of unexposed BSH plane on slope face is classified are 2 types; from low slope height and steep slope face. Example of BSH plane do not appear on slope face due to low slope height condition at 50 and 100 m in Figure 6.4 (a) and (b), respectively. Figure 6.5 shows BSH do not appear on slope face at 40° and 50° in Figure 6.5 (a) and (b), respectively. The positions of BSH plane must be suitable slope face angle and slope height will be appeared on slope face of simulated model in Figure 6.6. Table 6.3 is summary of cases of BSH position plane on simulated models.

6.4.3. Effect of water content of VTF and slope height

The variation of water contents of VTF from 0, 5, 10, 15, 20, 25, 30, 35 by weight, affects factor of safety at same slope face and height conditions in Figures 6.7, to 6.9. Slope height is affected by position of exposed BSH plan on slope face. The results indicate that factor of safety is decreased with increasing slope height in case of BSH plan do not appear on slope face. Effect of exposed BSH plane on slope shows factors of safety is higher than unexposed BSH on slope case at same conditions (slope face, slope height and water content).

มหาวิทยาลัยเทคโนโลยีสุรนารี

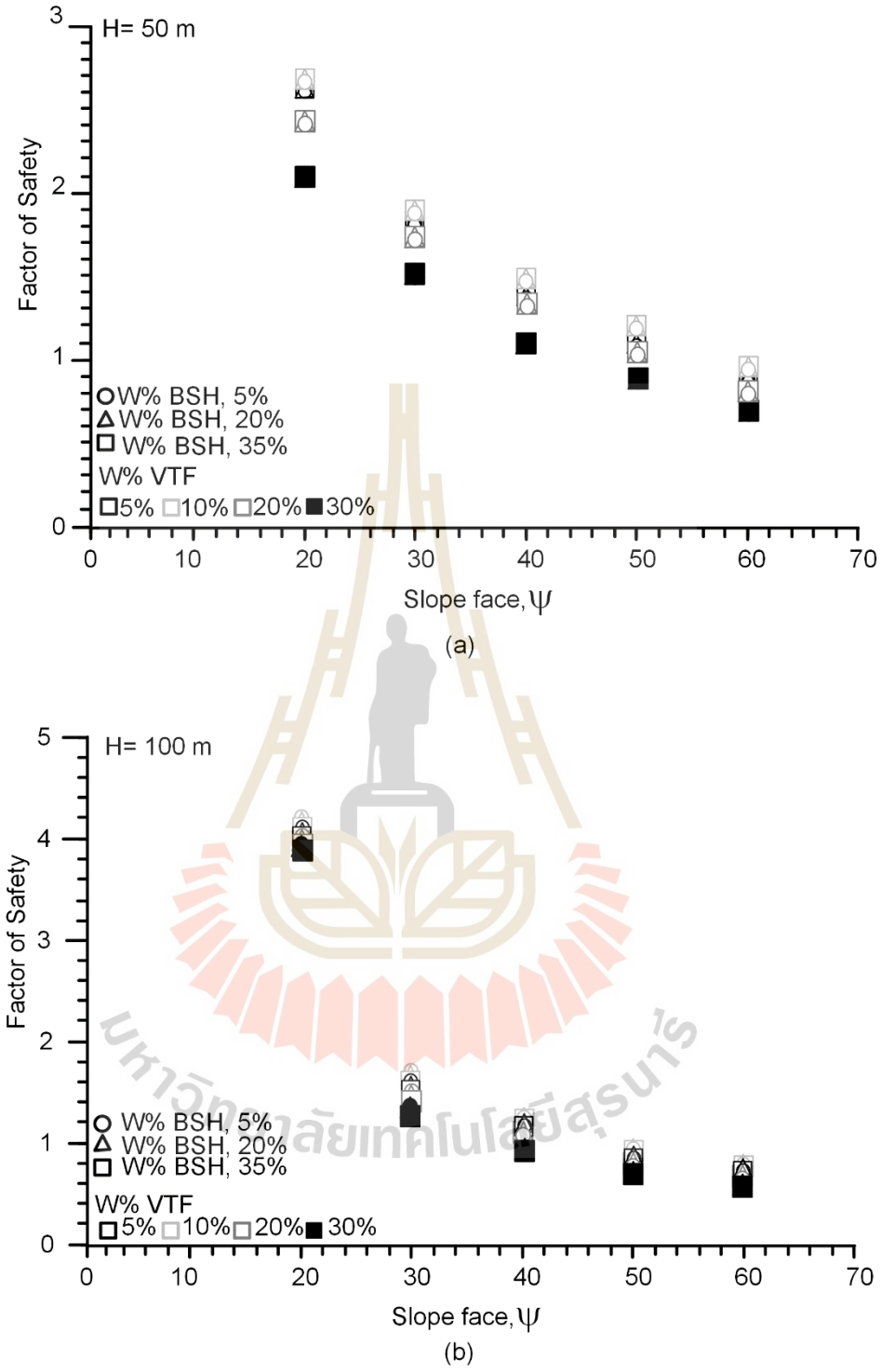


Figure 6.2 Factor of safety as a function of slope face angles under various water contents of BSH and VTF, and slope heights at 50 m (a) and 100 m (b).

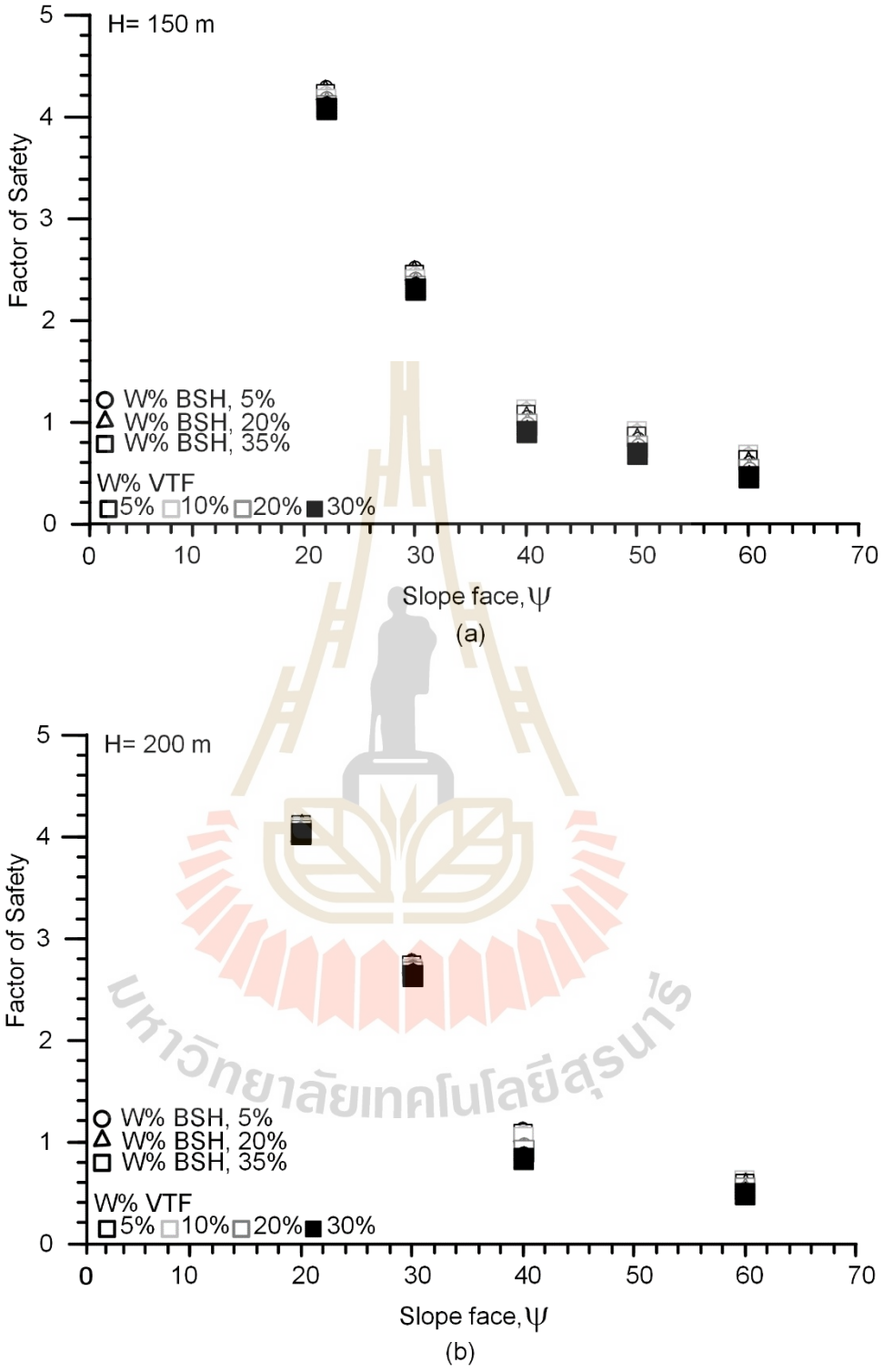


Figure 6.3 Factor of safety as a function of slope face angles under various water contents of BSH and VTF, and slope heights at 150 m (a) and 200 m (b).

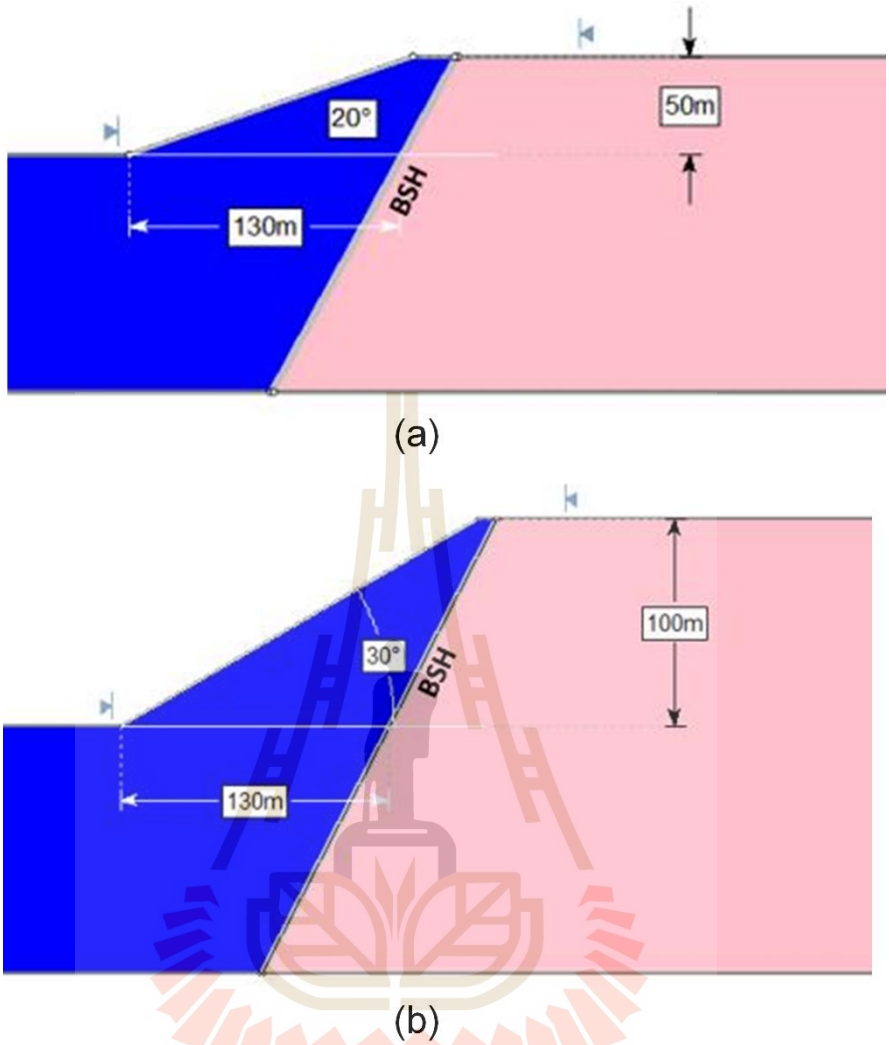


Figure 6.4 BSH plane do not appear as low slope height condition at (a) slope height 50 m, slope face 20° and (b) slope heights 100 m, slope face 30°

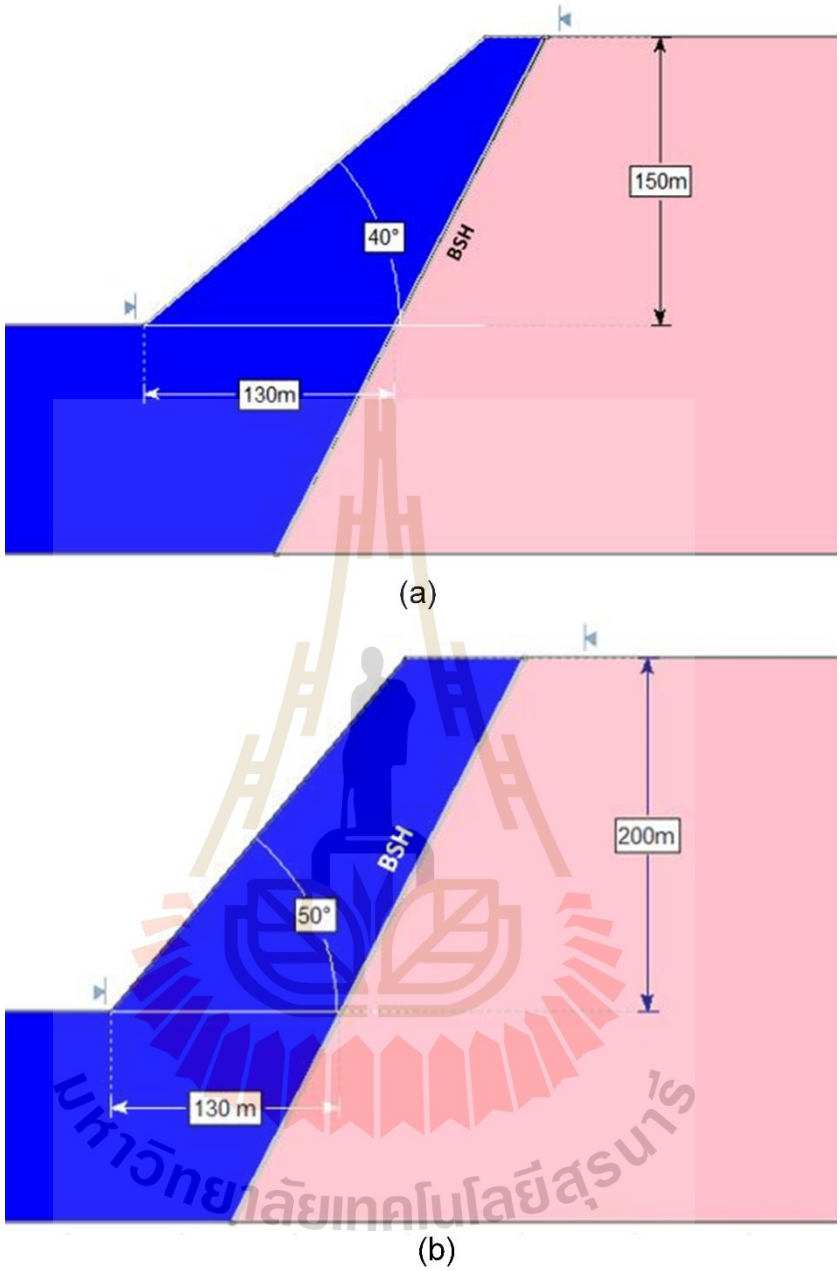


Figure 6.5 BSH plane do not appear as steep slope face condition at (a) slope face 40° slope height 150 m and (b) slope face 50° slope heights 200 m.

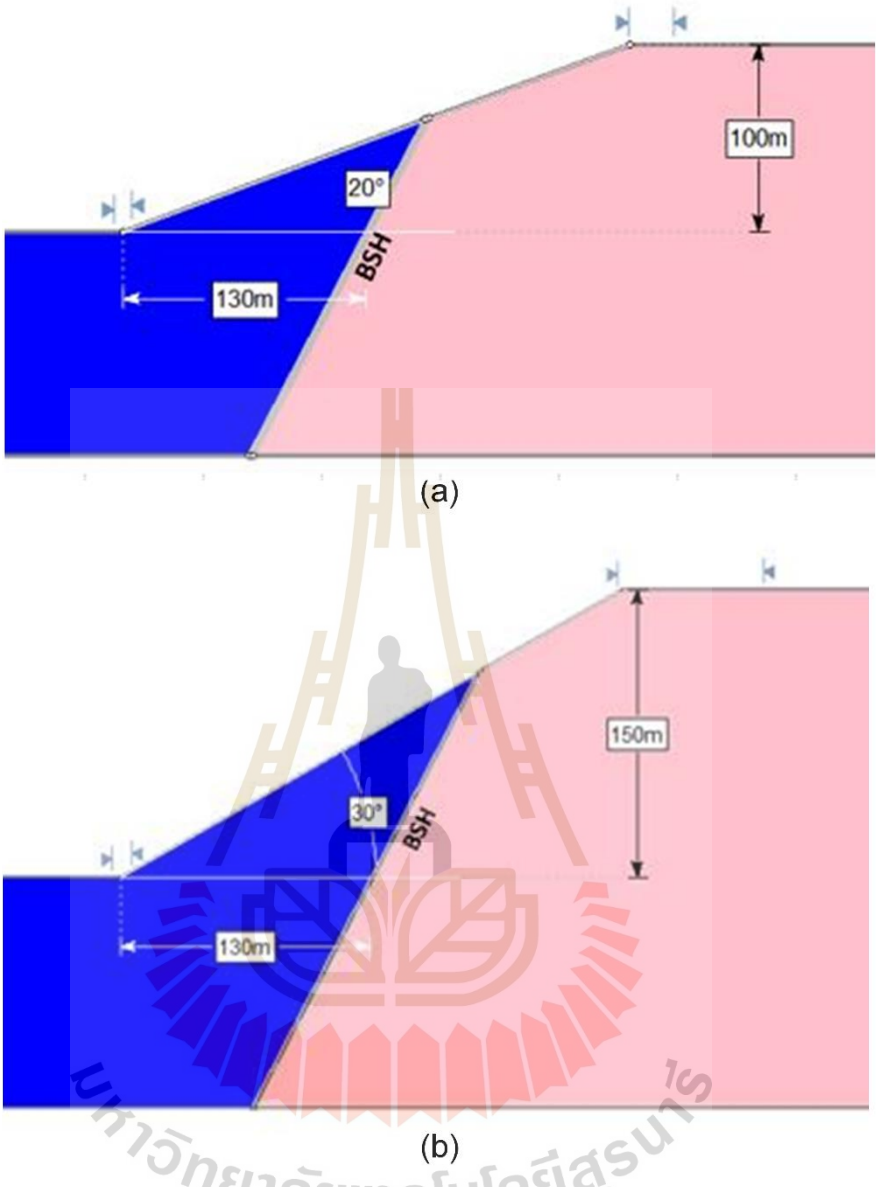


Figure 6.6 BSH plane appears at (a) slope face 20°, slope height 100 m and (b) slope face 30°, slope height 150 m.

Table 6.3 Summary of BSH position plane from simulated model.

Slope face (degrees)	Slope height (m)	Position of BSH plane
20	50	Unexposed-Low slope height
20	100	Exposed on slope
20	150	Exposed on slope
20	200	Exposed on slope
30	50	Unexposed-Low slope height
30	100	Unexposed-Low slope height
30	150	Exposed on slope
30	200	Exposed on slope
40	50	Unexposed-Steep slope face
40	100	Unexposed-Steep slope face
40	150	Unexposed-Steep slope face
40	200	Exposed on slope
50	50	Unexposed-Steep slope face
50	100	Unexposed-Steep slope face
50	150	Unexposed-Steep slope face
50	200	Unexposed-Steep slope face
60	50	Unexposed-Steep slope face
60	100	Unexposed-Steep slope face
60	150	Unexposed-Steep slope face
60	200	Unexposed-Steep slope face

มหาวิทยาลัยเทคโนโลยีสุรนารี

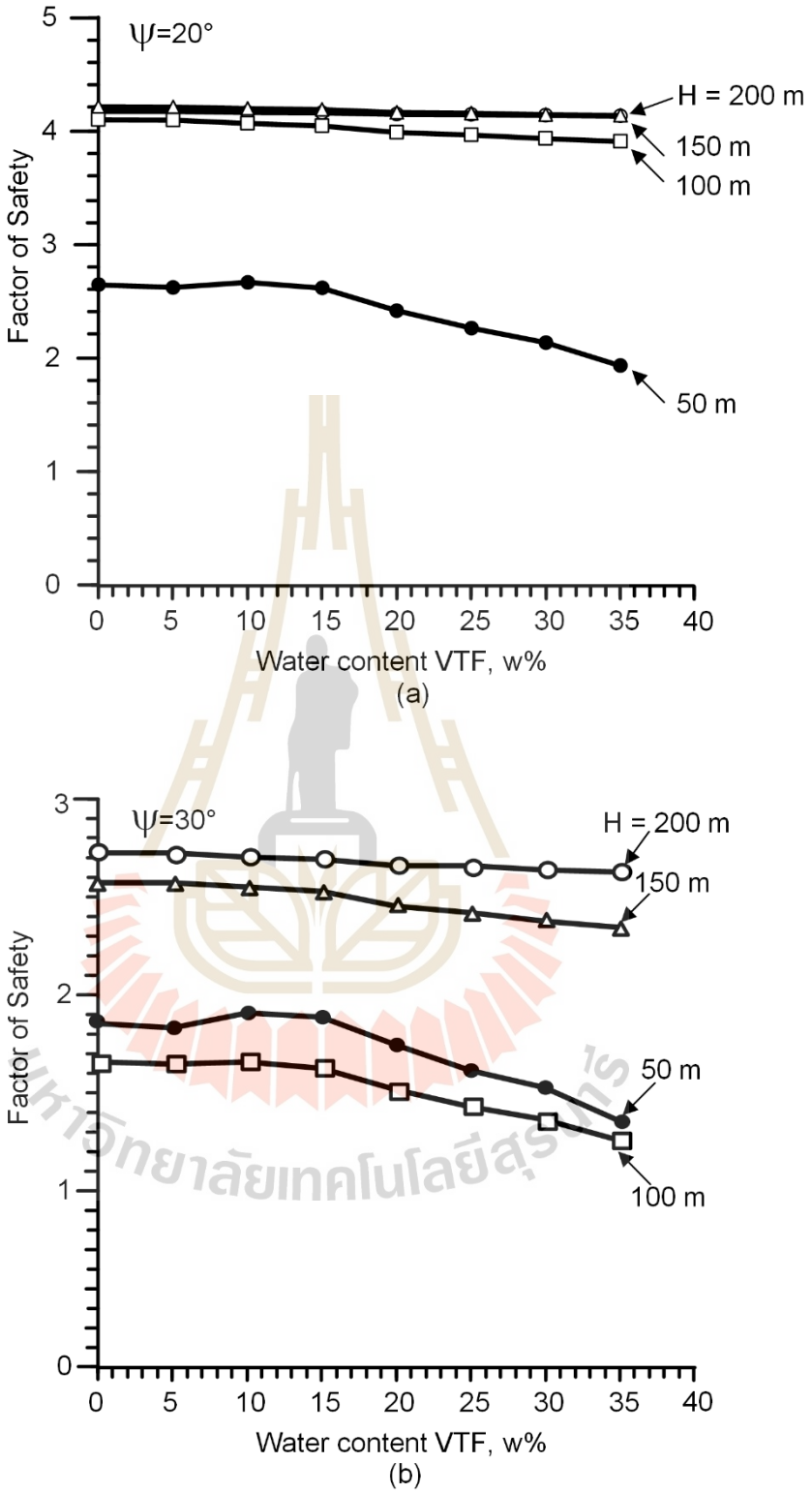


Figure 6.7 Factor of safety as a function of water contents of VTF under various slope heights with slope face angles at 20° (a) and 30° (b).

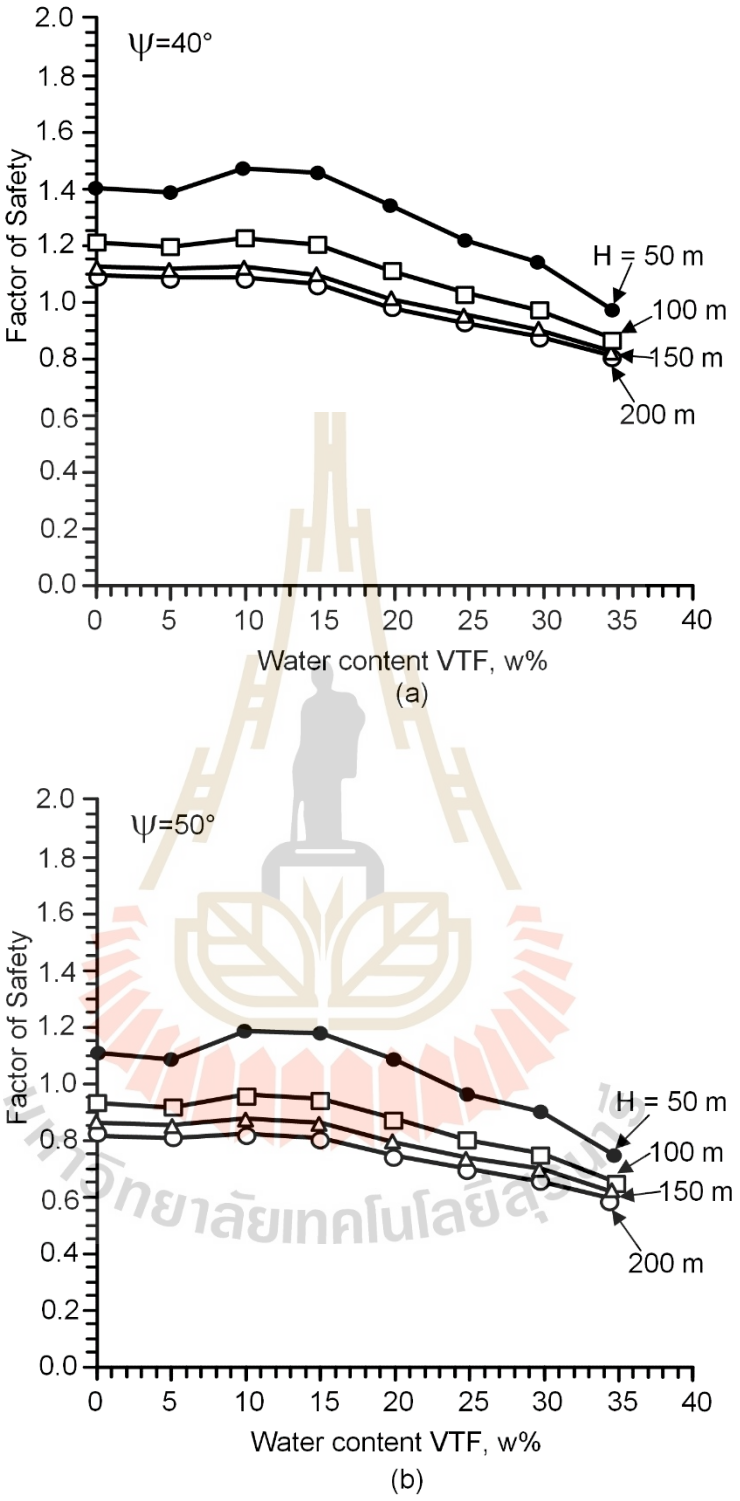


Figure 6.8 Factor of safety as a function of water contents of VTF under various slope heights with slope face angles at 40°(a) and 50°(b).

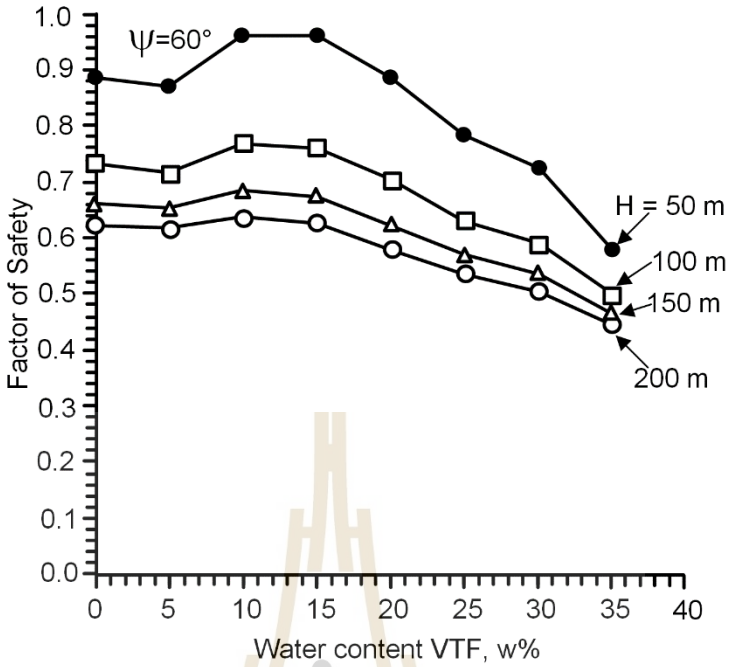


Figure 6.9 Factor of safety as a function of water contents of VTF under various slope heights with slope face angles at 60°.

6.5 Empirical equation

The empirical equation is derived from the simulation results of unexposed conditions of weak BSH plane using the SPSS program (Wendai, 2000). This is because the FS of exposed conditions of weak BSH planes are greater than 2.0 which are accepted in the field. Figure 6.10 plots the factor of safety as a function of water contents which are multiplied by power function of friction angles and slope heights. The mathematical relationship between FS, w, ψ and H parameters can be represented by:

$$FS = (-1343w^2+181.43w +353.45)\bullet(\psi^{-1.24}\bullet H^{-0.24}) \quad (6.1)$$

where FS is factor of safety, w is water content, ψ is slope face angle and h is slope height. The constants of mention equations are generated by simulation model results in non-linear regression analysis. The coefficient of determination (R^2) at 0.981 are indicated good correlation simulation data by correlation coefficient.

The empirical equation's limits are appropriate for open pit slopes where clay minerals dominate the majority of the lithology of the overall slope face.

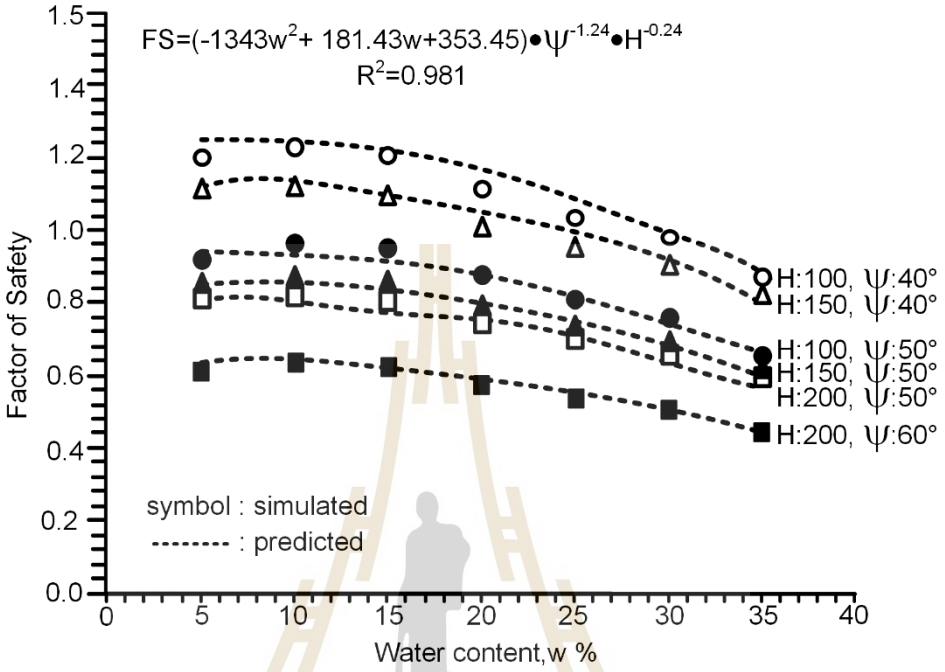


Figure 6.10 Predicted factor of safety as a function of water contents, slope face angles, and slope heights.

มหาวิทยาลัยเทคโนโลยีสุรนารี

CHAPTER VII
DISCUSSIONS, CONCLUSIONS AND RECOMMENDATIONS FOR FUTURE STUDIES

7.1 Discussions

The south wall open pit mine of Phu Kham mining, Laos is studied in terms of factor of safety as affected by water contents of mudflow on hanging wall using direct shear tests, numerical simulation, and empirical equation. The mudflow materials are black fault and tuff materials obtained from the collection of drilling core samples. A direct shear test is performed on mudflow under different water contents. The relation of simulated results from laboratory tests is derived to form empirical equation to determination of slope stability by basic properties parameters of materials on the sidewall.

The cohesion and friction angles from the direct shear test are determined with different water contents used in 0, 5, 10, 15, 20, 25, 30 and 35% by weights. Laboratory results are numerical simulation models based on the limit equilibrium method. It is predefined that slope geometry has a black fault of 2 meters of thickness and a distance between the fault and the toe of 130 meters. The four hundred twenty numerical models are simulated on the hanging wall. This study does not consider groundwater conditions.

The findings from this study indicate that the factor controlling slope stability is slope face angle, slope height and basic properties (cohesion and friction angle) of hanging wall materials with varied water content. These results agree reasonably well with those studies from researchers (Shiferaw, 2021; Yong et al., 2023; Gusman et al., 2018; Wang et al., 1990; Hao et al., 2023; Li et al., 2021) that slope stability is increased by decreasing of slope face angle, slope height and water content of materials.

The empirical equation is proposed to predict the factor of safety of slope based on slope face angle, slope height and water content parameters. The soft material of slope is applied to equation (6.1) of the open pit mine. The main material has cohesion from 1.48 up to 36.66 kPa, and friction angle from 26 up to 37 degrees. The slope height is 50 to 200 meters and the distance of fault from toe is 130 meters. The correlation of simulation data is indicated by a good correlation coefficient (R^2 > 0.9) which confides reasonably.

The comparison of the empirical equation on pit slope geometry with different numerical simulation methods using limit equilibrium (LEM) by Slide2D software, finite difference method (FDM) by FLAC 2D software and finite element method (FEM) by RS2 software is shown in Figures 7.1 and 7.2.

7.2 Conclusions

The study was carried out with the aim, they can be summarized as follows:

1) Excavation of mine slope is fast, so accurate empirical equation is required.
2) Factor of safety of empirical equation is similar with numerical simulation results (LEM, FDM and FEM).
3) Effect of water content of main or/and seam fault materials slightly affects from factor of safety of numerical simulation results.
4) Slope stability is increased by decreasing slope face angle, slope height and water content because high shear strength leads to high friction force to driving of rock mass.
5) Exposed fault on slope face case indicates minor failure (not overall slope) by LEM simulation.
6) The empirical equation is derived by LEM result of overall slope failure case. The equation is appropriate for open pit slopes where clay minerals dominate the majority of the lithology.

มหาวิทยาลัยเทคโนโลยีสุรนารี

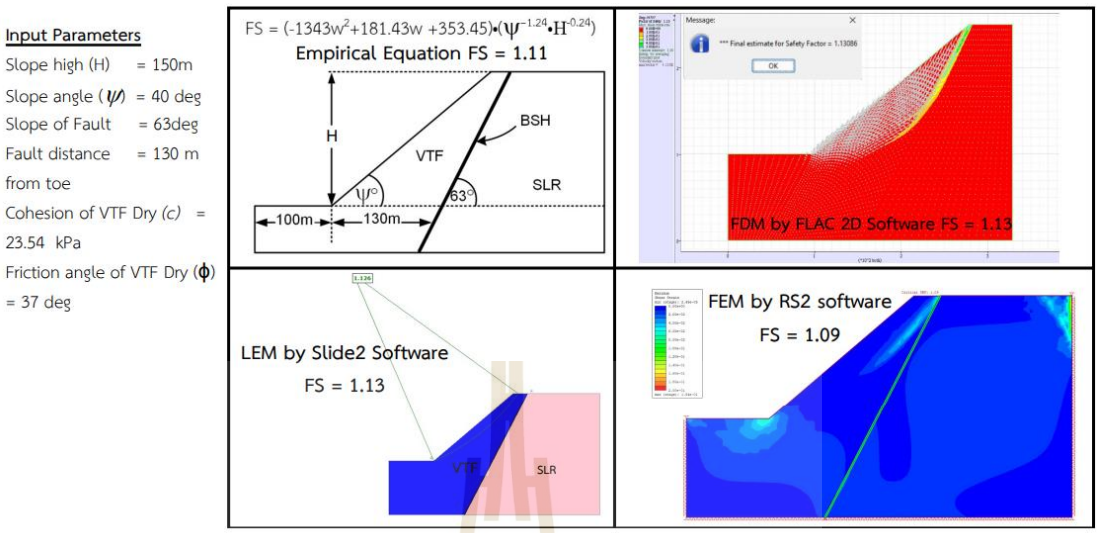


Figure 7.1 Comparison of empirical equation with different numerical simulation models at cohesion 23.54 kPa and friction angle 37 degrees of VTF material.

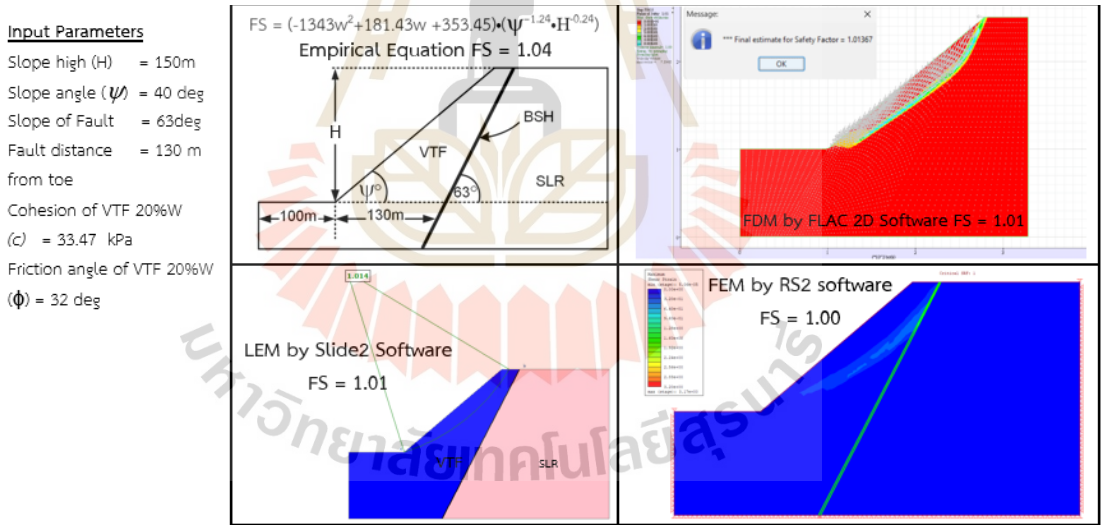


Figure 7.2 Comparison of empirical equation with different numerical simulation models at cohesion 33.47 kPa and friction angle 32 degrees of VTF material.

7.3 Recommendations for future studies

The uncertainties and adequacies of the research investigation and results discussed above lead to the recommendations for further studies, as follows.

1. Thickness, direction and position of seam weak plane should be studied as they may affect the overall slope.

2. The addition of quantity and different directions of seam weak plane should be studied in the field.

3. Dynamic loading on exposed weak plan of slope should be studied to assess the effect of heavy vehicles moving on the slope crest.

4. The direct shear test should be conducted using a wider range of normal load to more accurately simulate real-field conditions.

5. The field density measurements should be taken throughout the year, including the dry, pre-wet, wet, and post-wet seasons, to analyse the varying water contents in the field.

มหาวิทยาลัยเทคโนโลยีสุรนารี

REFERENCES

American Society for Testing and Materials. (2021). *Annual Book of ASTM Standards: Standard test method for density and unit weight of soil in place by sand-cone method* (Vol. 04.08). West Conshohocken, PA: ASTM International.

American Society for Testing and Materials. (2021). *Annual Book of ASTM Standards: Standard test method for laboratory determination of water (moisture) content of soil and rock by mass* (Vol. 04.08). West Conshohocken, PA: ASTM International.

American Society for Testing and Materials. (2021). *Annual Book of ASTM Standards: Standard practice for classification of soils for engineering purposes (Unified Soil Classification System)* (Vol. 04.08). West Conshohocken, PA: ASTM International.

American Society for Testing and Materials. (2021). *Annual Book of ASTM Standards: Standard practice for description and identification of soils (Visual-Manual Procedures)* (Vol. 04.08). West Conshohocken, PA: ASTM International.

American Society for Testing and Materials. (2021). *Annual Book of ASTM Standards: Standard test method for direct shear test of soil under consolidated drained condition* (Vol. 04.08). West Conshohocken, PA: ASTM International.

American Society for Testing and Materials. (2021). *Annual Book of ASTM Standards: Standard test method for particle-size analysis of soil* (Vol. 04.08). West Conshohocken, PA: ASTM International.

มหาวิทยาลัยเทคโนโลยีสุรนารี

American Society for Testing and Materials. (2021). *Annual Book of ASTM Standards: Standard test method for liquid limit, plastic limit, and plasticity index of soil.* (Vol. 04.08). West Conshohocken, PA: ASTM International.

American Society for Testing and Materials. (2021). *Annual Book of ASTM Standards: Standard test methods for specific gravity of soil solids by water pycnometer* (Vol. 04.08). West Conshohocken, PA: ASTM International.

Beyabanaki, S. A. (2020). A comparison between using finite difference and limit equilibrium methods for landslide analysis of slopes containing a weak layer. *American Journal of Engineering Research*, 9(12): 68-79.

Bishop, C. M. (1995). Neural networks for pattern recognition. *Oxford university press*.

Charkley, F. N., Zhang, K., & Mei, G. (2019). Shear strength of compacted clays as affected by mineral content and wet-Dry Cycles. *Advances in Civil Engineering*, 2019: 1-8.

El Hariri, A., Ahmed, A. E. E., & Kiss, P. (2023). Review on soil shear strength with loam sand soil results using direct shear test. *Journal of Terramechanics*, 107: 47-59.

Fahy, M.P., & Guccione, M.J. (1979). Estimating strength of sandstone using petrographic thin section data. *Engineering Geology*, 16(4): 467 485.

Fan P (2000) Accreted terranes and mineral deposits of Indochina. *Journal of Asian Earth Sciences*, 18: 343–350.

Fredlund., D.G., Morgenstern, N.R., & Widger, R.A. (1978). The shear strength of unsaturated soils. *Canadian Geotech Journal*, 16: 121-139.

Fuenkajorn, K., & Sri-In, T. (2009). Prediction of long-term strength of some weak rocks. *Engineering Journal of Research and Development*, 20(4): 1-12.

Gunsallus, K.T., & Kulhawy, F.H. (1984). A comparative evaluation of rock strength measures. International *Journal of Rock Mechanics and Mining Sciences and Geomechanics Abstracts*, 21(5): 233-248.

Gusman, M., Nazki, A., & Putra, R. R. (2018). The modelling influence of water content to mechanical parameter of soil in analysis of slope stability. *Journal of Physics: Conference Series*, 1008(1): 012022.

Hao, J., Jia, P., Wu, T., Li, W., Chen, J., Yang, X., & Zhang, M. (2023). Numerical analysis of the impacts of rainfall on permafrost-related slope stability on the Qinghai–Tibet Plateau. *Journal of Hydrology*, 47: 101439.

Huang, Y. H. (2012). Stability analysis of earth slopes. S*pringer Science and Business Media*, 1, 213-231. doi: 10.1007/978-1-46846602-7

Ioanna, I., Dimitrios, R., Theodora, P., & Paris, T. (2009). Geotechnical and mineralogical properties of weak rocks from Central Greece. *Open Geosciences*, 1(4): 431-442.

Janbu, N. (1955). Application of composite slip surfaces for stability analysis. *European Conferrence on Stability of Earth Slopes*, 3: 43-49.

King, S. (2015). Structural geology, face mapping and fault modelling of the Phu Kham Mine, Laos. *Soild Geology Ltd Report to Phu Bia Mining*, August 2015, pp 257-273.

Li, Y. H., Lv, M. F., Guo, Y. C., & Huang, M. S. (2021). Effects of the soil water content and relative roughness on the shear strength of silt and steel plate interface. *Measurement*, 174: 109003.

Liu, G., Li, S., & Wang, J. (2021). New Green-Ampt model based on fractional derivative and its application in 3D slope stability analysis. *Journal of Hydrology*, 603: 127084.

Liu, W., Ouyang, G., Luo, X., Luo, J., Hu, L., & Fu, M. (2020). Moisture content, pore-water pressure and wetting front in granite residual soil during collapsing erosion with varying slope angle. *Geomorphology*, 362.

Mao, J., Bierlein, F. P., & Tate, N. M. (2005). Discovery, geology and mineralisation of the Phu Kham copper-gold deposit Lao People's Democratic Republic. In Mineral Deposit Research: Meeting the Global Challenge: *Proceedings of the the Eighth Biennial SGA Meeting Beijing*, Springer Berlin Heidelberg, pp. 1077-1080.

Morgenstern, N. U., & Price, V. E. (1965). The analysis of the stability of general slip surfaces. *Geotechnique*, 15(1): 79-93.

Nonveiller, E. (1965). The stability analysis of slopes with a slip surface of general shape. *Proceedings of the 6th International Conference on Soil Mechanics and Foundation Engineering*, pp. 522-525.

Pei, P., Zhao, Y., Ni, P., & Mei, G. (2020). A protective measure for expansive soil slopes based on moisture content control. *Engineering Geology*, 269: 105527.

Pramuji. (2015). Phu Kham south wall sub-horizontal drains design. *Report of Phu Bia Mining*, May 2015, pp. 1-4.

Ramli, D & Lucas, D. (2021). Phu Kham (PKM) South wall cut back (SWCB): Geotechnical design report. *Mining One Ltd Report to Phu Bia Mining*, June 2021, pp. 33-105.

Sarma, S. K. (1979). Stability analysis of embankments and slopes. *Journal of the Geotechnical Engineering Division*, 105(12): 1511-1524.

Shakoor, A., & Bonelli, R.E. (1991). Relationship between petrographic characteristics, engineering index properties and mechanical properties of selected sandstones. *Bulletin of the Association of Engineering Geologists*, 28(1): 55-71.

Shiferaw, H. M. (2021). Study on the influence of slope height and angle on the factor of safety and shape of failure of slopes based on strength reduction method of analysis. *Beni-Suef University Journal of Basic and Applied Sciences*, 10(1): 1-11.

Soysouvanh, V., Ariffin, K. S., & Wantanabe, K. (2016). Ore mineralogy and geochemistry of the Phu Kham Porphyry copper-gold deposit, *Hosted within NE Fault Zone, Lao PDR. Procedia Chemistry*, 19: 961-968.

Su, P., Qiu, P., Liu, B., Chen, W., & Su, S. (2022). Stability prediction and optimal angle of high slope in open-pit mine based on two-dimension limit equilibrium method and three-dimension numerical simulation. *Physics and Chemistry of the Earth, Part A/B/C*, 127: 103151.

Wang, J., Zhou, Z., Chen, C., Wang, H., & Chen, Z. (2023). Failure mechanism and stability analysis of an open-pit slope under excavation unloading conditions. *Frontiers in Earth Science*, 11: 1109316.

Wang, Y. Y., & Lin, Z. G. (1990). Structural features and physical and mechanical properties of Chinese loess. *Science Press*, Beijing.

Yong, X., Zhang, Y., Hou, Y., Han, B., An, N., Zhang, H., & Ma, Y. (2023). Stability of loess high-fill slope based on monitored soil moisture changes. *Research in Cold and Arid Regions*.

Zhang, B., Zhao, Q. G., Horn, R., & Baumgartl, T. (2001). Shear strength of surface soil as affected by soil bulk density and soil water content. *Soil and tillage research*, 59(3-4): 97-106.

Zhang, Y., Zhong, X., Lin, J., Zhao, D., Jiang, F., Wang, M. K., & Huang, Y. (2020). Effects of fractal dimension and water content on the shear strength of red soil in the hilly granitic region of southern China. *Geomorphology*, 351: 106956.

Zhao, X., Zhao, Y., & Yu, W. (2023). The safety factor of a heterogeneous slope in an open-pit metal mine: A case study from the Tanjianshan gold mine. *Frontiers in Earth Science*, 10: 990454.

มหาวิทยาลัยเทคโนโลยีสุรนารี

BIOGRAPHY

Suriya Wongkaew was born in 1978 in Tak Province, Thailand. He received his Bachelor's Degree in Geological Engineering from Suranaree University of Technology in 2001. For his post-graduate, he works at Phu Bia Mining Limited in Lao, PDR since 2010 and commenced to study with a Master's degree in Civil, Transportation and Geo-resources Engineering Program, Institute of Engineering, Suranaree University of Technology during graduation, 2019-2023.

มหาวิทยาลัยเทคโนโลยีสุรนารี